

ABSTRACT

TITLE OF DISSERTATION: DEVELOPMENT OF A FOUR CAVITY
SECOND-HARMONIC GYROKLYSTRON
AS DRIVER FOR A LINEAR ACCELERATOR
Emmanuel Steve Gouveia, Doctor of Philosophy, 2004

Dissertation directed by: Professor Thomas M. Antonsen
Departments of Physics and Electrical Engineering

Gyroklystrons are microwave amplifiers that combine the multi-cavity configuration of a klystron with the energy extraction mechanism of the cyclotron maser instability. These devices have been studied at the University of Maryland for several years. This work is focused on the development of a 17.14 GHz four-cavity frequency-doubling gyroklystron circuit. This device was designed specifically to drive a high gradient linear accelerator recently developed by the Haimson Corporation. The gyroklystron was designed using the code MAGYKL, yielding a predicted output power of 87 MW for an input drive power of 250 W, with a velocity pitch ratio (α) of 1.4. The tube was later fabricated, and underwent a series of experimental tests to evaluate its performance. The highest peak power observed was 18.5 ± 1.7 MW, corresponding to an efficiency of 7.0 % and a gain of 24.0 dB.

This result fell short of the theoretical design, yet it was consistent with the low value of the velocity pitch ratio ($\alpha = 0.85$) realized in the experiments. This limitation on α was linked to the onset of instabilities in the input cavity. The ultimate cause of these instabilities was the thermal non-uniformity in the emitter of our electron gun, which led to a significant variation (approximately 50 %) of the current density across the beam. In order to remedy this problem, we have radically redesigned the input cavity, changing both its geometry and Q factor. These measures should dramatically reduce the probability of instabilities, thus allowing us to remove the experimental limitations imposed on α . This new design is presented here. We also describe advanced designs of an output cavity with radial power extraction, and a compact circular to rectangular mode converter. A detailed description of the present experimental setup is given, along with an overview of the power transport system necessary to feed the accelerator with output power from the gyrokystron.

DEVELOPMENT OF A FOUR CAVITY
SECOND-HARMONIC GYROKLYSTRON AS DRIVER FOR
A LINEAR ACCELERATOR

by

Emmanuel Steve Gouveia

Dissertation submitted to the Faculty of the Graduate School
of the University of Maryland at College Park in partial
fulfillment of the requirements for the degree of
Doctor of Philosophy
2004

Advisory Committee:

Professor Thomas Antonsen, Chair

Professor Richard Ellis

Professor Victor Granatstein

Professor Hans Griem

Professor Wesley Lawson

© Copyright by
Emmanuel Steve Gouveia
2004

TABLE OF CONTENTS

List of Tables.....	iv
List of Figures.....	v
Chapter 1: Introduction.....	1
1.1 Context of Research.....	2
1.2 Overview of the University of Maryland GKL Program	9
Chapter 2: Gyroklystron Theory and Design	14
2.1 Basic Theory.....	14
2.2 Design Methodology	18
Chapter 3: Experimental Setup.....	33
3.1 System Overview.....	33
3.2 The Modulator	35
3.3 The Electron Gun.....	37
3.4 The Magnet System	40
3.5 Beam and Microwave Transport System.....	41
3.6 Input Power System.....	43
3.7 Microwave Diagnostics	44
Chapter 4: Design and Implementation of the Four-Cavity Gyroklystron.....	49
4.1 Overview of Four-Cavity Circuit Design	49
4.2 The Input Cavity	51
4.3 Buncher and Penultimate Cavities.....	53
4.4 Output cavity	55
4.5 Drift Spaces	56
4.6 Small Uptaper and Coaxial to Circular Transition	57
4.7 Performance of Theoretical Design of Four-Cavity Gyroklystron.....	58
Chapter 5: Experimental Results	62
5.1 Overview of Experimental Procedure	62
5.2 Presentation of Experimental Results.....	65
5.3 Preliminary Analysis	72
5.4 Experimental Observation of Instability.....	75
5.5 Analysis of MIG Emitter Performance.....	77
Chapter 6: Design and Cold-Testing of New Input Cavity	84
6.1 Analysis of Instability in the Input Cavity.....	84
6.2 Design of New Input Cavity	89
6.3 Cold-Testing of New Input Cavity	91
6.4 Theoretical Performance of Circuit with new Input Cavity	93

Chapter 7: Design of New Radial-Extraction Output Cavity	97
7.1 Introduction	97
7.2 Design Procedure.....	101
7.3 Final Results	105
Chapter 8: Output Power Transport System and Linear Accelerator	108
8.1 Introduction	108
8.2 Design of Circular to Rectangular Converter	109
8.3 Overview of Power Transport System.....	113
8.4 The HRC Linear Accelerator.....	117
Chapter 9: Summary and Future Work.....	119
References	121

LIST OF TABLES

Number	Page
1. The Standard Model of Particle Physics.	3
2. Summary of UMD cylindrical gyrokystrons.	11
3. Summary of UMD coaxial gyrokystrons since 1994.	13
4. Gun parameters for gyrokystron systems at UMD.	31
5. Specifications of the electron gun.	39
6. Theoretical design of the four-cavity circuit.	50
7. Modes that are not cutoff in the drift.	56
8. Dielectric properties of microwave-absorbing ceramics.	57
9. Results from HFSS eigenmode solver.	84
10. Electromagnetic properties of new output cavity.	105
11. Geometric parameters of new output cavity.	105
12. Final dimensions of converter.	111

LIST OF FIGURES

Number	Page
1. Diagram of the model for a given gyrokystron cavity.	19
2. Representation of the gyrokystron subsystems	33
3. Experimental test-bed	34
4. Modulator circuitry	36
5. Typical beam emission from MIG (EGUN)	38
6. Cross section of small orbit gyrotron electron beam	40
7. Diagram of input power system	43
8. Cross-sectional view of anechoic chamber.	45
9. Diagram of signal transmission line from anechoic chamber.	46
10. Plot of crystal power as function of crystal voltage.	47
11. Engineering diagram of four-cavity Circuit	49
12. Cross-sectional view of input cavity	51
13. Cold-test transmission and reflection coefficients	52
14. Start of oscillation curves for input cavity.	53
15. Cross-sectional view of buncher cavity.	54
16. Start of oscillation curves for buncher cavity.	54
17. Cross-sectional view of output cavity.	55
18. New dual tapers: A – Inner Transition, B – Outer Taper.	58
19. Output power as function of input power.	59
20. Efficiency as a function of drive frequency.	59

Number	Page
21. Effect of alpha on efficiency as function of input power.	60
22. Effect of alpha on efficiency and gain.	61
23. Reactivation of electron gun.	62
24. Typical pulses of beam voltage and current.	64
25. Experimental magnetic field profile.	66
26. Output pulse with highest peak power observed	67
27. Forward and reflected input power.	67
28. Widest output pulse observed.	68
29. Phase correlation signal.	69
30. Spectrum of output power.	70
31. Far-field pattern of output and theoretical curve for TE ₀₂ .	71
32. Experimental drive curve for four-cavity gyrokystron.	72
33. Theoretical performance of circuit for $\alpha = 0.85$.	73
34. Comparison of theoretical and experimental magnetic fields.	74
35. Instability in input cavity.	76
36. Spectrum of instability in input cavity.	76
37. Variation of surface temperature of emitter.	78
38. Thermal profile of emitter.	79
39. Comparison of thermal and x-ray data from emitter studies.	80
40. Current density as function of azimuthal location.	81
41. α as function of azimuthal location.	82
42. Variation of the axial velocity spread across beam.	83

Number	Page
43. Electric field pattern of mode 2 from HFSS solutions.	85
44. Electric field pattern of mode 4 from HFSS solutions.	86
45. Broadband S_{21} curve for input cavity.	87
46. Start-of-oscillation Q for TE_{411} mode.	88
47. Start-of-oscillation Q for TE_{011} mode.	89
48. Cross-sectional view of old and new designs for the input cavity.	90
49. S_{21} curve for final input cavity.	92
50. Broadband S_{21} curve for final input cavity.	93
51. Performance of gyroklystron with new input cavity.	95
52. Performance of gyroklystron with defective emitter.	96
53. Current axial-extraction output cavity.	98
54. Radial-extraction output cavity.	100
55. Three dimensional model of new output cavity.	101
56. Simplified cross-sectional view of model.	102
57. Cross-sectional electric field distribution.	103
58. Longitudinal electric field distribution.	104
59. Resonant frequency and Q as a function of slot length.	106
60. Transmission coefficient for TE_{01} mode.	107
61. Reflection coefficient of the new cavity's injection port.	107
62. Cross-sectional view of converter.	109
63. 3-D Model of converter.	111
64. Reflection coefficient of converter.	112

Number	Page
65. Transmission coefficient of converter.	112
66. Complete view of power transport system coupled to accelerator.	113
67. Rippled-wall converter.	115
68. Schematic of part of the output waveguide system.	116
69. Circular pumping cross.	116
70. Schematic of linear accelerator.	117
71. Build-up of power in accelerating structure.	118

Chapter 1 – Introduction

This dissertation details the latest developments in the Gyroklystron Program at the University of Maryland, under the auspices of the Institute for Research in Electronics and Applied Physics (IREAP). In particular, I will describe the design and construction of a four-cavity second harmonic gyroklystron tube, along with experimental studies of its performance. This device has been conceived as a state-of-the-art prototype driver for future linear accelerators. I will also detail work on advanced designs for an input cavity, a radial-extraction output cavity, and a novel circular to rectangular mode converter.

In this chapter I will give an overview of the work which led to this research and I will summarize previous experiments conducted by the University of Maryland Gyroklystron group. The following chapter will present a brief theoretical description of the gyroklystron and computer codes used in its design. Chapter 3 will deal with the experimental test bed and diagnostic devices for studying the performance of the amplifier. In Chapter 4, a detailed description of the circuit design and implementation will be presented. Chapter 5 will describe experimental results of the tube's operation, including the existence of an instability which limited the performance of the amplifier. In Chapter 6 I will present the design and cold-testing of a new input cavity which should overcome the instability observed. Then in Chapter 7 I will show my design of a new type of output cavity which allows radial power extraction. The subject of Chapter 8 is the power transport system necessary to connect our gyroklystron to a linear accelerator. This linear accelerator was fabricated by the Haimson Research

Corporation (HRC), and will be briefly described in Chapter 8 as well. Finally, in Chapter 9, I will summarize the work discussed in this entire text and will refer to the future challenges that lie in the application of the gyrokystron to drive the HRC accelerating structure.

1.1 Context of Research

Since our very beginnings, human beings have been driven by an incessant curiosity. This relentless desire to understand the phenomena occurring around us, coupled with the ever present instinct for survival in a dangerous world, has driven us in a unique and eternal quest for knowledge and subsequent mastery over Nature. As our knowledge has progressed, we have plunged into realms of ever-increasing abstraction, deciphering the laws of nature, re-engineering its creations and finding beauty unlike anything we could have expected.

Now, in the beginning of the third millennium of the common era, roughly fifty-five hundred years after the invention of writing in ancient Sumeria, we have reached an amazing level of understanding. We have developed theories which allow us to comprehend most phenomena occurring around us -- from the subatomic scale described by quantum field theories, to the immensity of galactic dynamics explained by general relativity. The conceptually greatest epistemological task facing us now is the search for a convergence of these great realms of physics, that is, the development and experimental confirmation of a theory that reconciles gravitation with quantum mechanics. Such a feat will answer many fundamental questions about the inner workings, origin and possible future of the Universe.

	Elementary Particles			Elementary Fields	
Particle Type	Three Generations of Matter			Fundamental Force	Carrier
Quarks	<i>Up</i>	<i>Charm</i>	<i>Top</i>	<i>Electromagnetism</i>	<i>Photon</i>
	<i>Down</i>	<i>Strange</i>	<i>Bottom</i>	<i>Weak Nuclear</i>	<i>Weak bosons: Z⁰ W⁺ W⁻</i>
Leptons	<i>Electron Neutrino</i>	<i>Muon Neutrino</i>	<i>Tau Neutrino</i>	<i>Strong Nuclear</i>	<i>Gluons</i>
	<i>Electron</i>	<i>Muon</i>	<i>Tau</i>	<i>Gravity</i>	<i>Graviton</i>

Table 1 – The Standard Model of Particle Physics

Our current view of the elementary structure of energy and matter is described in the Standard Model of Particle Physics [1], which is exhibited in Table 1. According to it, all matter is constituted by quarks and leptons in free (leptons only) or various bound combinations. There are six quarks and six leptons, each group being split into three generations of duplets. All interactions amongst these elementary particles are regulated by the four fundamental forces: electromagnetism, weak nuclear, strong nuclear and gravity. Each of these forces possesses specific carriers: photons for electromagnetic, weak bosons for weak nuclear, gluons for strong nuclear and gravitons for gravity. A unified theory would presumably be able to demonstrate that all these quanta are degenerate forms of one more fundamental particle, and the dynamics of this particle would then account for all phenomena in the universe, embracing both present quantum field theories and general relativity as subsets.

There are many theoretical models that offer possible extensions of the Standard Model, and therefore possible solutions for the unification of all fundamental forces. At present the most popular models beyond the Standard Model are contained within three classes of theories: supergravity (SUGRA), supersymmetry (SUSY) and string theories [2]. Two models in particular, the Minimum Supersymmetric Standard Model (MSSM) and Minimum Supergravity (mSUGRA) are especially interesting, since they predict phenomena in an energy range which should be observable by collider experiments [2,3]. Thus, there is an urgent need for experimental verification of predictions of these candidate theories, as well as the search for other phenomena not yet predicted.

The indispensable tool for probing the depths of the subatomic world is the particle accelerator. These are large machines that use electric and magnetic fields to accelerate, manipulate, and then collide beams made up of electrically-charged subatomic particles (such as electrons, protons or nuclei). Since the energy of these collisions is very high, it allows certain unusual localized phenomena to occur – phenomena which otherwise can only take place in the very center of stars, or further back in the very first instants after the Big Bang. It is in these energy scales that we can observe evidence of elementary interactions mediated by the fundamental forces [1]. The higher the energy, the further we can probe the subatomic realm in search of evidence for new phenomena.

Particle accelerators can be qualitatively characterized by three parameters: target type, geometry and particle species. The commonly used particle species in high energy accelerators are electrons, protons and their anti-matter counterparts (antiproton for the proton, positron for the electron), since these are the most stable electrically-

charged subatomic particles we know. The proton (or anti-proton) is made up of three quarks bound by gluons, and requires a center-of-mass energy in the range of 20 to 40 TeV to produce 1 TeV per constituent energy. The electron (and positron) on the other hand is an elementary particle, requiring a center-of-mass energy of less than 2 TeV in order to provide 1 TeV of energy for a fundamental interaction to occur. Additionally, the fact that electrons are elementary particles allows their collisions to have a much “cleaner” profile, lacking the multiple number of primary reactions and extra scores of secondary and higher-order interactions which plague the data analysis of proton accelerator experiments. Hence, event reconstruction from collected data in lepton accelerators is much more straightforward and accurate, usually allowing greater precision of measurements and the study of more complex particle signatures.

The accelerated particle beam can be impacted against a specially prepared fixed target (usually containing high-Z nuclei), or the beam can be impacted against another accelerated particle beam. This latter type of accelerator is called a collider, and it has the advantage of achieving higher center-of-mass energy levels (since kinetic energy from both accelerated beams boosts the final collision).

With respect to the geometry, a particle accelerator can either be linear or circular. In linear accelerators, the particle beam is guided in a straight trajectory passing through a series of accelerating structures which increase its kinetic energy before reaching the target. Circular accelerators re-circulate particle beams repeatedly through the same accelerating structures, thus allowing beams to reach higher final acceleration than linear accelerators. However, linear colliders have several intrinsic advantages over circular colliders even when operating at lower energy scales. Some of

these advantages are higher luminosity, reduced background interactions, better contained events and therefore more precise measurements [4]. Furthermore, a major disadvantage of circular accelerators is that in order to confine the beams to circular orbits, the particles in the beam suffer periodic transverse accelerations which yield synchrotron radiation. The instantaneous power loss from synchrotron radiation is given by [5]

$$P = \frac{2}{3} q^2 c \frac{\beta^4 \gamma^4}{\rho^2} = \frac{2}{3} q^2 c \frac{\beta^4}{\rho^2} \frac{E^4}{(m_0 c^2)^4}, \quad (1.1)$$

where q is the charge of the particle, E and m_0 are the total energy and rest mass of the particle, and ρ is the bending radius. Clearly, less massive particles will suffer greater energy loss due to synchrotron radiation than more massive particles with the same energy. The problem of synchrotron radiation is then particularly grave for leptonic beams (electrons and positrons), effectively limiting the performance of leptonic circular colliders to about one hundred GeV.

In order to produce energy levels beyond the current predicted 14 TeV for the next largest accelerator project – the Large Hadron Collider (LHC) accelerator at CERN – future accelerator designers will be forced to push the envelope of technology by taking advantage of any edge allowed by the laws of physics. A good conceptual candidate for future machines is then the leptonic (electron-positron) linear collider. Support for this idea has risen from recent studies which indicated that a leptonic linear collider of energy below 1 TeV may allow for more precise measurements of theorized new particles than the LHC [4,6,7]. A multi-TeV linear collider would require an accelerating gradient in excess of 100 MeV/m so as to keep the length of beam tunnels

to a reasonable size [8]. The principal problem with such high accelerating gradients is electrical breakdown inside the accelerating structure.

It has been shown elsewhere in the literature [9], that the accelerating gradient (E_a) is related to the peak power per feed (P) and drive frequency (f) by

$$E_a \propto P^{1/2} f , \quad (1.2)$$

So in order to increase the accelerating gradient one should employ RF sources at both higher values of power and frequency.

Klystrons are the current state-of-the-art microwave drivers for particle accelerators. First developed in 1939 [10], these microwave amplifiers are linear beam devices composed of a series of cavities and the output power is extracted from the axial kinetic energy of the electron beam. An example of the best presently realizable performance of klystrons can be contemplated in the plan for the Next Linear Collider (NLC) at SLAC, which will employ klystrons operating at 11.424 GHz and peak power of 75 MW [11,12]. Klystrons operate in the fundamental mode (TM_{010}), thus their performance becomes severely limited at very high frequencies since the linear cavity dimensions must decrease roughly proportionally to the wavelength so as to keep the system cutoff to all other modes. Hence their peak power effectively scales no better than

$$E_a \propto \lambda^2 , \quad (1.3)$$

where λ is the wavelength of the microwaves produced [9].

There is concurrently a great research effort into the study and development of other potential drivers for future accelerators. Some of these are magnicons [13], multiple-beam klystrons [14,15], relativistic klystrons [16,17], high power traveling

wave tubes (TWT) [18,19], gyro-TWT's [20], cyclotron auto-resonance masers [21], free-electron lasers [22,23,24].

One possible candidate to replace klystrons in future accelerators at high frequencies is the gyroklystron. The gyroklystron is a microwave tube that combines the multi-cavity amplifier configuration of a klystron with the energy extraction mechanism of the cyclotron maser instability [25]. The operation is similar to a klystron except that (a) bunching occurs in azimuthal phase space rather than in axial position, and (b) larger overmoded TE cavities are utilized. A beam composed of electrons gyrating in a magnetic field about a guiding radius enters the input cavity and receives an azimuthal momentum impulse due to the electric fields of an input signal. Afterwards, while the beam drifts between cavities, it is bunched ballistically in azimuthal phase as a result of this transverse velocity modulation received in the input cavity. The bunched beam ultimately releases energy in the output cavity through the cyclotron maser instability (a more detailed description of the operation of a gyroklystron will be presented in the next chapter).

It has been shown elsewhere in the literature [9] that when considering drivers for a typical high energy accelerator structure consisting of a disc-loaded traveling wave circuit, a good parameter for comparing the performance of the different drivers is the energy density (U_p) which is defined by

$$U_p = \frac{P_p t_p}{\lambda^2} = P_p t_p \frac{n^2 f_D^2}{c^2}, \quad (1.4)$$

where P_p is the peak power, t_p is the pulse length, λ is the wavelength of the output signal, f_D is the drive frequency and n is the multiple harmonic factor of the device's

operation ($\lambda = \frac{c}{n \cdot f_D}$). The higher U_p is for a certain device, the smaller will be the number of drivers needed for a particle accelerator to reach a same given energy level. Gyroklystrons are able to produce greater energy densities at greater frequencies than klystrons. This is partially due to the fact that in gyro-klystrons the peak power capability scales as the wavelength of the microwaves produced near the cyclotron frequency. Furthermore, even greater energy density (U_p) levels can be obtained by operating at multiple harmonics of the fundamental drive frequency. In fact, theoretical and experimental studies have indicated the potential of gyro-klystrons to fill various applications up to 95 GHz [26,27,28]

1.2 Overview of The University of Maryland Gyroklystron Program

Cylindrical Tubes

The research into gyro-amplifiers at the University of Maryland started in 1984, with the original goal of developing a 30MW device based on a PFN modulator with 500 kV, 200A and 1 μ s long pulses [29]. The first tubes tested were cylindrical two TE₀₁₁ cavity devices operating near the fundamental cyclotron frequency around 9.85 GHz, and their study constituted proof of principle experiments demonstrating the viability of gyro-klystrons [30]. Initially, however, very little power was produced due to spurious oscillating modes which were very detrimental to the operation of the amplifiers. Thereafter, a systematic effort was undertaken to eliminate the different classes of instabilities. A particularly effective procedure involved the addition of lossy dielectric materials to regions of the circuit that had been identified as prone to instabilities. For this purpose special lossy ceramics were fabricated [31]. The addition

of the lossy ceramics to the microwave tubes allowed studies with subsequent tubes to employ higher values of beam power and velocity pitch ratio (α) leading to a more efficient amplification regime. As a consequence, a series of fundamental frequency two-cavity tubes resulted in the production of 24 MW of peak power with an efficiency of 30% [32,33]. A series of three-cavity fundamental tubes led to a maximum peak power of 27 MW, with a maximum efficiency of 32% [34]. One should note that magnetic field tapering was also critical to the success of the tubes.

Next, higher harmonic tubes were designed and studied. Theoretical studies indicated that these tubes would be able to operate with the same platform, and with comparable output powers. Yet, since energy extraction occurs at higher frequencies, these higher harmonic tubes should present a considerable increase of the peak power density making these amplifiers even more attractive for accelerator applications. A series of two-cavity second harmonic tubes culminated in 32 MW of peak power at 19.76 GHz in the TE_{021} mode, with an efficiency of 28.6% [35,36]. A third harmonic tube was also constructed and tested, although its performance was poor, yielding 1.8 MW with an efficiency of 2% and output mode TE_{031} at 29.57 GHz [37].

A summary of results obtained with the various cylindrical gyrokystrons at the University of Maryland is presented in Table 2.

Parameter	Gyroklystron Tubes			
Harmonic	1	1	2	3
# cavities	2	3	2	2
Voltage (kV)	425	425	457	435
Current (A)	190	195	244	212
Frequency (GHz)	9.875	9.87	19.76	29.7
Power (MW)	24	27	32	1.8
Efficiency (%)	30	32	29	2
Gain (dB)	33	36	27	14

Table 2 – Summary of UMD cylindrical gyroklystrons.

Coaxial Tubes

Some preliminary investigation of coaxial tubes was performed in the 30 MW test bed in 1994. These yielded peak powers of 13 and 21 MW. However, testing of these tubes was limited by melting of the support pins [38].

After the third harmonic cylindrical study (mentioned above) was completed, the decision was made to pursue higher power levels in the 100 MW range. This goal would require a significant modification both in the beam parameters and design of microwave tubes. For practical purposes the beam voltage of 500 kV was maintained, so an increase was necessary in the beam current. A decision was made not to increase the beam current density, but rather to increase the average beam radius. As a consequence, the drift tubes would be significantly more overmoded. In order to alleviate this problem, a coaxial geometry was chosen for the microwave circuits, which led to a substantial decrease in the drift tube mode density, and in particular maintained cavity isolation for the TE_{0n1} mode at the n^{th} harmonic.

The implementation of this new system required a new electron gun and an upgrade of the modulator. Once the upgrades were completed, the study of gyrokystron tubes was resumed. A series of coaxial first harmonic tubes were tested, at about 8.6 GHz with an operating mode TE_{011} . The maximum peak power obtained was approximately 75 MW with a corresponding efficiency of 32% and gain of 29.7 dB [39]. The decrease in frequency was not a consequence of the coaxial system, but rather an attempt to conform to the practice of operating at a harmonic of the SLC frequency.

Subsequently, research began into second harmonic coaxial tubes with output in the TE_{021} mode around 17.14 GHz. A series of two three-cavity tubes were designed and built. Experimental study of these tubes was hindered by problems with the electron gun, which were responsible for the poor performance and eventual demise of the last three-cavity tube. A more detailed discussion of these issues will be presented later in this dissertation. The maximum peak power obtained with the three-cavity circuit was 27.7 MW corresponding to an efficiency of 13.3% [40].

A summary of results obtained with the coaxial gyrokystrons at the University of Maryland since 1994 is presented in Table 3.

Parameter	Gyroklystron Tubes	
Harmonic	1	2
# cavities	3	3
Voltage (kV)	469	400
Current (A)	506	515
Frequency (GHz)	8.6	17.17
Power (MW)	75	27.7
Efficiency (%)	32	13.3
Gain (dB)	29.7	24.8

Table 3 – Summary of UMD coaxial gyroklystrons since 1994

My contribution to this research consisted of designing, fabricating and testing a four-cavity frequency doubling gyroklystron. This tube will be used to drive a linear accelerator structure. Additionally, I also developed designs for an improved input cavity, a radial extraction output cavity and a circular to rectangular mode converter. These subjects will be discussed in detail later in this text.

Chapter 2 - Gyroklystron Theory and Design

2.1 Basic Theory

A gyroklystron is one type of microwave amplifying tube contained within a class of microwave devices called gyrodevices. All devices in this class take advantage of the cyclotron resonance maser instability to transfer energy from the gyrating electrons in a beam to a fast electromagnetic wave. The relationship between the electron beam and the electromagnetic fields generated within a gyrodevice is described by the cyclotron-resonance condition [25,41,42]

$$\omega = n\omega_c \pm k_z v_z, \quad (2.1)$$

where ω is the frequency of the electromagnetic field, k_z is the axial wavenumber, v_z is the axial velocity of the electrons, n is the harmonic number (an integer), and ω_c is the relativistic cyclotron frequency (defined below).

The phase velocity of the electromagnetic wave is then given by

$$v_{ph} = \frac{\omega}{k_z} = \frac{n\omega_c}{k_z} \pm v_z. \quad (2.2)$$

Thus, devices such as the gyroklystron, which can have a phase velocity greater than light, are termed fast-wave devices. In gyro-devices this is due to the cyclotron frequency term ($n\omega_c$). This effect is further enhanced in gyroklystrons by the fact that these possess a positive Doppler shift term ($k_z v_z$).

The cyclotron frequency is the rotational frequency of the electron around its guiding center given by:

$$\omega_c = \frac{eB}{m_o\gamma}, \quad (2.3)$$

where e is the electron charge, B is the magnitude of the axial magnetic field, m_o is the rest mass of an electron, and γ is the Lorentz factor of the electron, which is given by

$$\gamma = 1 + \frac{eV}{m_o c^2}, \quad (2.4)$$

where V is the voltage of the electron beam.

The radius of gyration of the electrons about the guiding center is given by the Larmor radius

$$r_L = \frac{v_{\perp}}{\omega_c}, \quad (2.5)$$

where v_{\perp} is the velocity of the electrons perpendicular to the direction of beam propagation. Since electron gyration is effectively the source of energy for the electromagnetic waves generated, the relationship between the v_{\perp} and the axial velocity of electron beam propagation (v_z) is a very important local characteristic of the beam, usually referred to as α :

$$\alpha = \frac{v_{\perp}}{v_z}. \quad (2.6)$$

Electron bunching and stimulated emission occur when interaction with the fast wave field leads to a change in the Doppler shifted cyclotron resonance frequency (2.1).

So let us start by differentiating the cyclotron condition for a fast-wave device

$$\frac{d\omega}{dt} = \frac{d}{dt}(n\omega_c + k_z v_z) = \frac{d}{dt}\left(n \frac{eB}{\gamma m} + k_z v_z\right). \quad (2.7)$$

Now let us consider the Lorentz force equation for an electron

$$\frac{d\vec{p}}{dt} = -e(\vec{E} + \vec{v} \times \vec{B}), \quad (2.8)$$

where \vec{E} and \vec{B} are the electric and magnetic fields applied on the electrons, and \vec{p} is the relativistic momentum ($\vec{p} = \gamma m \vec{v}$). The Lorentz factor γ can also be given by

$$\gamma = \frac{1}{\sqrt{1 - \frac{v^2}{c^2}}}. \quad (2.9)$$

So if we take the product

$$\vec{v} \cdot \left(\frac{d\vec{p}}{dt} = -e(\vec{E} + \vec{v} \times \vec{B}) \right), \quad (2.10)$$

then by using (2.9) we can obtain the energy relation

$$\dot{\gamma} = \frac{d\gamma}{dt} = \frac{-e}{mc^2} (\vec{v} \cdot \vec{E}). \quad (2.11)$$

Now, if we use Faraday's law

$$\vec{\nabla} \times \vec{E} = -\frac{\partial \vec{B}}{\partial t} \Rightarrow \vec{\nabla}_z \times \vec{E}_\perp + \vec{\nabla}_\perp \times \vec{E}_z + \frac{\partial \vec{B}}{\partial t} = 0 \quad (2.12)$$

and assume a TE mode interaction, we can derive the expression

$$\vec{B}_\perp = \frac{k_z}{\omega} \hat{z} \times \vec{E}_\perp \quad (2.13)$$

relating the transverse \vec{E} and \vec{B} fields for the TE waveguide mode.

Finally, let us consider also the \hat{z} component of the Lorentz force

$$\hat{z} \cdot \left(\frac{d\vec{p}}{dt} = -e(\vec{E} + \vec{v} \times \vec{B}) \right). \quad (2.14)$$

By substituting (2.13) into (2.14), and then (2.14) and (2.11) into (2.7) we can get

$$\frac{d\omega}{dt} = \frac{-ek_z^2}{m\gamma\omega} \left[1 - \frac{\omega^2}{k_z^2 c^2} \right] (\vec{v}_\perp \cdot \vec{E}_\perp) \equiv (\theta_1) - (\theta_2), \quad (2.15)$$

This equation contains two terms (θ_1) and (θ_2) . The first term (θ_1) derives entirely from the variation in the axial velocity and it describes electron phase bunching in the axial (z) direction [43]. This term gives rise to the Weibel instability [43]. The second term (θ_2) , arises in part from the change in the energy of the electrons ($dE/dt \sim d\gamma/dt$) due to their cyclotron oscillation. This term describes azimuthal phase bunching, and it gives rise to the cyclotron resonance Maser (CRM) instability [15,44,45]. Notice that in the fast-wave regime ($\omega > k_z c$), in which gyrokystrons operate, the CRM term dominates the axial bunching term. The dispersion relation for cyclotron resonance masers (in the absence of spread) is given by [43]

$$\omega^2 - k_z^2 c^2 = \frac{\omega_p^2}{\gamma} \left(\frac{\omega}{\omega - \omega_c} - \frac{v_\perp^2 (\omega^2 - k_z^2 c^2)}{2c^2 (\omega - \omega_c)} \right), \quad (2.16)$$

where ω_p is the plasma frequency, which is defined by

$$\omega_p^2 = \frac{4\pi \cdot n_e e^2}{m_0}, \quad (2.17)$$

where n_e is the electron number density.

The gyrokystron tubes that we have recently studied at the University of Maryland utilize highly relativistic beams (500 keV, $\gamma = 2$) interacting with modes well above cutoff. Thus, the Doppler term is not negligible. This is significant because as this term increases the axial velocity spread in the electron beam will lead to electrons which do not satisfy the cyclotron condition for a given electromagnetic mode.

Therefore, there will be a reduction in the strength of the interaction between the beam with the microwaves generated and a subsequent reduction in conversion efficiency.

2.2 Design Methodology

The active region of a gyrokystron, the region located between the input and output cavities - in which the particles and electromagnetic waves interact - is called the microwave circuit or tube. This region is split into a series of alternating cross sectional segments called cavities and drift regions. Cavities are resonant structures, regions where the beam actively interacts with electromagnetic waves. A gyrokystron has at least two cavities: an input cavity where the beam is exposed to an external drive signal, and an output cavity where the beam generates an amplified (and possibly multiple harmonic) version of the input signal. Extra cavities can be added between the input and output cavities (such is the case of the circuit discussed in this study) to further bunch the beam, increasing the overall gain and perhaps efficiency of the circuit. In theory, the cavities have abrupt discontinuities at the boundaries, being electromagnetically insulated from one another and physically separated by drift regions, that are void of electromagnetic energy. In reality though, electromagnetic fields from cavities do leak into the drift regions, possibly exciting spurious modes there. Therefore, one important concern is to minimize any kind of direct electromagnetic interaction between adjacent cavities (“cross-talk”) which could impair the optimal operation of the circuit, leading to degradation of efficiency and gain of the circuit, and compromising zero-drive stability. The importance of drift regions becomes clear: these regions are conceived so as to permit electron beam passage with the least possible interaction with

electromagnetic waves. Thus they are designed so as to be cut-off regions for the operating electromagnetic modes excited in any cavities of the circuit. Nonetheless, they represent an important part of the beam formation, as the electrons bunch ballistically.

Cold cavity design

The expression “cold cavity” refers to the absence of free charges (ρ) and currents (\vec{J}) within a given microwave structure, thus ρ and \vec{J} are zero. The electromagnetic properties of each of the cavities must be studied in the absence of an electron beam. This is the first stage for designing the microwave circuit. This procedure is performed using the code COAX [46,47]. In using COAX, one starts with a geometric description of a given cavity along with adjacent drift areas, as seen on Fig.1.

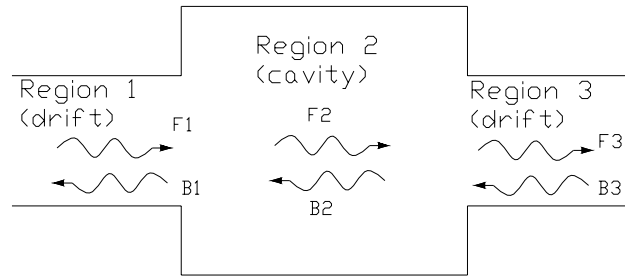


Figure 1 – Diagram of the model for a given gyrokystron cavity.

The code then considers each constant waveguide section of the input geometry as a separate region. The transverse \vec{E} and \vec{H} fields in a given region κ are expressed as a finite sum over a set of orthogonal eigenmodes $e_{i\alpha}$ and $h_{i\alpha}$ of the waveguide in the region:

$$\vec{E}_\kappa = \sum_{i=1}^M \vec{E}_{i\kappa} = \sum_{i=1}^M A_{i\kappa} \vec{e}_{i\kappa} \quad , \quad (2.18)$$

$$\vec{H}_{i\kappa} = \sum_{i=1}^M \vec{H}_{i\kappa} = \sum_{i=1}^M I_{i\kappa} \vec{h}_{i\kappa} \quad . \quad (2.19)$$

Furthermore, each of these modes e and h has two components: a forward wave (propagating in the $+z$ direction) and a backward wave. Hence, the transverse fields \vec{E} and \vec{H} in region κ can be written

$$\vec{E}_\kappa = \sum_{i=1}^M (F_{i\kappa} + B_{i\kappa}) \vec{e}_{i\kappa} \quad (2.20)$$

$$\vec{H}_\kappa = \sum_{i=1}^M \left(\frac{F_{i\kappa} - B_{i\kappa}}{Z_{i\kappa}} \right) \vec{h}_{i\kappa} \quad (2.21)$$

where F and B are the modal amplitudes of the forward and backward components respectively, while $Z_{i\kappa}$ is the characteristic impedance of the i^{th} eigenmode of region κ , defined by

$$Z_{TE} = \frac{\omega\mu_0}{k_z}; Z_{TM} = \frac{k_z}{\omega\varepsilon_0}, \quad (2.22)$$

where μ_0 and ε_0 are the free space magnetic permeability and electric permittivity, respectively. The expansions of \vec{E} and \vec{H} for two adjacent regions can be related by boundary conditions. The continuity of the tangential \vec{E} and \vec{H} fields across the interface of the two regions, along with the condition that the tangential \vec{E} field be zero on the wall of the larger cross section waveguide yield the following relations:

$$P[\underline{F}_1 + \underline{B}_1] = I[\underline{F}_2 + \underline{B}_2], \quad (2.23)$$

$$Z_1 P^T Y_2 [\underline{F}_2 - \underline{B}_2] = I[\underline{F}_1 - \underline{B}_1], \quad (2.24)$$

where F and B are vectors containing the amplitude coefficients (F_1, \dots, F_k) and (B_1, \dots, B_k) for regions 1 or 2. Z_1 and Y_2 are diagonal matrices of modal impedance for region 1 and modal admittance for region 2 respectively; while I is the identity matrix. P is the mode coupling (MC) matrix, whose elements are generated by expressing the eigenmodes in one region in terms of the eigenmodes of the other one,

$$P_{ji} = \int_S \vec{e}_{j2} \cdot \vec{e}_{i1}^* dS \quad (2.25)$$

thus effectively describing which modes in one region couple to modes in the other.

From this equation it can be demonstrated that, in the case of either cylindrical or coaxial systems, modes of different azimuthal eigenvalues will not couple across from one region to the other [47]. Additionally, TM modes in the smaller region (region 1 in Fig.1) do not couple to TE or TEM modes in the larger region (region 2); and TE modes do not couple to the TEM mode.

The forward and backward wave amplitudes for the two adjacent regions can be related by the scattering matrix:

$$\begin{pmatrix} \underline{B}_1 \\ \underline{B}_2 \end{pmatrix} = \begin{pmatrix} S_{11} & S_{12} \\ S_{21} & S_{22} \end{pmatrix} \begin{pmatrix} \underline{F}_1 \\ \underline{F}_2 \end{pmatrix}. \quad (2.26)$$

We can utilize the expressions (2.23) and (2.24) to solve for the components of the scattering matrix, obtaining

$$S_{11} = [I + Z_1 P^T Y_2 P]^{-1} [I - Z_1 P^T Y_2 P], \quad (2.27)$$

$$S_{12} = 2[I + Z_1 P^T Y_2 P]^{-1} Z_1 P^T Y_2, \quad (2.28)$$

$$S_{21} = 2[I + P Z_1 P^T Y_2]^{-1} P, \quad (2.29)$$

$$S_{22} = -[I + P Z_1 P^T Y_2]^{-1} [I - P Z_1 P^T Y_2]. \quad (2.30)$$

If a given configuration possesses more than two regions, the scattering matrices are cascaded from the central cavity region outwards to the left and right. The outermost scattering matrices are determined by the boundary conditions at the ends, being either matched waveguide sections ($S_{11} = 0$) or shorted sections ($S_{11} = -I$). The two resulting matrices S^L and S^R describe the combined effect of cascading scattering matrices towards the left and right of the central cavity region, respectively. Therefore, the relationships between the forward and backward wave amplitudes in the left and right sides of the cavity region can be expressed by

$$\underline{B}^R = S_{11}^R \underline{F}^R, \quad (2.31)$$

$$\underline{B}^L = S_{11}^L \underline{F}^L, \quad (2.32)$$

Notice that $F^R = B^L$ and $F^L = B^R$, as guaranteed by the continuity condition in the center of the cavity. Combining the equations (2.31) and (2.32) we obtain the matrix equation

$$\underline{B}^R = S_{11}^R S_{11}^L \underline{B}^R, \quad (2.33)$$

which yields

$$\det(S_{11}^R S_{11}^L - I) = 0. \quad (2.34)$$

Solving this eigenvalue equation by a two-dimensional search in complex frequency space will allow the COAX code to obtain the resonant frequency and corresponding quality factor Q of the cavity, which are related by

$$Q = \frac{1}{2} \frac{\text{Re}(\omega)}{\text{Im}(\omega)}. \quad (2.35)$$

Large Signal Analysis

After studying the “cold-cavity” properties of a given section of the microwave circuit, we need to model the behavior of the whole microwave circuit in the presence of the electron beam. This study is commonly referred to as “large signal” (or “hot”) analysis, and it involves solving fairly complex equations that describe the interaction of electromagnetic fields with the electrons that make up the beam. This modeling is performed using the computer code MAGYKL, which is the upgraded version of an earlier code called GYCOAX [48].

The relationship between the fields and the current density \vec{J} of the electron beam is given by the time harmonic Maxwell equations

$$\vec{\nabla} \times \vec{E} = -j\omega\mu_0\vec{H}, \quad (2.36)$$

$$\vec{\nabla} \times \vec{H} = j\omega\varepsilon_0\vec{E} + \vec{J}, \quad (2.37)$$

where ω is the fundamental frequency of the electromagnetic waves. Now, the cold cavity modes \vec{E}_i and \vec{H}_i mentioned in the previous section (see (2.18) and (2.19)) form a complete set, hence the hot cavity fields \vec{E} and \vec{H} can be expressed as a sum of \vec{E}_i and \vec{H}_i

$$\vec{E} = \sum_i a_i \vec{E}_i, \quad (2.38)$$

$$\vec{H} = \sum_i b_i \vec{H}_i, \quad (2.39)$$

where \vec{E}_i and \vec{H}_i satisfy Maxwell's equations with the absence of the excitation term \vec{J} :

$$\vec{\nabla} \times \vec{E}_i = -j\omega_i\mu_0\vec{H}_i, \quad (2.40)$$

$$\vec{\nabla} \times \vec{H}_i = j\omega_i \epsilon_0 \vec{E}_i. \quad (2.41)$$

Substituting the expressions (2.38) and (2.39) into the equations (2.36) and (2.37), in combination with (2.40) and (2.41) we get

$$\sum_i \frac{\omega_i}{\omega} a_i \vec{H}_i = \sum_i b_i \vec{H}_i, \quad (2.42)$$

$$\sum_i \omega_i \epsilon_0 b_i \vec{E}_i = w \sum_i \epsilon_0 a_i \vec{E}_i - j\vec{J}. \quad (2.43)$$

Next, let us multiply (2.42) by \vec{H}_j^* , integrating over the volume of the cavity. Due to mode orthogonality we get

$$b_j = \frac{\omega_j}{\omega} a_j. \quad (2.44)$$

Similarly, we repeat this procedure with (2.43) multiplying it by \vec{E}_j^* , integrating over the cavity volume. Mode orthogonality and (2.44) leads us to

$$a_j = \frac{1}{\frac{\Delta\omega_j}{\omega} (\omega + \omega_j) \epsilon_0} \frac{j \int_{cavity\ volume} \vec{J} \cdot \vec{E}_j^* dV}{\int_{cavity\ volume} \vec{E}_j \cdot \vec{E}_j^* dV}. \quad (2.45)$$

where $\Delta\omega_j$ is the frequency shift between the the operating mode and the resonant frequency of the j^{th} natural mode

$$\Delta\omega_j = \omega - \omega_j. \quad (2.46)$$

Clearly, the excitation amplitude a_j will be large for a mode whose frequency is near that of the driving signal. At $\omega = \omega_j$, a mathematical singularity takes place. However, a real cavity has a finite quality factor (Q) and will not respond with an infinite

amplitude. The quality factor (Q) of a cavity for a given mode of frequency ω_i is given by the usual expression

$$Q_i = \frac{1}{2} \frac{\text{Re}(\omega_i)}{\text{Im}(\omega_i)}. \quad (2.47)$$

And its effect can also be described by the expression

$$\omega_i = \omega_{iR} \left(1 \pm \frac{j}{2Q_i} \right). \quad (2.48)$$

where ω_{iR} is the real resonant frequency of the i^{th} mode, and Q_i its associated quality factor. Assuming that 1) each cavity of our gyrokystron circuit is driven at a frequency very near the resonant frequency of the design mode (ω_0), and 2) the design mode frequency of each cavity is well separated from other modes; it follows that the amplitudes a_i of all other modes should be much smaller than the amplitude of the design (mode which we will denote as A) Therefore we can reduce the expansions (2.38) and (2.39) to only one term each

$$\vec{E} = A\vec{E}_0. \quad (2.49)$$

$$\vec{H} = A \frac{\omega_0}{\omega} \vec{H}_0. \quad (2.50)$$

where \vec{E}_0 and \vec{H}_0 are the natural fields of the cavity design mode. The amplitude A can be obtained from (2.45) along with (2.49) and (2.48), yielding

$$A = \frac{1}{\frac{(\omega - \omega_0)}{\omega} (\omega + \omega_0)} \frac{\int_{\text{cavity volume}} \vec{J} \cdot \vec{E}_0^* dV}{\epsilon_0 \int_{\text{cavity volume}} \vec{E}_0 \cdot \vec{E}_0^* dV}. \quad (2.51)$$

If we now time average this expression over one oscillation period ($T = 2\pi/\omega$), and use equation (2.48) in the large Q limit ($Q \gg 1$, which implies $\text{Im}\{\omega_0\} \ll \text{Re}\{\omega_0\}$ and $\text{Re}\{\omega_0\} = \omega_{0R} \approx \omega$), we arrive at

$$A = \frac{-Q}{2\omega \left(\frac{1}{2} + j\Delta_\omega \right)} W_{EM} \int_{\text{cavityvolume}} dV \langle \vec{J} \cdot \vec{E}_0^* \rangle_t, \quad (2.52)$$

where

$$\Delta_\omega = Q \frac{\omega_{0R} - \omega}{\omega} \quad (2.53)$$

is the normalized frequency shift, and

$$W_{EM} = \frac{\epsilon_0}{2} \int_{\text{cavityvolume}} dV \langle \vec{E}_0 \cdot \vec{E}_0^* \rangle_t, \quad (2.54)$$

is the field energy. The time average over one period is denoted by

$$\langle \dots \rangle = \frac{1}{T} \int_0^T (\dots) dt. \quad (2.55)$$

In addition to solving (2.52), which allows us to determine the fields in a given cavity of the gyrokystron, the code MAGYKL must also solve equations that describe the motion of electrons in the beam. These are derived from the relativistic Lorentz force equation of the form

$$\frac{d\vec{p}}{dt} = -e \left[\vec{E} + \vec{\beta} \times (\vec{B} + \vec{B}_E) \right], \quad (2.56)$$

where \vec{p} is the electron momentum and $\vec{\beta} = \vec{v}/c$ is the normalized velocity of the particle. As before, \vec{E} and $\vec{B} = \mu_0 \vec{H}$ are the “hot” cavity fields given by (2.49) and (2.50), and \vec{B}_E is the external magnetic field.

The equations (2.52) and (2.56) constitute a complete set, and in the case of the nonlinear regime must be integrated numerically.

The solution of this set of equations must fulfill a self-consistency requirement. This condition is that the current density which produces the electromagnetic fields (2.52) must be the same as the current density which is produced by the fields (2.56). This condition can be written as

$$\left(\frac{1}{2} + j\Delta_\omega\right)A = -I\mathcal{G}(|A|, \phi), \quad (2.57)$$

where g is the complex gain function, ϕ is the wave phase ($A = |A| e^{j\phi}$) given with respect to the input cavity ($\phi = 0$ at the entrance of the input cavity), and I is the normalized current, which is given by

$$I = \frac{Q_0}{2\beta_{z0}} \frac{I_b}{I_a} \frac{1}{W_0}, \quad (2.58)$$

I_b is the beam current, I_a is the Alfvén current [49] and W_0 is the normalized field energy. Canceling the factor of A from both sides, and separating real and imaginary parts we arrive at

$$\frac{1}{2} = -I g_R(|A|, \phi), \quad (2.59)$$

$$\Delta_\omega = -I g_I(|A|, \phi), \quad (2.60)$$

where g_R and g_I are the real and imaginary parts of the gain function. It can be shown that equation (2.59) can be rewritten using the equations of motion (please see reference [48] for a more rigorous discussion), yielding

$$|A|^2 = I \eta_\perp(|A|, \phi). \quad (2.61)$$

In this equation, η_{\perp} is the perpendicular efficiency, which is related to the total efficiency η (fraction of the electron's energy that is given up to the electromagnetic fields) by

$$\eta = \frac{\gamma_0 + 1}{2\gamma_0} \frac{\alpha_0^2}{\alpha_0^2 + 1} \eta_{\perp}, \quad (2.62)$$

where γ_0 is the initial average relativistic factor and α_0 is the initial velocity pitch ratio.

Now, we can contemplate how to design a gyrokystron using the code MAGYKL. The geometry of a cavity determines its Q and resonance frequency f_r (something which can be computed using the code COAX), which in turn with the beam parameters (such as potential, current, guiding radius, and a few others) determines the normalized current I and normalized frequency shift Δ_w , from which the wave amplitude $|A|$ and phase ϕ can be calculated (using (2.60) and (2.61)). So MAGYKL takes the complex amplitude and phase of cold cavity fields as an input, and calculates the normalized current and frequency shift for a beam with specific parameters. From I and Δ_w values of Q for the different cavities can be computed, and they are matched to the cold cavity Q 's. Once this self-consistency condition (expressed now in terms of Q) is fulfilled, the efficiency and gain of the circuit can be calculated.

The amplitudes and relative phases of the fields in each of the cavities can be easily altered so as to maximize the efficiency of the circuit while matching the Q 's. Thus, MAGYKL varies the values of the amplitude and phase in each cavity calculating an error term by comparing sequential iterations. The code tries to minimize the error term (until it reaches a specified minimum), accordingly making new guesses for A and ϕ . Once the search converges to a steady-state set of values for A and ϕ which fulfill the

self-consistency condition for the Q of the cavity, then the code moves on to the next cavity and repeats the same procedure.

Stability of Cavities

An important criterion in the design of a microwave amplifier, such as the gyrokystron, is zero-drive stability. This property guarantees that there is only output power from the tube while the driver for the circuit is on, so that there are no self-oscillations taking place at the operating regime of the tube. Self-oscillations are problematic, for they affect mode and phase purity of the output signal (which is crucial for accelerator applications), effectively reducing the efficiency and gain of the amplifier, and leading also to local field enhancement and the possibility of breakdown. In order to avoid this scenario, we studied the potential for self-oscillation in each cavity of our design using the computer code QPB.

This code calculates the product of the quality factor Q of a given cavity and the beam power (thus the name QPB). Based on this quantity we can calculate the threshold for the onset of self oscillation, either by considering a fixed value of Q for the cavity and calculating the start of oscillation current (I_{so}) with

$$I_{so} = \frac{(Q \cdot P_b)_{so}}{QV_b}, \quad (2.63)$$

where P_b and V_b are the beam power and voltage respectively; or alternatively, we can consider the beam current constant, and calculate the value of the start of oscillation Q

$$Q_{so} = \frac{(Q \cdot P_b)_{so}}{V_b I_b}, \quad (2.64)$$

Hence, we can alter the beam parameters or the characteristics of a given cavity in order to remain in a regime away from self-oscillations.

In order to get a better understanding about the calculation of QPB , we can multiply equation (2.52) by the complex conjugate of A obtaining

$$|A|^2 = \frac{Q}{2\omega \left(\frac{1}{2} + j\Delta_w \right) W_{EM}} \int_{cavityvolume} dV \langle \vec{J} \cdot (A^* \vec{E}_0^*) \rangle_t, \quad (2.65)$$

Now, if we use equation (2.49) we notice that the integral in the right hand side of the previous expression is simply the average power coupling between the beam and the electromagnetic field, that is

$$\int_{cavityvolume} dV \langle \vec{J} \cdot (A^* \vec{E}_0^*) \rangle_t = \int_{cavityvolume} dV \langle \vec{J} \cdot \vec{E}^* \rangle_t = \eta P_b, \quad (2.66)$$

where η is the efficiency and P_b is the beam power ($P_b = V_b \cdot I_b$). Consequently, we can write (2.65) as

$$|A|^2 = \frac{Q}{2\omega \left(\frac{1}{2} + j\Delta_w \right) W_{EM}} \eta P_b, \quad (2.67)$$

Now, in the case of self-oscillation $\omega \approx \omega_0$, so $\Delta_w \approx 0$, and we get

$$|A|^2 = \frac{Q}{\omega W_{EM}} \eta P_b, \quad (2.68)$$

We can combine (2.61), (2.62) and (2.59) with the previous equation to get

$$(Q \cdot P_b)_{SO} = \frac{\omega}{2} \frac{2\gamma_0}{\gamma_0 + 1} \frac{\alpha_0^2 + 1}{\alpha_0^2} \frac{W_{EM}}{g_R}, \quad (2.69)$$

where g_R is the real component of the complex gain function.

This gain function can in turn be calculated by QPB using a generalized form of Madey's theorem (a rigorous discussion and derivation can be found in [50]).

Overall Design Procedure

The design of a gyrokylystron circuit starts with the experimental constraints dictated by the equipment available (primarily the gun specifications and driver signal source) and the specific application envisioned. The stable operating voltage and current of the beam produced by the electron gun are particularly important. This information, along with geometric details of the configuration of gun electrodes (please see Table 4) and external magnetic field values, is necessary for us to compute various beam parameters with the computer code EGUN. EGUN calculates electron trajectories, from which quantities such as axial velocity spread and alpha can be determined. These will be required for both MAGYKL and QPB simulations.

Parameter	30 MW system	100 MW system
Nominal Current, I_b (A)	160	600
Max. Current Density, J_c (A/cm ²)	6.98	7.95
Nominal Voltage, V_b (kV)	500	500
Cathode Radius, r_c (cm)	2.28	7.15
Outer Drift Tube Radius, r_o (cm)	1.5	3.325
Inner Drift Tube Radius, r_i (cm)	---	1.825

Table 4 - Gun parameters for gyrokylystron systems at UMD.

After that preliminary work, we define the geometries of each of the cavities by trial-and-error using the code COAX. Once a specific cavity design yields the target Q and resonant frequency, we use QPB to determine if the cavity is zero-drive stable with the planned beam parameters. This procedure is repeated for each cavity in the circuit.

Then we run the code MAGYKL with data from the output files of COAX for all cavities in the gyrokystron circuit. MAGYKL computes the overall efficiency of the gyrokystron based on the characteristics of the cavities, the parameters of the electron beam and the external magnetic field profile applied on the circuit. In order to maximize the efficiency one can usually vary several quantities:

- 1) The input drive power or frequency;
- 2) The magnetic field profile applied to the circuit;
- 3) The drift lengths between the cavities in the circuit;
- 4) The Q or cold-frequency of a given cavity → requiring repeat of cavity study with COAX and check for stability with QPB.
- 5) The beam parameters (V_b , I_b , α) → requiring repeat of QPB stability check and possibly EGUN studies;

This can lead to a very complex and time consuming search for an optimal overall circuit design.

Chapter 3 – Experimental Setup

3.1 System Overview

Experimental implementation of such high power microwave devices, as described herein, is a very challenging enterprise. This requires a complex setup, in which every aspect of the system must be carefully designed and constructed. A conceptual diagram of the gyrokylystron and its supporting/auxiliary systems is seen in Fig. 2.

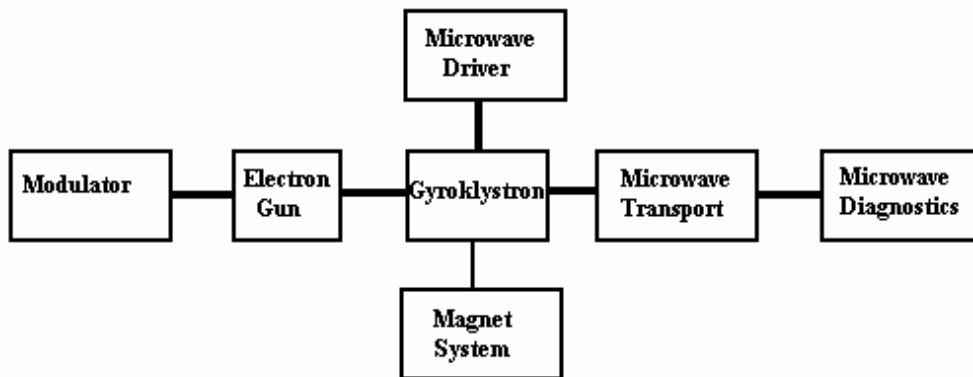


Figure 2 – Representation of the gyrokylystron subsystems.

The fundamental components necessary for the operation of the GKL are:

- a) Modulator
- b) Electron gun
- c) Magnet system
- d) Beam and Microwave Transport System
- e) Input Power System
- f) Microwave Diagnostics

An overview of this entire system is warranted so as to demonstrate how these various components are integrated into a whole. A schematic of the entire gyrokystron experimental setup is displayed in Fig. 3.

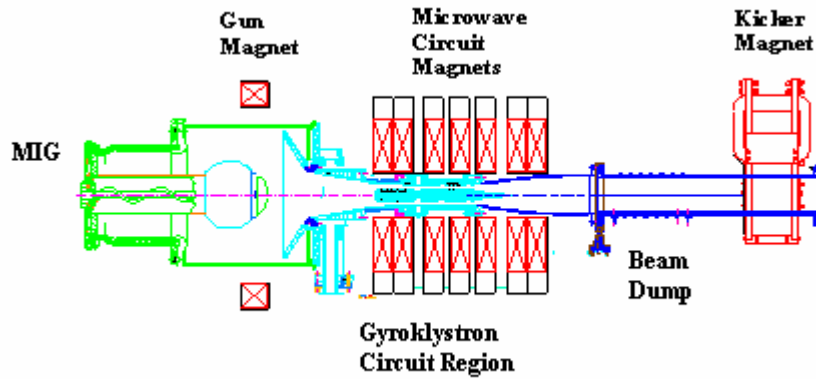


Figure 3 – Experimental test-bed.

The modulator is the source of power for the electron gun, it produces an electric pulse with the appropriate voltage, current and duration to initiate the production of an electron beam. The electrons in the beam acquire rotational momentum due to the presence of a magnetic field in the gun region.

The beam then travels through the gyrokystron circuit. Simultaneously, the microwave driver produces a signal which is injected into the input cavity of the GKL. While passing the input cavity of the gyrokystron, the electron beam is exposed to electromagnetic fields induced therein due to the injected input power. As a consequence of this interaction, the individual electrons in the beam experience a force which leads to azimuthal bunching of the beam.

The bunched beam interacts with the remaining cavities of the GKL, under the influence of a stationary magnetic field. At the output cavity, an amplified microwave signal is produced and exits the circuit axially along with the spent electron beam. As

the electron beam exits the region of high magnetic field, it loses its magnetic confinement and the beam expands until it impacts with the beam pipe wall at the "beam dump" region. Any remaining stray electrons that still remain in the beam pipe are forced into the wall by action of the field of a kicker magnet. Meanwhile, the output power is transported through a series of tapers into an anechoic chamber where it can be sampled and studied.

I will now present a more detailed description of these major subsystems of our experiment.

3.2 The Modulator

The high voltage modulator and its associated circuitry were originally designed and built by W. Lawson and J. Calame, and are described in detail in J. Calame's Master's thesis [51]. The original specifications were for 500 kV, 400 A pulses for 1 μ s and a repetition rate of up to 5 Hz.

It has undergone significant upgrades since its original conception. The modulator had been originally designed to power a 30MW gyrokystron system with a double-anode MIG (magnetron injection gun), hence the modifications were necessary when the gyrokystron system was upgraded to support 100MW level tubes with a single-anode MIG. Most noteworthy alterations were (1) the addition of a second tank of Pulse Forming Network (PFN) banks so as to double the current to the transformer tank, and (2) changes to the electric circuitry in the transformer tank so as to accommodate the single-anode MIG. A diagram of the current modulator can be seen in Fig. 4.

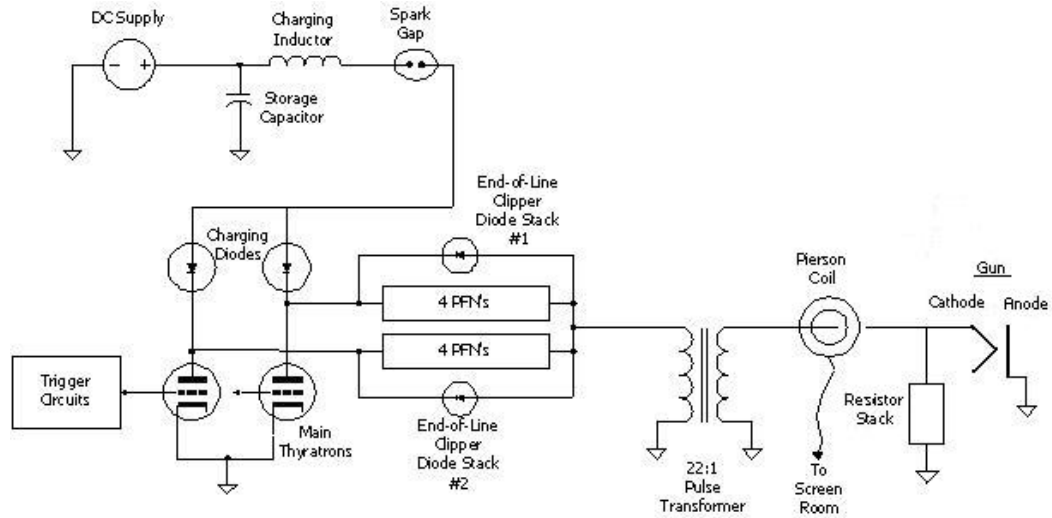


Figure 4 –Modulator circuitry.

The basic components of the current modulator are: a DC high voltage supply, a spark gap, high voltage thyatron switches, eight pulse forming networks (PFN) and a high voltage pulse transformer.

At the core of the modulator are eight PFN's connected in parallel. Each of these PFN's has an impedance of 10 ohms and is composed of 12 stages of LC circuits [51]. The PFN discharge is initiated by two deuterium thyratrons.

Since the impedance of the electron gun can vary (primarily due to the temperature of the thermionic emitter), a series of resistor stacks are connected in parallel with the electron gun. The overall resistance of the stacks can be easily changed by rewiring the resistor stacks. This allows us to maintain a matched load at the output of the modulator even if the impedance of the electron gun changes.

Recently, the modulator has undergone yet another significant upgrade. The current resonant charging system has been replaced with a modern high voltage

switching supply module, the Lambda-EMI 802L 50kV capacitor charging supply. This supply will charge the PFN more uniformly and more reliably from one cycle to the next. This upgrade will allow us to charge the capacitor banks of the Pulse Forming Network (PFN) to a consistent voltage from one charge cycle to the next, which is crucial for us to obtain more stable voltage pulses so as to produce repeatable pulse-to-pulse characteristics. Such high quality beams will be important for overall improved performance of the GKL, and are imperative for greater phase and amplitude control. These are essential requirements for future studies in accelerator drive. With an average charging rate of 8000 J/s at 50 kV, the supply will enable us to charge/discharge the PFN at a rate of approximately 5 Hz and have pulse-to-pulse variations less than 0.1%.

3.3 The Electron Gun

The electron gun is at the center of all of our gyrokystron experiments. This device is the source of the high-quality annular electron beam that we use for microwave amplification. Magnetron Injection Guns (MIG) are the most common guns used in gyrotron and gyrokystron devices [52].

Our gun is a single anode MIG, which was designed to produce a 250-360 MW electron beam with an alpha value of 1.5 while minimizing the velocity spread [48]. Velocity spread is a natural characteristic of real particle beams which increases with alpha and the current of the beam, and which has been shown to have a detrimental effect on the efficiency of operation of gyro-devices. The design for our MIG allowed for a velocity spread below 10% for an alpha of 1.5 and a beam current of 720 A (which were original design parameters of the first gyrokystron tubes used with this gun).

Figure 5 is a printout of EGUN displaying a cross sectional view of the MIG and a typical r-z projection of the beam trajectory. The MIG was designed to operate below its space-charge limit so as to optimize beam quality. Detailed specifications of the gun design can be seen in Table 5.

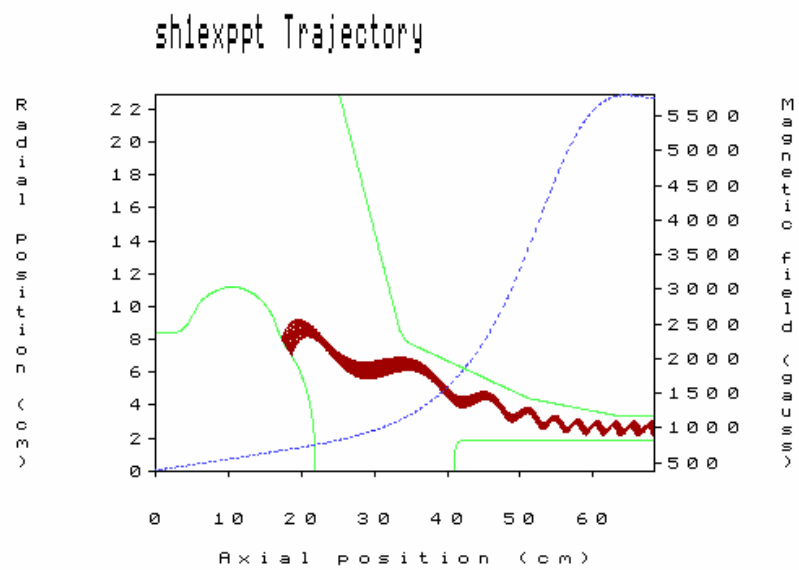


Figure 5 - Typical beam emission from MIG (EGUN)

Electrode Specifications		Simulated Results	
Cathode Radius (cm)	7.49	Cathode Loading (A/cm ²)	5.80
Cathode Half-Angle (deg)	35-39	Compression Ratio	7.55
Emitter Strip Width (cm)	2.30	Thickness (cm)	1.26
A-K gap (cm)	13.9	Space-Charge Limit (A)	1975
Emitter Strip Length (cm)	1.35	Voltage (kV)	500
		Current (A)	480-800
		Velocity Ratio	1.5
		Axial Velocity Spread	6.4%
		(at 480 A)	
Peak E-fields (kV/cm)			
Cathode	91.6		
Anode	26.1		
Emitter	63.8		

Table 5 - Specifications of the electron gun.

The coaxial gyroklystron requires an annular electron beam in which individual electrons undergo rotational motion about their equilibrium position in the overall beam (see Fig. 6) - as the beam moves downstream from the electron gun through the microwave circuit. In order to achieve this, a magnetic field coil is placed outside the gun, centered at the axial location of the emitter. The presence of the magnetic field produced by this coil, in conjunction with the convergent path of the electrons in the region between the cathode and anode, lead to the acquisition of angular momentum by electrons in the beam.

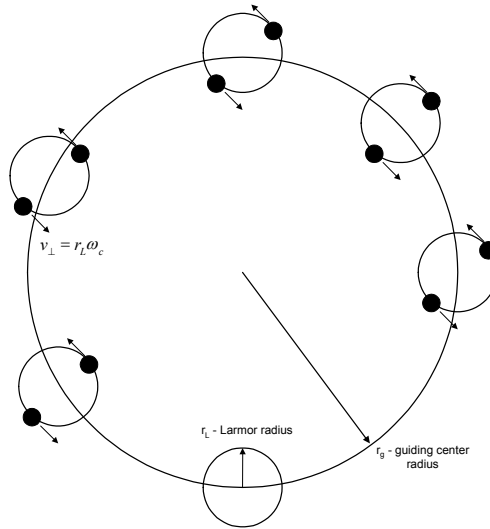


Figure 6 - Cross section of small orbit gyrotron electron beam

The cathode of the MIG possesses a thermionic barium-dispenser emitter. The emitter consists of a tungsten matrix, impregnated with a 6:2:1 mixture of barium oxide, calcium oxide, and alumina. The emitter contains a spiral heating element, behind the emitter surface, to bring the temperature to approximately 1000° C. It is important that the heating be homogeneous along the whole surface of the emitter, so as to ensure the uniformity of the electron emission and therefore of the electron beam. This key element of our MIG has been found to be problematic. I will discuss this point further in Chapters 5 and 9.

3.4 The Magnet System

The magnet system of the gyrokystron is comprised of eight solenoidal pancake magnets and one kicker magnet. These are water-cooled and capable of producing magnetic fields of more than 0.5 T. One magnet (the gun magnet) is located around the

electron gun (as mentioned earlier), while the other seven magnets are placed along the region of the microwave circuit. This configuration can be seen in Fig. 3 which displays the experimental test-bed.

There are four independent power supplies used to energize the magnets: one controls the gun magnet while the remaining three supplies power the seven circuit magnets (one supply controls three adjacent magnets, while the other two supplies power two magnets each). This flexibility in the control of the magnetic field gives us the ability to (a) control the magnetic compression at the entrance of the microwave circuit (which in turn allows us to set the alpha parameter for the gyrokystron), as well as (b) to adjust the cyclotron tune in the regions of the microwave cavities. Control over these parameters helps us maximize the efficiency of the gyrokystron circuit.

Finally, the last component of the magnet system is the kicker magnet. This magnet has a nominal field of 800 G and it is necessary to remove any stray electrons that remain after the beam dump (further explanation follows in the next topic).

3.5 Beam and Microwave Transport System

The first component of the beam transport system is a downtaper that connects the gate valve at the end of the MIG (radius=10.16 cm) to the microwave circuit (radius=3.4 cm). Within this downtaper, the beam undergoes adiabatic compression. The taper has been designed to reduce the possibility of spurious oscillations in this region. To this effect, several microwave absorbing ceramic (both carbon-impregnated aluminum-silicate (CIAS) and the BeO/SiC) rings are utilized to line the inner surface of the taper.

After this taper the beam travels through the microwave circuit. Finally the beam, accompanied by a microwave pulse generated in the output cavity of the gyrokystron, passes through a small uptaper designed to adjust the beam pipe radius from 3.4 cm to 6.35 cm, which is the diameter of the beam dump region. The microwave tube and small uptaper will be discussed in detail in Chapter 4.

The beam dump, as the name indicates, is the region of the system in which the electron beam is terminated. In our experiment we use high-energy electron beams (500 keV), hence as the beam terminates by impacting the walls of the beam pipe it produces a significant amount of x-ray radiation by bremsstrahlung. Thus the beam dump was carefully designed to absorb the x-ray flux: a 3" layer of lead surrounds this chamber to provide shielding from the radiation produced.

The termination of the beam also produces heating due both to scattering and ohmic phenomena. Therefore, the beam dump is cooled by water flowing through channels in its exterior wall.

As mentioned above, a kicker magnet at the end of the beam dump ensures that any remaining stray electrons are forced into the beam pipe wall. Once the electron beam disappears, the output microwave pulse continues its journey by passing through an alumina (Al_2O_3) window. This window serves as the boundary between the ultra-vacuum contained in the gun-microwave regions and atmospheric pressure. The window has a radius of 6.35 cm and a thickness of 0.575 cm, which was designed to be half the wavelength of TE_{01} mode at 8.568 GHz, so as to minimize reflections of this mode and its multiple harmonics. The reflection coefficient for the TE_{01} mode at 8.568 GHz is 6.7×10^{-5} and for the TE_{02} mode at 17.11 GHz is 0.0051.

After the window, the microwaves travel along a large uptaper and enter the anechoic chamber where this electromagnetic signal is detected and analyzed.

3.6 Input Power System

A diagram of the entire input power system is presented in Fig. 7. The input power for the gyrokylystron is provided by a coaxial magnetron built by Varian. This magnetron can be mechanically tuned from 8.47 to 8.70 GHz and produces 2-2.5 μ s pulses with a maximum peak power of 150 kW.

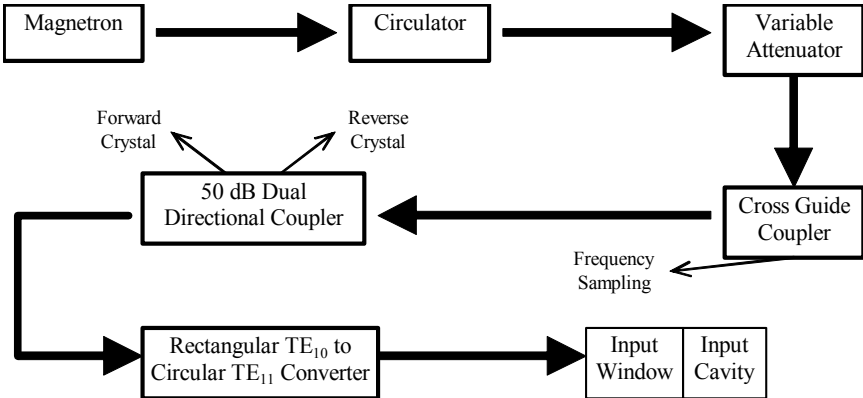


Figure 7 – Diagram of input power system.

The output of the magnetron travels through a series of waveguides and a circulator (which provides protection from large reflections coming from the input cavity to the gyrokylystron), and through a 50 dB dual-directional coupler. Both sampling ports of this coupler are fitted with diode crystals that allow us to measure the forward (towards the gyrokylystron) and reflected (back from the gyrokylystron) drive

power. The entire input power waveguide system is filled with sulfur hexafluoride (SF_6) so as to minimize the possibility of electrical breakdown in the line.

The magnetron power is then injected into the input cavity of the gyrokystron through two identical alumina windows that are placed at the end of the input waveguide system. One of the windows serves as the interface between the vacuum and the sulfur hexafluoride (near atmospheric pressure). The function of the second window is to compensate for some of the mismatch between the window and slot on the input cavity. The distance between the windows was set to 0.546 cm based on impedance matching.

3.7 Microwave Diagnostics

The primary diagnostic tool for our gyrokystron experiments is the anechoic chamber. A cross-sectional view of the chamber can be seen in Fig. 8. This is a metal chamber, whose inner walls are lined with microwave absorbing material (with the exception of the wall that contains the port through which the microwaves enter the chamber). This material is configured in pyramidal surfaces so as to reduce reflections.

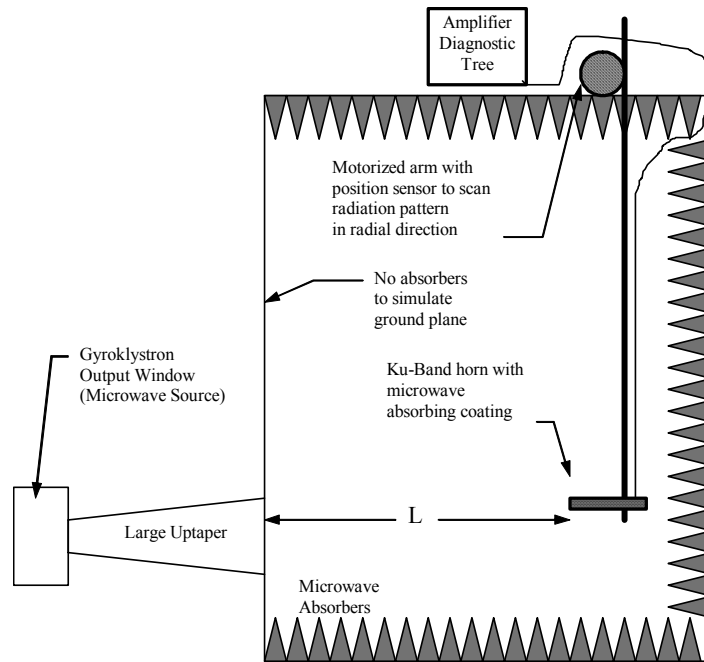


Figure 8 – Cross-sectional view of anechoic chamber.

This chamber was designed to simulate the free space launch of the microwaves coming from the gyrokystron. The microwave pattern is then sampled with a pickup horn which collects a fraction of the power launched. The Horn is made of a microwave absorbing epoxy, cast around a standard open-ended WR62 waveguide which has a cutoff frequency of 9.5GHz. The horn is supported by a dielectric rod, and can be moved by a remotely controlled motor. This way, we can make careful measurements of the power as well as scan the radial pattern of the microwave radiation.

The diagram in Fig. 9 displays the entire anechoic chamber signal transmission line.

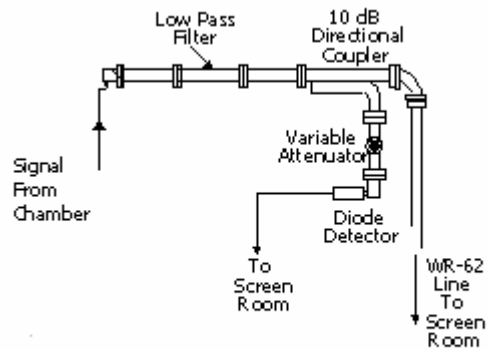


Figure 9 – Diagram of signal transmission line from anechoic chamber.

The microwave signal picked up by the horn then passes through a 20 dB cross-guide coupler. The signal is carried out of the chamber in a coaxial cable and, and is then injected back into a waveguide by a coaxial adapter. The pulse then passes through a low pass filter that significantly attenuates frequencies above 18 GHz.

A 10 dB directional coupler allows the signal to be split into two components: an unattenuated signal, and a (sampled) attenuated component. The attenuated signal passes through a variable attenuator and is fed to a diode crystal detector, which allows us to determine the total power originally present in the anechoic chamber. Meanwhile, the unattenuated signal is led to the screen room through a WR62 waveguide. The signal is split evenly into two lines by a 3 dB attenuator, and these lines can be used for various purposes: for power measurements with the peak power analyzer; for spectral studies with the spectrum analyzer; or for phase coherence studies using a mixer circuit.

The diode detector used for measurements of the chamber power was the HP33330. These measurements are based on the fact that when the crystal is exposed to

an electromagnetic wave it produces a DC signal whose intensity is related to the power of the incident wave. Hence a careful calibration of these crystals is necessary. This calibration was performed with the assistance of a precise low-power microwave oscillator and the peak power analyzer. Then the data was fitted to a quadratic function. The obtained data and fit can be seen in Fig.10.

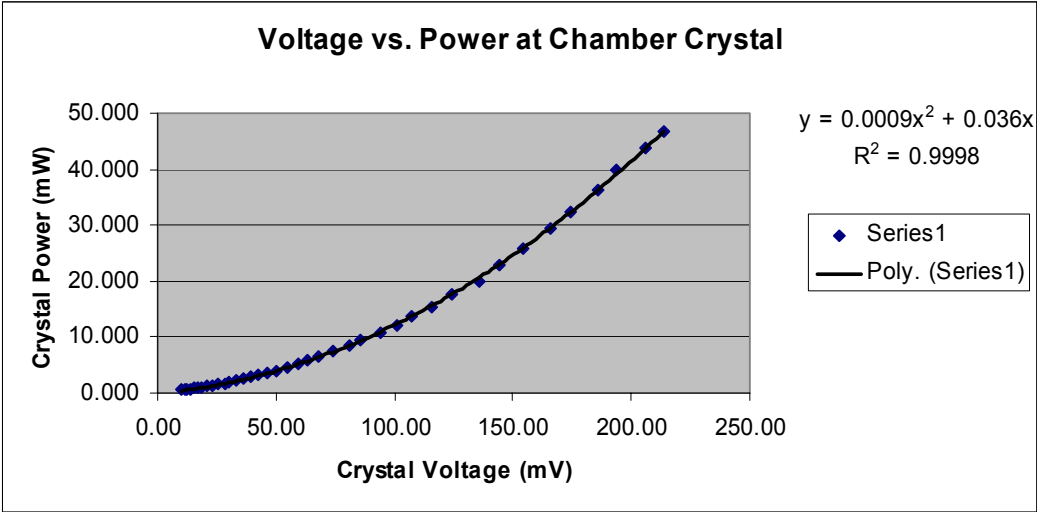


Figure 10 – Plot of crystal power as a function of crystal voltage.

Two other instruments are of note here: the peak power analyzer and the spectrum analyzer. The peak power analyzer provides us another diagnostic of power produced in the gyroklystron. Our analyzer was the model HP 8991A, which is a self-calibrating instrument, correcting for temperature as well as zero drift errors. The spectrum analyzer displays the frequency components of the power produced in the gyroklystron. The specific device used was the HP 84710.

The final component of the diagnostics is the phase coherence mixer circuit. The circuit consists of a double-balanced harmonic mixer with a frequency doubler LO input. This circuit selectively discriminates intermediate frequencies corresponding to

$$\omega_i = 2 \cdot \omega_{LO} - \omega_{RF} \quad (3.1)$$

The LO input is connected to a sample of the magnetron power (driver signal for the gyrokystron), while a sample of the output signal of the gyrokystron is connected to the RF input of the mixer. Thus, the output of the mixer will display any phase coherence between the input and output signals of the gyrokystron. If the signals are uncorrelated a random noise pattern will emerge from the output of the mixer. This method allows us to confirm that the gyrokystron is indeed operating as an amplifier at any given point.

Chapter 4 – Design and Implementation of the Four Cavity Frequency-Doubling Gyroklystron

4.1 Overview of the Four-Cavity Circuit Design

The four-cavity gyroklystron is a frequency-doubling circuit, which possesses one input cavity operating at the drive frequency in the TE_{011} mode and three other cavities operating at the second harmonic of the drive frequency in the TE_{021} mode. An engineering design of the tube is presented in Fig. 11. The design of this four-cavity gyroklystron was based on the preexisting design of a three-cavity tube (SH2) which was performed by I. Yovchev [53]. That tube was then implemented and studied experimentally by M. Castle.

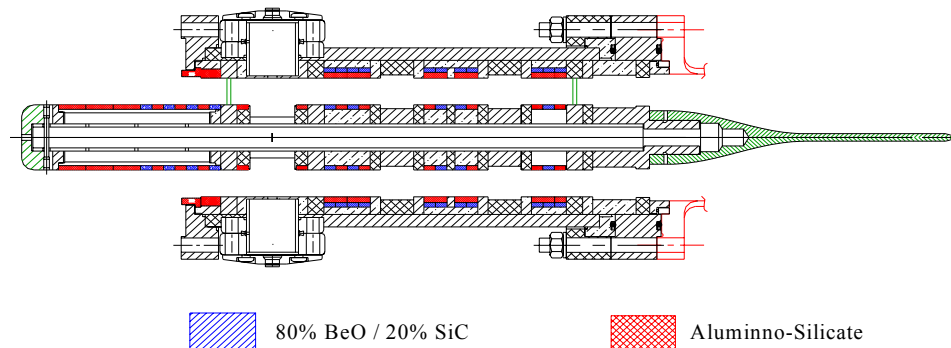


Figure 11 – Engineering diagram of four-cavity circuit .

The original concept behind the four-cavity design was to produce a tube with elevated gain by introducing one more cavity, to be located between the input and buncher cavities of the older three-cavity design. I took as given three cavities with specific frequencies and Q factors. I used the simulation code COAX (discussed in Chapter 2) to design a new intermediate cavity by attempting different geometric configurations based on the predicted cold-test resonant frequency of the TE₀₂ mode (output of COAX). Then I used the simulation code MAGYKL (also discussed in detail in Chapter 2) to simulate various configurations of the four (three old and one new) cavities, based on the predicted efficiency of the overall circuit at different levels of input power. Thus I performed a comprehensive search in a six-dimension parameter space consisting of three drift space distances, frequency and Q-factor of the new cavity, and input drive power. The design was based on a value of $\alpha = 1.4$ and a drive frequency of 8.568 GHz. The final optimal design I obtained from my simulations is presented in Table 6. Next, I will talk about each cavity in detail.

Cavity	Resonant Frequency (GHz)	Q-factor	Operating Mode
Input Cavity	8.568	54	TE ₀₁₁
Buncher Cavity	17.130	410	TE ₀₂₁
Penultimate Cavity	17.136	390	TE ₀₂₁
Output Cavity	17.115	310	TE ₀₂₁

Table 6 - Theoretical design of the four-cavity circuit.

4.2 The Input Cavity

The input cavity was initially designed and cold tested by K. Flaherty [54]. It is a coaxial cavity designed to operate at the TE₀₁₁ mode, with a design frequency of 8.568 GHz and a design Q of 50. A cross sectional view of this cavity can be seen in Fig. 12. It should be noticed that the cavity's outer radius is the same as the drift region, and that it is the inner radius that creates the cavity.

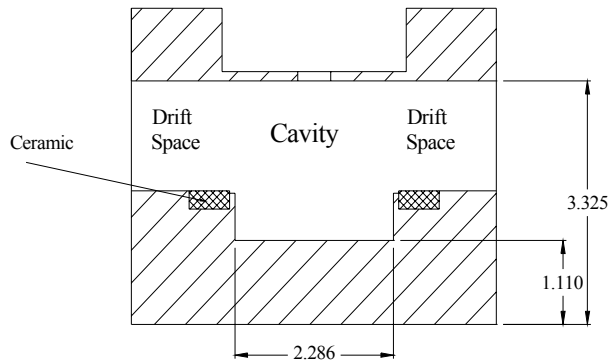


Figure 12 – Cross-sectional view of input cavity (all dimensions in cm) .

The input power is injected into the input cavity by means of an elliptical coupling slot (1.905 cm wide by 0.47 cm wide with corners of a 0.318 cm (0.125”) radius). The total Q factor of a cavity (Q_T) is determined by its diffractive (Q_D) and resistive (or lossy) (Q_R) components, as

$$\frac{1}{Q_T} = \frac{1}{Q_D} + \frac{1}{Q_R} \quad (4.1)$$

For optimal coupling, the cavity was designed so that its diffractive and resistive Q factors were equal. The diffractive Q is determined by the geometry of the cavity and the coupling aperture, while the resistive Q was set by adjusting the location of two lossy ceramics near the edges of the inner radius of the cavity.

The final cold test resonant frequency for the cavity was found to be $8.585 \pm .001$ GHz and its final Q of 54 ± 5 [40]. The plots of the cold-test reflection (blue diamonds) and transmission (pink squares) coefficients are shown in Fig 13. The stability of this cavity was also studied using the code QPB, and the resulting data is presented in Fig. 14. Each one of the curves in Fig. 14 represents the threshold current for start of oscillation of a given mode as a function of the magnetic field in the cavity. So, for a given value of the magnetic field, the cavity will be stable for a certain mode as long as the beam current is below the curve of the start of oscillation current for that mode. Therefore this study indicated that the cavity would be stable for all magnetic fields for currents up to 560 A.

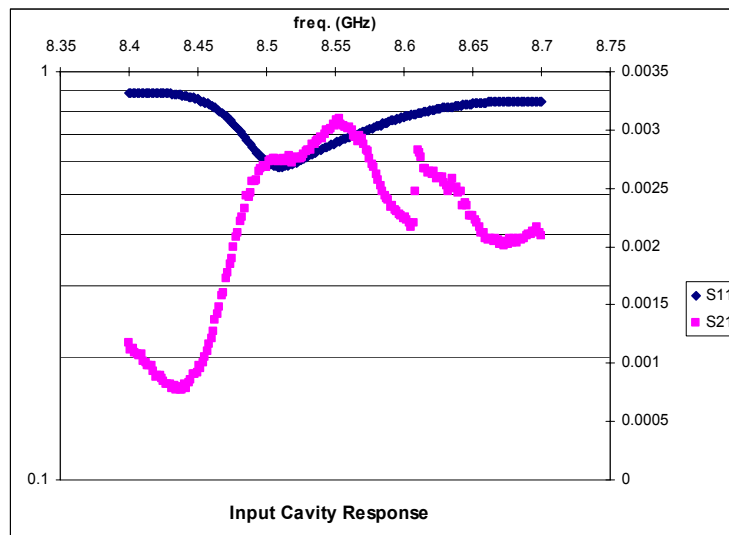


Figure 13 – Cold-test transmission and reflection coefficients.

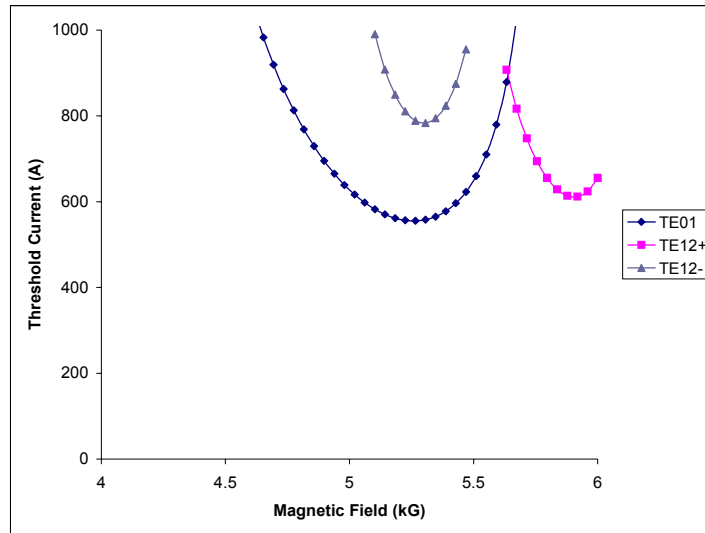


Figure 14 – Start of oscillation curves for input cavity.

4.3 Buncher and Penultimate Cavities

If one examines Table 6 it will be noticeable that the characteristics of the buncher and penultimate cavities are very similar. There are only small variations in their frequency of operation $\Delta f_R \sim 6$ MHz and Q-factors $\Delta Q \sim 20$. If we were to manufacture both of these cavities and then cold-test them, we would observe that the experimental errors in measurement of f_R and the Q-factors for the cavities would indeed be greater than the design differences between these two cavities. Therefore we decided to make the buncher cavity identical to the penultimate cavity. Figure 15 presents a cross-sectional view of the cavity. This cavity was originally designed using COAX. The stability of the cavity was studied using QPB. The results of QPB are displayed in Fig. 16. This graph indicates that the cavity would be stable for a beam current of 540 A with a magnetic field in the cavity up to 5.4 kG.

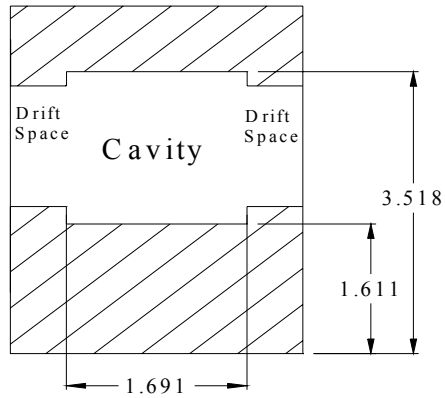


Figure 15 – Cross-sectional view of buncher cavity (all dimensions in cm).

The cavity was cold-tested, and its resonant frequency and Q-factor were adjusted by varying the dimensions of the cavity and the proximity of the drift space ceramics [40]. The final resonant frequency was 17.136 GHz with a Q-factor of 390.

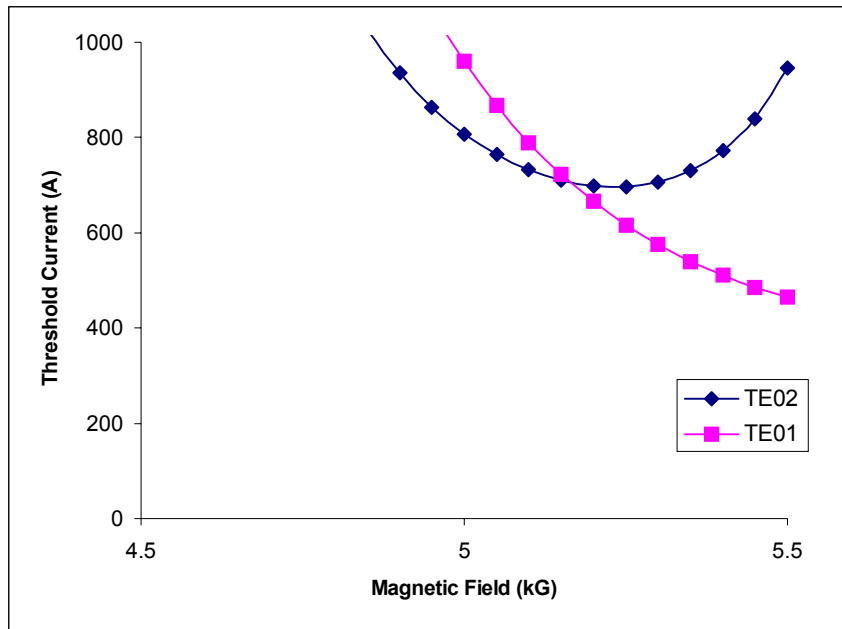


Figure 16 – Start of oscillation curves for buncher cavity

4.4 Output Cavity

A diagram of this cavity is in Fig. 17. This cavity was initially designed using a time-dependent version of the code GYCOAX (the predecessor of MAGYKL). The simulations predicted that efficiency could be optimized by detuning the resonant frequency of the cavity to 17.11 GHz. This design was later altered based on data from cold-testing of the cavity. One aspect of the cavity is of particular importance. The downstream edge of the cavity (referred to as "lip") sets the diffractive Q of the cavity, and is designed so as to maximize the amount of microwave power that exits this edge of the output cavity in the TE_{021} mode. The steps on the inner and outer coaxial regions of the lip are equal so as to minimize conversion of the TE_{021} mode into the TE_{011} mode near 17 GHz. The final measured values of the resonant frequency and Q-factor for this cavity were 17.115 ± 0.001 GHz and 310 ± 8 [40].

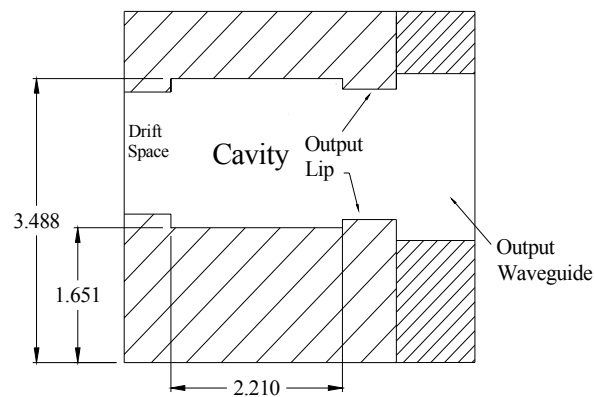


Figure 17 – Cross-sectional view of output cavity (all dimensions in cm).

4.5 Drift Spaces

Drift spaces are regions that are designed to be void of electromagnetic fields, and which isolate the various cavities of the circuit. The dimensions of these regions were determined so as to allow enough clearance for the electron beam, while being cutoff for as many modes as possible. Given that the guiding center radius for the beam is approximately 2.56 cm, and the Larmor radius is 0.3-0.5 cm, the minimum outer radius and maximum inner radius would be 3.06 cm and 2.06 cm, respectively.

The final chosen outer and inner radii were 3.325 cm and 1.825 cm, respectively, so as to allow for extra clearance from the beam. For this geometry, there are several modes below the drive frequency which are not cutoff. These are shown in Table. 7.

Mode	Cutoff Frequency (GHz)
TE ₁₁	1.8765
TE ₂₁	3.730
TE ₃₁	5.542
TE ₄₁	7.2975

Table 7 – Modes that are not cutoff in the drift.

In order to eliminate these modes, the drift regions are lined with special microwave-absorbing ceramics. These were of two types: the CIAS (carbon impregnated alumino-silicate) were custom made in-house, and the Beo/SiC which were commercially available from Ceralloy [31].

The specifications of these ceramics can be found in Table 8.

	CIAS	BeO-SiC
Real Part of Dielectric Constant	5.3	16-17
Loss Tangent	.17	.21

Table 8 - Dielectric properties of microwave-absorbing ceramics.

4.6 Small Uptaper and Coaxial to Circular Transition

The microwaves that exit the output cavity in the TE_{02} coaxial mode travel downstream and must undergo a conversion from coaxial to circular geometry. This conversion is achieved by the presence of an inner and an outer taper. It is important that these tapers be very carefully designed so as to maximize the transmission of power downstream, while minimizing any mode conversion that may occur. The previous uptaper design, used in the three-cavity system, caused mode conversions of about 5% from the TE_{021} mode. Thus, I designed a new set of dual tapers to optimize the power extraction from my four-cavity tube.

In order to do so I utilized the computer codes PROFILE and CXTAPER. CXTAPER is an upgraded version of the code NLTAPER. This code was created by W. Lawson [55] and was upgraded for simulating coaxial tapers. The code is based on a numerical solution of the generalized Telegraphist's equations. The tapers were designed by trial-and-error alteration of certain geometric parameters.

The final taper designs can be seen in Fig.18. The inner transition has a smooth sectioned profile defined by a cosine function and linear segments, while the outer taper is also sectioned with a linear segment following a Dolph-Chebyshev profile.

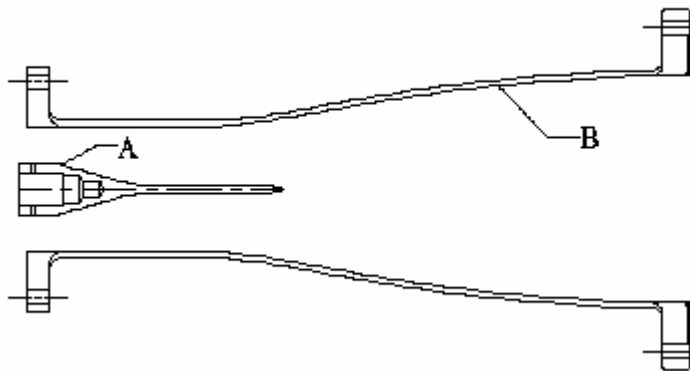


Figure 18 – New dual tapers: A - Inner Transition, B – Outer Taper

This taper constitutes a significant improvement over previous designs, reducing the mode conversion of the TE_{021} mode to less than 0.2%. The design has a theoretical normalized transmitted power of 98.9%, with an isolation of at least -30dB from unwanted modes.

4.7 Performance of Theoretical design of Four-cavity Gyroklystron

As mentioned earlier, I studied the characteristics of the theoretical design for the four-cavity circuit with MAGYKL. Figure 19 displays the efficiency of the design as a function of input power. For $\alpha = 1.4$ this design had a peak efficiency of 34.9 %, corresponding to an output power of 86.7 MW, with an input drive power of 250 W. The gain at that point is 55.4 dB. For input power levels between 140 and 340 W, the efficiency of the tube remains above 30 % leading to output powers above 74 MW.

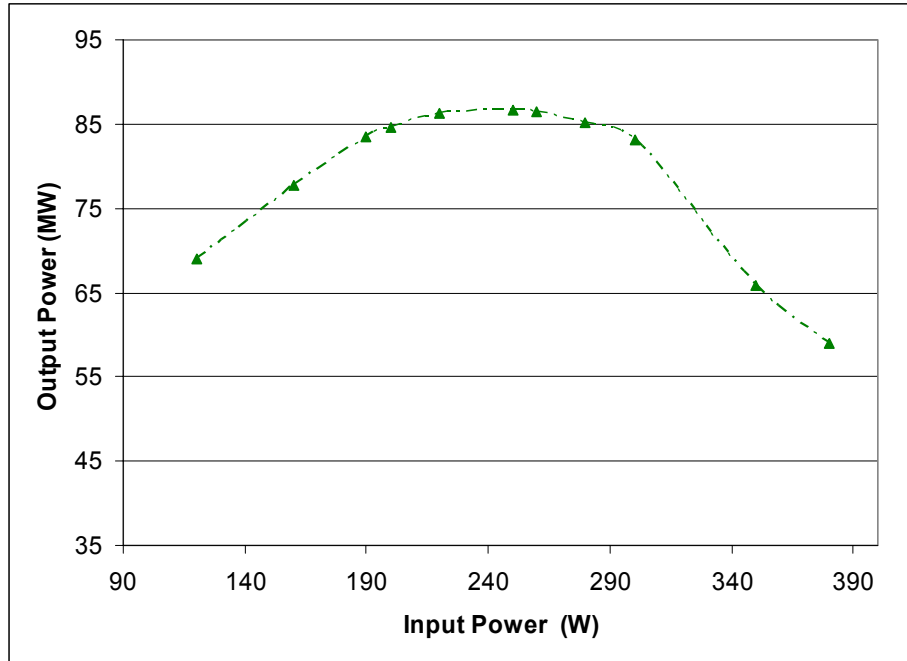


Figure 19 – Output power as function of input power.

The drive curve for this design can be seen in Fig. 20, where I plot efficiency vs. drive frequency for an input power of 190 W. The predicted bandwidth of the frequency-doubling circuit from computer simulations is 6 MHz.

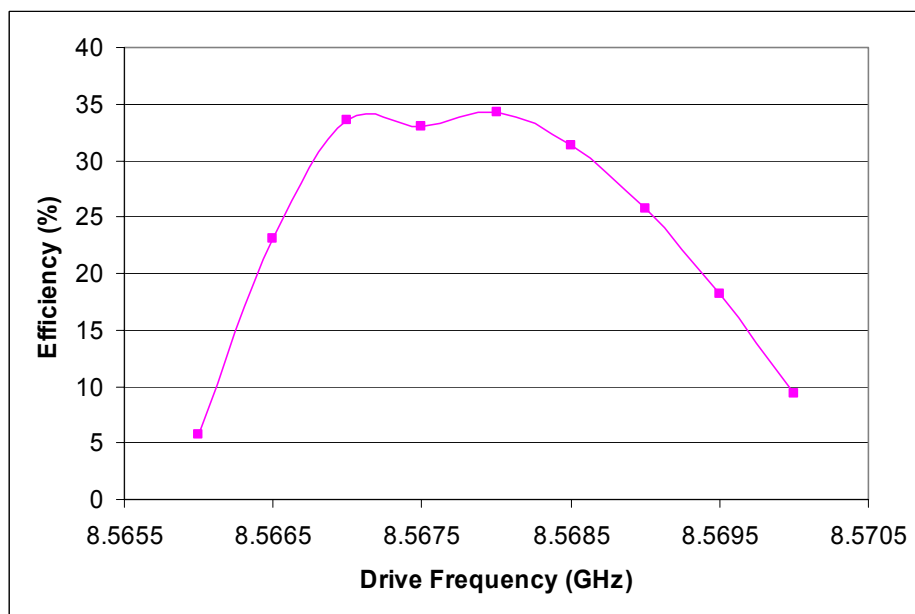


Figure 20 – Efficiency as a function of drive frequency.

This circuit is very sensitive to the velocity ratio as is clear from Fig. 21 which shows the effect of alpha on the efficiency of the design as a function of input power. One can notice that the curves for higher values of α are narrower, have higher peaks and these occur at lower values of the drive power. As the value of α decreases the maximum efficiency attainable by the circuit is reduced, while the amount of input power needed for optimal performance increases significantly. This phenomenon is clearly illustrated in Fig. 22 which shows the variation of the maximum efficiencies and gains for the circuit as a function of α . Both the efficiency and the gain (dB) of the gyrokystron decrease steadily with alpha.

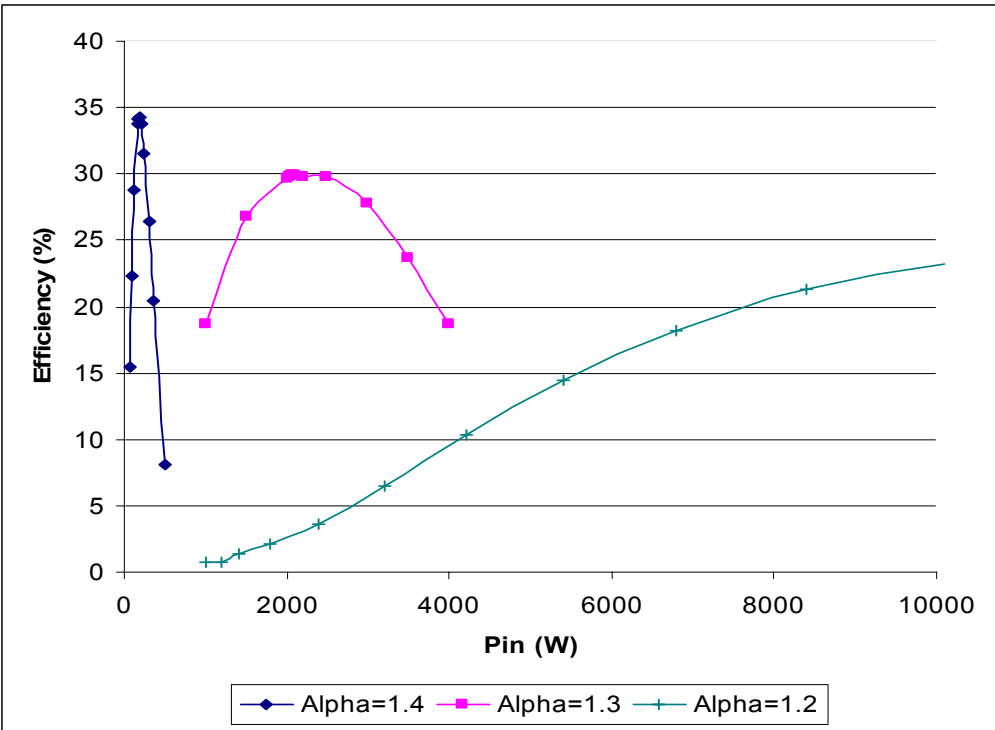


Figure 21 – Effect of alpha on efficiency as function of input power.

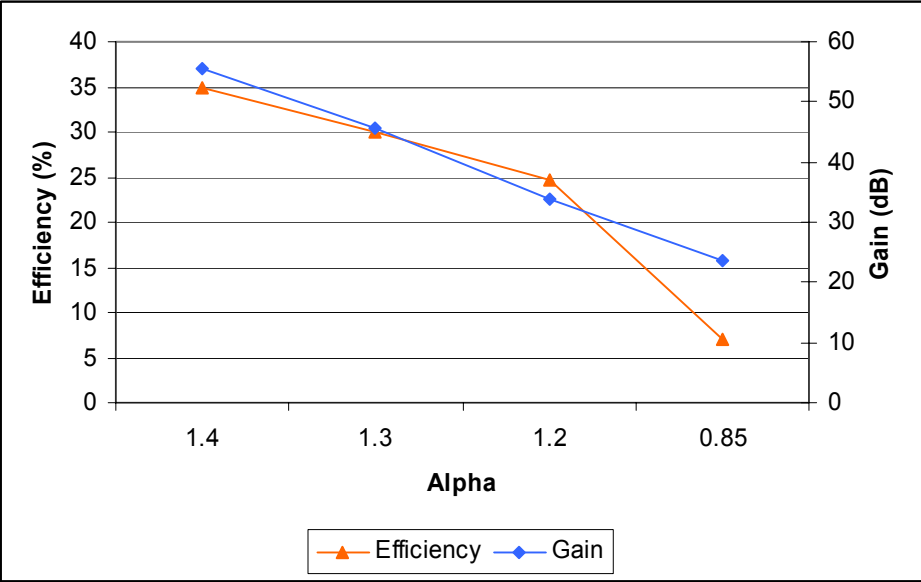


Figure 22 – Effect of alpha on efficiency and gain.

Chapter 5 – Experimental Results

5.1 Overview of Experimental Procedure

Every time our electron gun remains dormant for a few months, it requires re-conditioning. This process is two-fold: the first part involves a gradual heating of the gun emitter, without any potential across the gun electrodes. This procedure eventually reduces the amount of gas generated by the gun at the operating temperature. The second part of this re-conditioning is called the re-activation of the gun. It entails firing the electron beam into the anode of the gun, drawing progressively higher and higher currents. Figure 23 displays a diagram of data collected during our last re-activation.

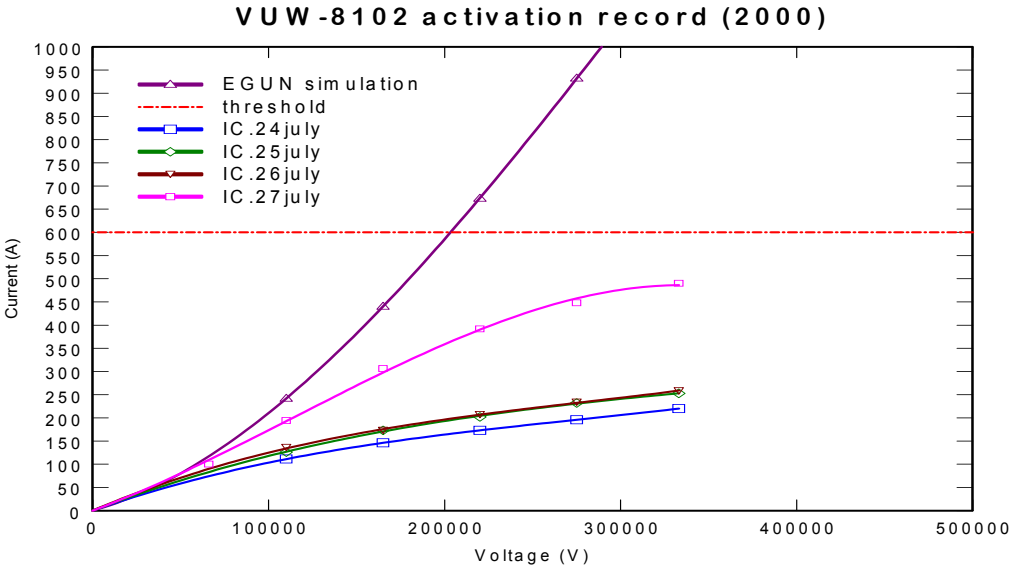


Figure 23 – Reactivation of electron gun.

Once the emitter has been appropriately conditioned and is operating within desired parameters, then the search for amplification can begin. The experimental search is conducted by systematically varying all the parameters at our disposal and observing the characteristics of the microwaves produced at the output of the gyrokystron. The parameters that we can control are of three fundamental types: beam parameters, input power parameters and magnetic field parameters.

The primary beam parameter we manipulate is the beam voltage (V_b). This is the voltage applied across the electrodes of our single cathode MIG. We can also indirectly affect the beam current (I_b). This is possible because the beam current is determined both by the beam voltage and by the temperature of the emitter (as long as one is operating below the space-charge regime). Thus by altering the heating element power of the emitter we can vary the beam current for a constant value of beam voltage.

The situation is complicated by the fact that the voltage and current pulses vary significantly from pulse to pulse even when all parameters we can control remain the same. Furthermore, these pulses possess a significant amount of ripple. Typical pulses for V_b , and I_b can be seen on Fig.24. One can notice a significant slope and noise on the tops of both pulses.

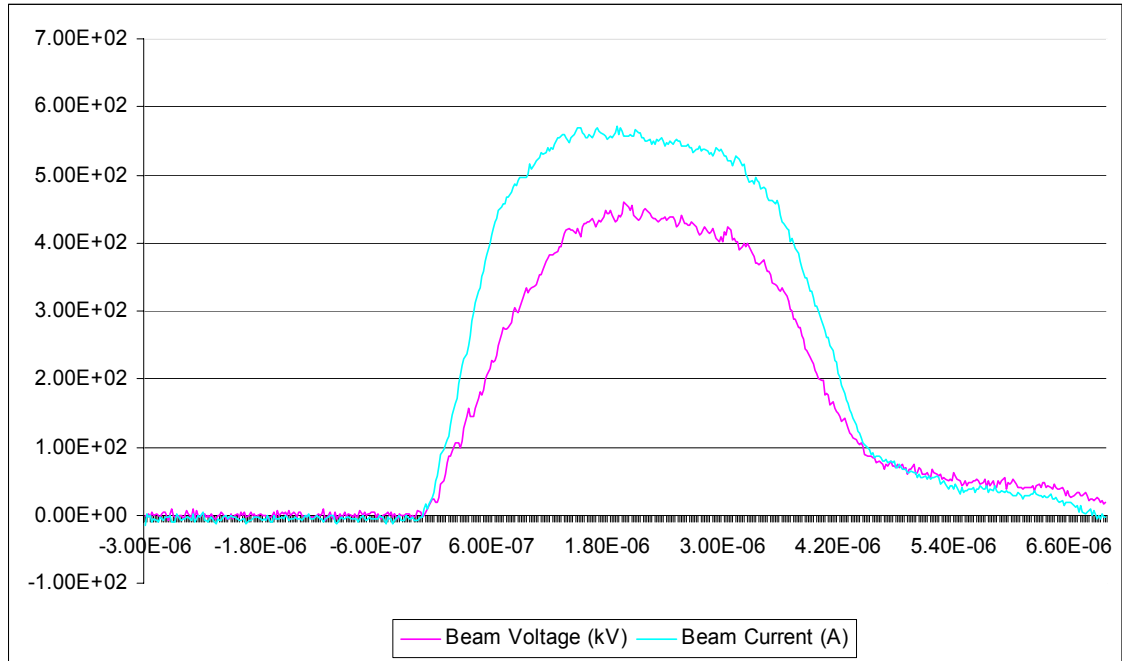


Figure 24 – Typical pulses of beam voltage and current.

The input power variables at our disposal are the frequency and total power of our driver, in this case a magnetron. The total frequency range possible for the magnetron is approximately 20MHz, which is mechanically tunable with a tuning screw. The maximum output power of the magnetron is 150 kW.

With respect to the magnetic field, we can adjust the values of four currents which power eight electromagnets: the current of the gun coil (I_G); the current (I_K) of a set of two coils located at the beginning of the microwave circuit; the current (I_L) of a set of three coils located over the microwave circuit; and the current (I_M) of the last two coils at the end of the microwave tube, prior to the beam dump. The control of these magnet currents is of critical importance, for this is how we set (1) the value of velocity pitch ratio (α) at the entrance of the gyrokystron, as well as (2) the cyclotron frequency

within each cavity (very important to maximize the coupling of beam to desired electromagnetic mode in each cavity).

Therefore, our experimental search consisted in probing by trial-and-error a nine-dimensional parameter space seeking to find a region of optimal performance. This task was quite overwhelming at first, however over time we gradually identified distinct regions of performance of the gyrokystron. Eventually an area of optimal performance was identified.

This task is time consuming. Even though the modulator was designed to operate at 5 Hz, in actuality we operated the system at a repetition rate of less than 1 Hz in order to avoid mis-fires caused by the poor response of the spark-gap (the most sensitive element of our firing circuit). However, the main restrictions are imposed by out gassing of the gun during each firing session. This phenomenon gradually degrades the vacuum as more shots are fired from the electron gun, effectively limiting the overall operation of the system to a few hundred shots at a time. Further conditioning of the gun, over several sessions, improves its out gassing behavior.

5.2 Presentation of experimental results

We identified a region of optimal performance of the gyrokystron. This region was defined by a beam voltage and current of 450 ± 10 kV and 550 ± 20 A, respectively. The values of the magnets' currents are: $I_G = 200 \pm 1$ A, $I_K = 255 \pm 1$ A, $I_L = 378 \pm 1$ A and $I_M = 320 \pm 1$ A. As expected, the performance of the circuit was extremely sensitive to the exact value of the magnets' currents. A variation of any of the

currents beyond 2 A (less than 1%) would throw us out of the amplification regime. The magnetic field profile generated by these currents is illustrated in Fig.25.

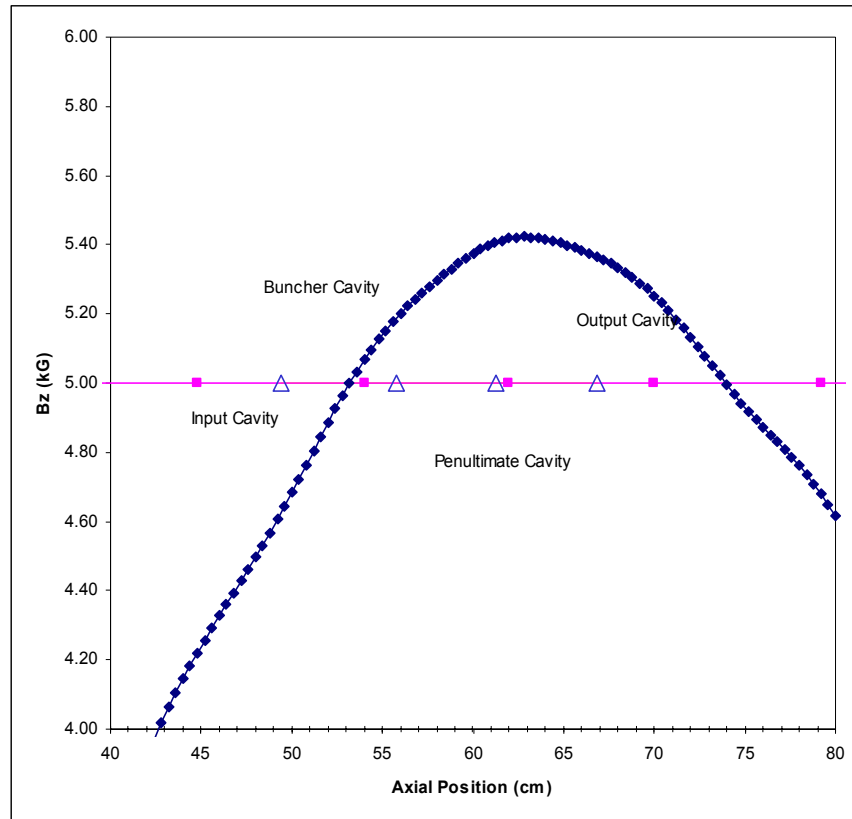


Figure 25 – Experimental magnetic field profile.

The highest peak power observed was 18.5 ± 1.7 MW measured with the anechoic chamber's diode detector. The signal from the detector for this pulse can be seen in Fig.26. The power of this pulse was also measured with the peak power analyzer, yielding 18.1 ± 1.7 MW. The corresponding efficiency based on both the crystal and peak power analyzer measurements is 7.0%.

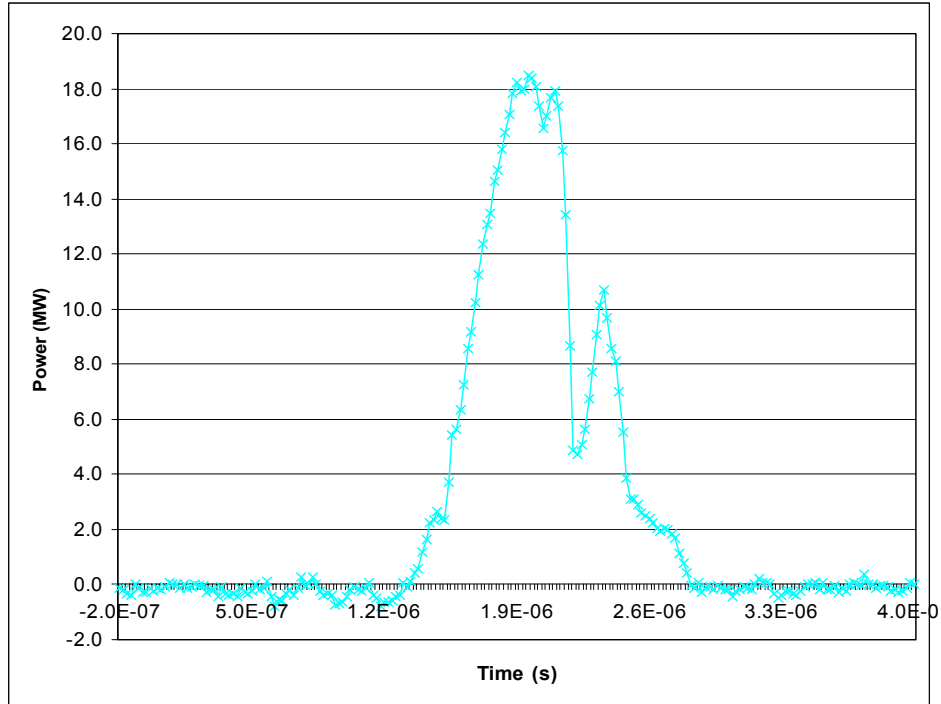


Figure 26 – Output pulse with highest peak power observed .

The forward and reverse pulses in the input line are presented in Fig. 27. The net power used to drive the gyrokystron at this point was approximately 73.3 ± 6.6 kW. This corresponds to a gain of 24.0 dB, for both the crystal and peak power analyzer values. The FWHM (full width half-maximum) time for this pulse is $0.73 \mu\text{s}$.

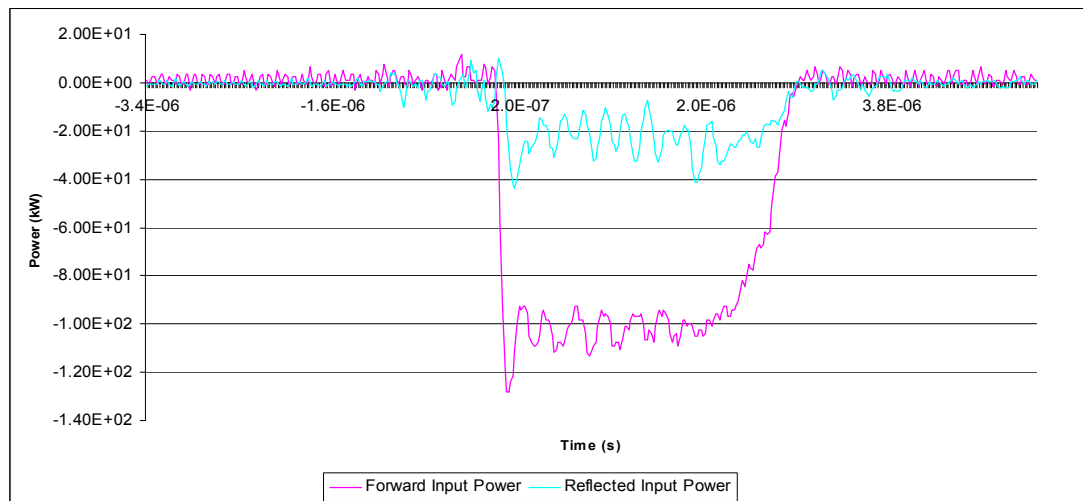


Figure 27 – Forward and reflected input power.

The widest high-power pulse observed is shown in Fig.28. This pulse had a maximum power of 15.4 ± 1.4 MW measured with the chamber crystal. The FWHM time for this pulse is $1.18 \mu\text{s}$. The efficiency and gain of this pulse are 6% and 23 dB, respectively.

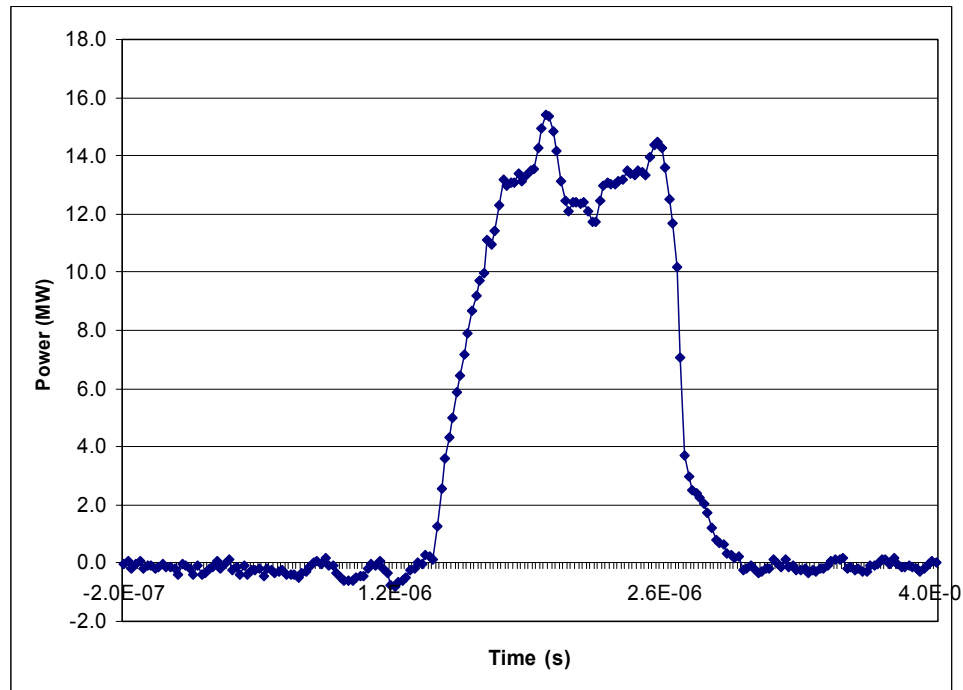


Figure 28 – Widest output pulse observed.

The fact that the output did represent an amplified signal was confirmed by two methods: response of gyrokystron to zero input power, and phase correlation of input and output powers. Indeed, every time that the magnetron driver was turned off we observed no output signal, and once the magnetron was turned back on a distinct gyrokystron output pulse was observed - while all other parameters were maintained constant.

For the phase correlation study we utilized a circuit described in Chapter 3. A typical output pulse and the corresponding signal from the phase correlation circuit are seen in Fig. 29. The correlation signal clearly displays a non-random behavior which is related to the output power pulse, giving a second indication that the gyrokylystron is operating as an amplifier in this regime. The phase correlation circuit was periodically used to confirm that we were still amplifying, and not seeing an oscillation.

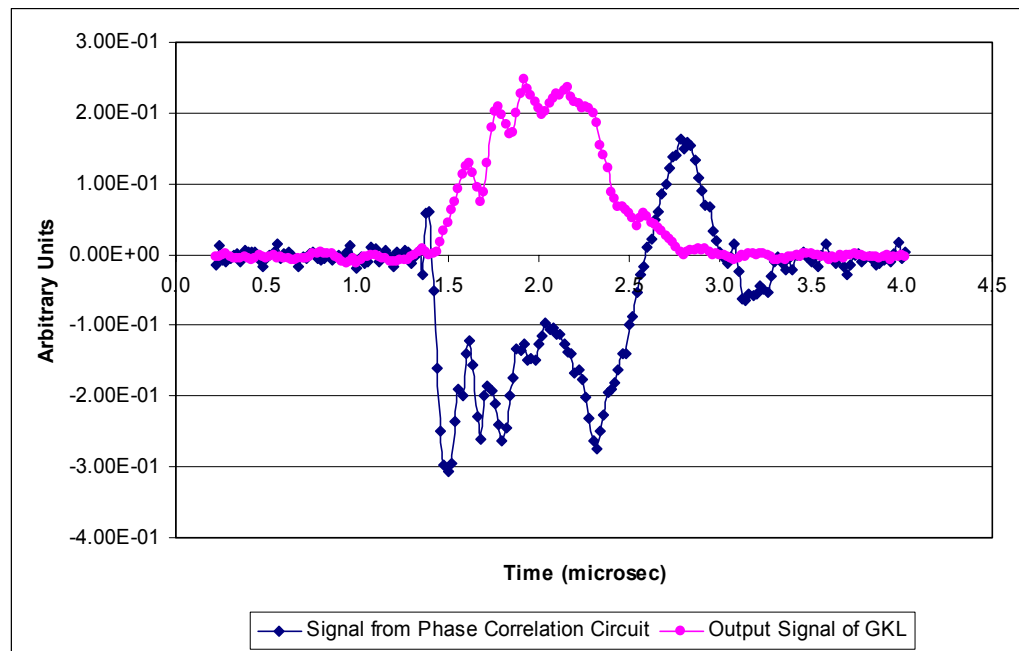


Figure 29 – Phase correlation signal.

We utilized the spectrum analyzer to study the frequency composition of the output signal. The low-repetition rate restriction of our modulation led to severe limitations in the resolution of the frequency scan that could be performed in a reasonable time. A typical spectrum analyzer scan in this regime is displayed in Fig. 30. The output pulses appear to have a frequency range of 32 MHz, with a peak at 17.15 GHz. The spectrum follows the typical frequency spectrum of the magnetron pulse.

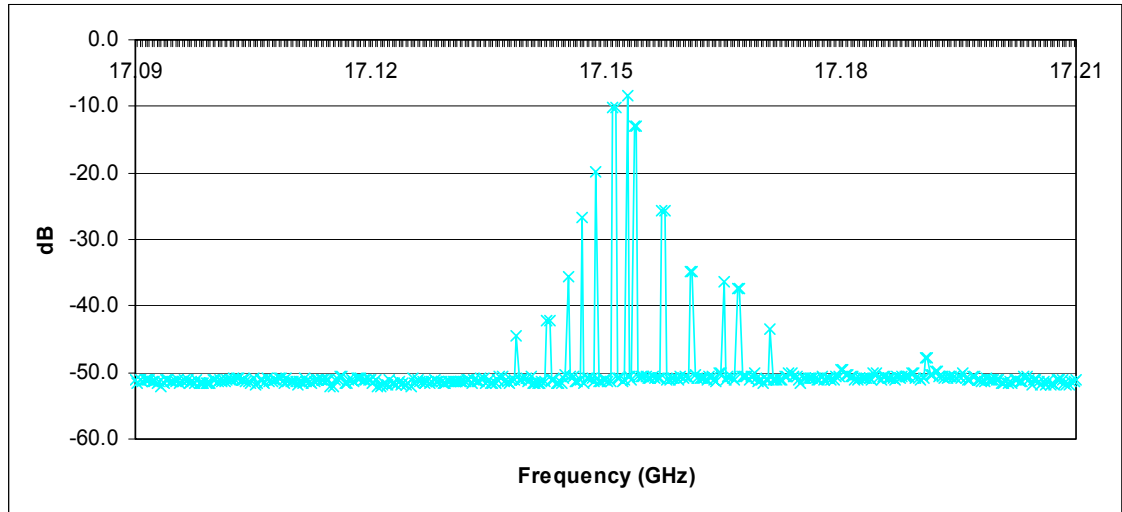


Figure 30 – Spectrum of output power.

Next we performed a far-field scan of the output mode. In order to perform this scan we moved the pickup horn in the anechoic chamber along the vertical axis, by remote control. For each location of the horn we collected several measurements of the output power. The whole procedure took approximately an hour. The pattern resulting from the average of power pulses observed in each location is displayed in Fig. 31. The data collected is in good agreement with the theoretical radial pattern of the TE_{021} mode, which is included in the plot.

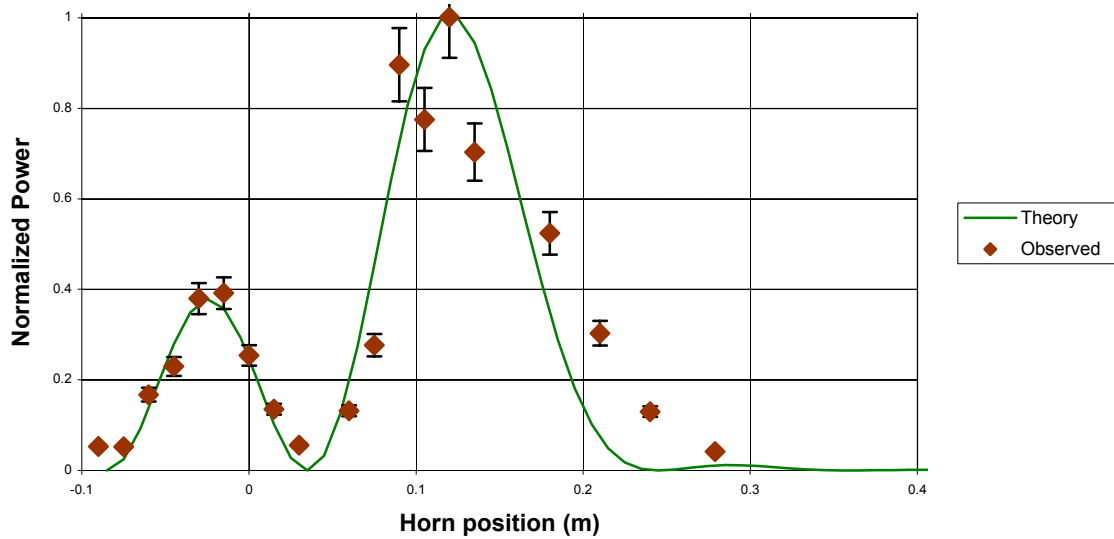


Figure 31 – Far-field pattern of output and theoretical curve for TE₀₂.

For most of our experimental studies, the pickup horn was positioned with the broadwall of the WR62 waveguide in the vertical direction. This is done in order to sample azimuthal electric fields (E_{θ}) in the anechoic chamber, since E_{θ} is the only component of the electric field that is present in the pure TE₀₂₁ mode. However, we periodically rotated the pickup horn by 90° so as to sample any radial electric fields (E_R) that may be present in the chamber. At each time the pickup was rotated, no power was observed. This test provided further confirmation that the output power was in the TE₀₂₁ mode. We also collected data exhibiting the relationship of the output power to the frequency of the driver. The methodology followed was similar to that used for the far-field scan. We adjusted the frequency of the magnetron mechanically using its tuning screw, then collected measurements of the output power for several pulses. The procedure was repeated for several magnetron frequencies, then we averaged the values

of the power recorded for each frequency. The resulting drive curve is seen in Fig. 32.

The bandwidth of the four-cavity frequency-doubling gyrokylystron is approximately 60 MHz, which is consistent with the Q-factors of the circuit's cavities.

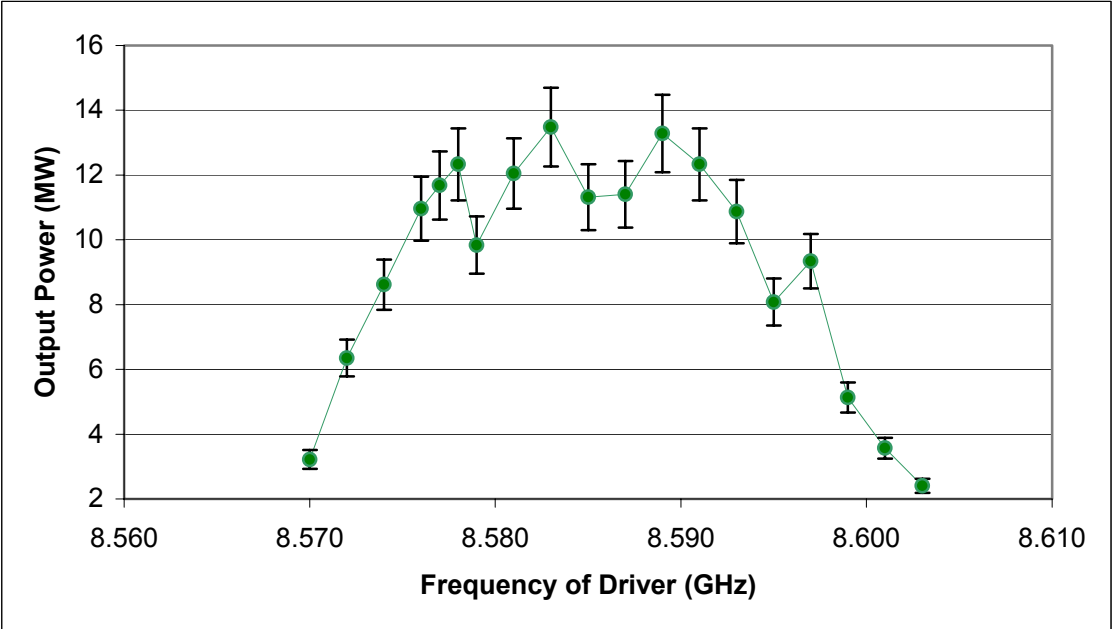


Figure 32 – Experimental drive curve for four-cavity gyrokylystron.

5.3 Preliminary Analysis

The tube has performed significantly worse than predicted in the theoretical design. The original design (presented in Chapter 4) predicted a peak output power of the order of 85 MW corresponding to an efficiency of 34.3 % with a gain of 56.8 dB for an alpha of 1.4 and with an input drive power of 180 W. These values were much higher than the best experimental results obtained.

In order to understand this situation, I simulated the electron beam in our gun using the computer code EGUN. The results from EGUN based on the experimental

values of V_b , I_b and magnet currents indicated that the velocity pitch ratio (α) was equal to 0.721 in our best operating regime. Now, there is some experimental indication that the values of α calculated by EGUN are conservative [56]. The actual value of α is likely to be 15% higher than that predicted by EGUN, due to the axial self-magnetic field of the beam. Thus, the actual value of α present in our best experimental results was at the most 0.85. This is only 60% of the expected value of 1.4 at which this gyrokylystron was designed to operate (note that the energy produced by the gyrokylystron is approximately proportional to this number squared).

This phenomenon can explain well the poor performance of the tube. To confirm this fact, I simulated the behaviour of my tube for a value of α equal to 0.85 using the code MAGYKL (described in Chapter 2). The results from the simulations are plotted in Fig.33. The predicted efficiency of the gyrokylystron for an $\alpha = 0.85$ and an input power of 73.3 kW is approximately 7% agreeing well with the maximum power observed.

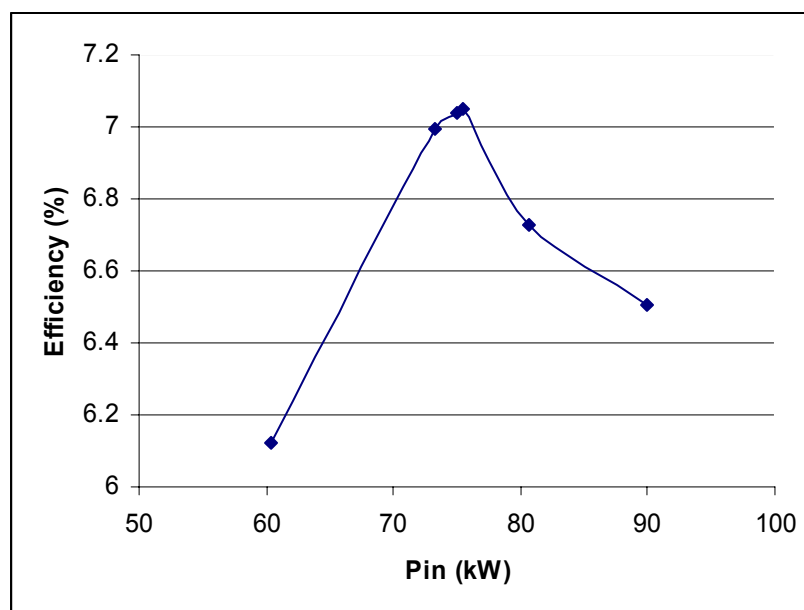


Figure 33 – Theoretical performance of circuit for $\alpha = 0.85$.

Figure 34 displays a comparison of the optimal experimental and theoretical magnetic fields (for $\alpha = 0.85$). It is interesting to note that both theoretical and experimental fields exhibit similar traits: both fields have similar profiles, both have peaks near the center of the penultimate cavity, and both have almost exactly the same value in the center of the input cavity.

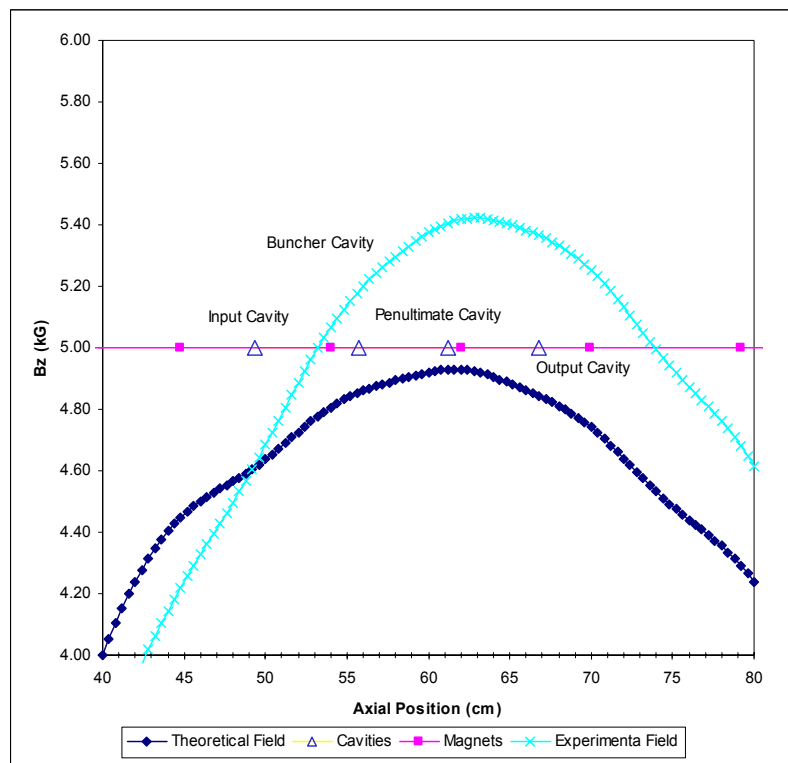


Figure 34 – Comparison of theoretical and experimental magnetic fields.

5.4 Experimental Observation of Instability

Once we were aware of the fact that our limited performance was due to operating in a region of low α , we actively probed for power utilizing magnetic field profiles corresponding to higher values of α . However, we were unable to find any better results. We would start out in a region where amplification was observed with $\alpha < 0.9$ and then gradually vary the magnetic fields so as to raise α . But as soon as the velocity ratio reached 0.9 or above we would cease to observe an output signal from the gyrokystron.

This perplexing behavior became more evident once we observed that anomalous signals were coming from the input line. These appeared to indicate that more power was coming from the input cavity of the gyrokystron than was being produced by the magnetron.

We turned off the magnetron and confirmed that the input cavity was indeed oscillating. This oscillation appeared to be dependent on the value of α , and it became significant when α exceeded 0.9. A typical pulse of this instability in the input cavity is shown in Fig. 35. This instability was observed to produce powers of the order of 150 kW, with pulse widths of $\sim 2.5 \mu\text{s}$.

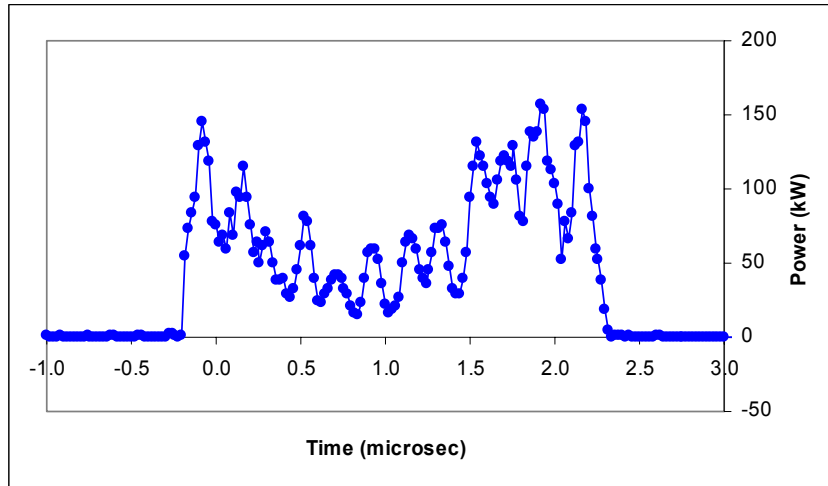


Figure 35 – Instability in input cavity.

In order to better understand the instability, we analyzed its frequency content using the spectrum analyzer. The result of this scan is seen in Fig. 36. The instability appears to have a frequency range of 100 MHz, with a peak around 7.5 GHz.

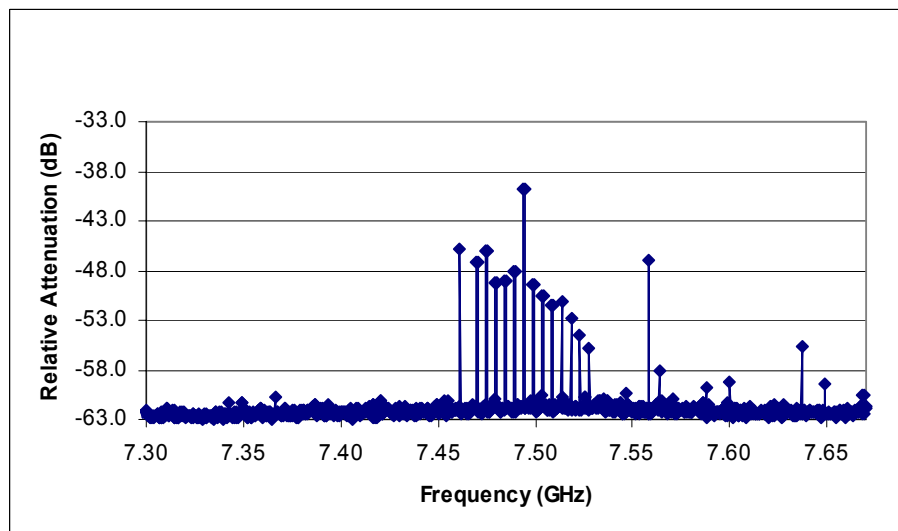


Figure 36 – Spectrum of instability in input cavity.

This instability in the input cavity was then clearly responsible for inhibiting the performance of the amplifier for $\alpha > 0.9$ by disrupting the bunching of the beam by the input signal. The instability thus effectively limited the operation of the gyrokystron to the region of $\alpha < 0.9$ as observed experimentally.

5.5 Analysis of MIG Emitter Performance

We believe that the ultimate cause for these instabilities in the input cavity lies in the emitter of our electron gun. We have observed in the past that the thermionic emitter of our MIG possessed a significant temperature variation. Results from pyrometric studies of the emitter indicated a significant azimuthal variation of the temperature of the emitter, with a range of 46 °C for a nominal temperature of 950 °C. This data, obtained from optical pyrometry, can be seen in Fig. 37. One can notice that the “hot spot” and the “cold spot” of the emitter are 180° apart. A model of the thermal variation across the emitter can be seen in Fig. 38. We believe that this temperature variation is due to non-uniformities in the placement of the emitter’s heating element. In particular, there is a large gap between the power leads of the element which cause that area to be heated less than the rest of the emitter, leading to the occurrence of a “cold spot”.

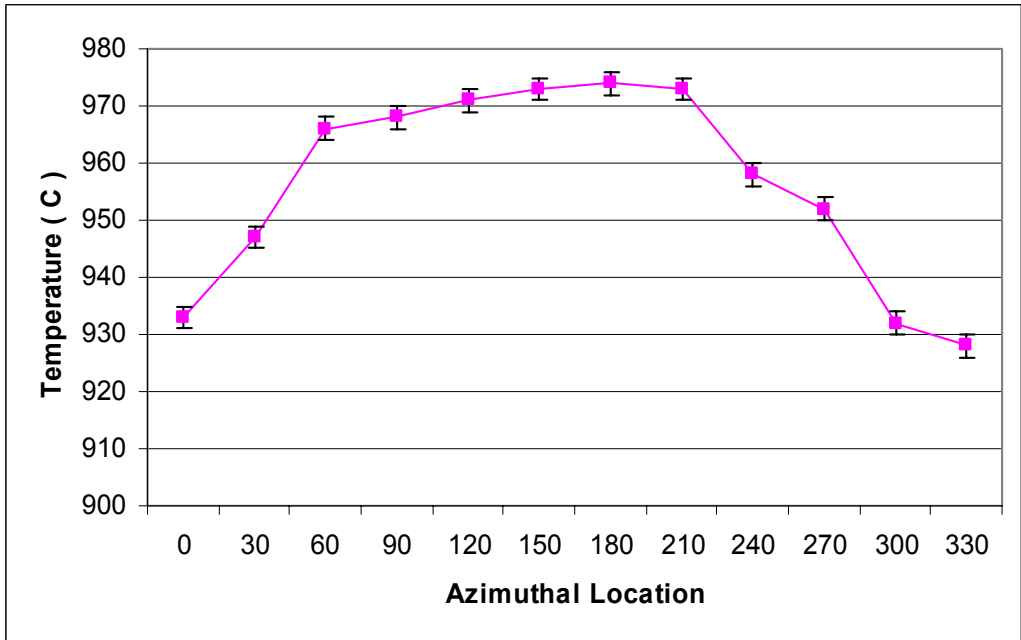


Figure 37 – Variation of surface temperature of emitter.

Since the MIG is operated in the temperature-limited regime, a variation in the temperature of the surface of the emitter would cause a variation in the electron emission across the surface of the emitter. This would then lead to a difference in the current density of the beam produced by the MIG.

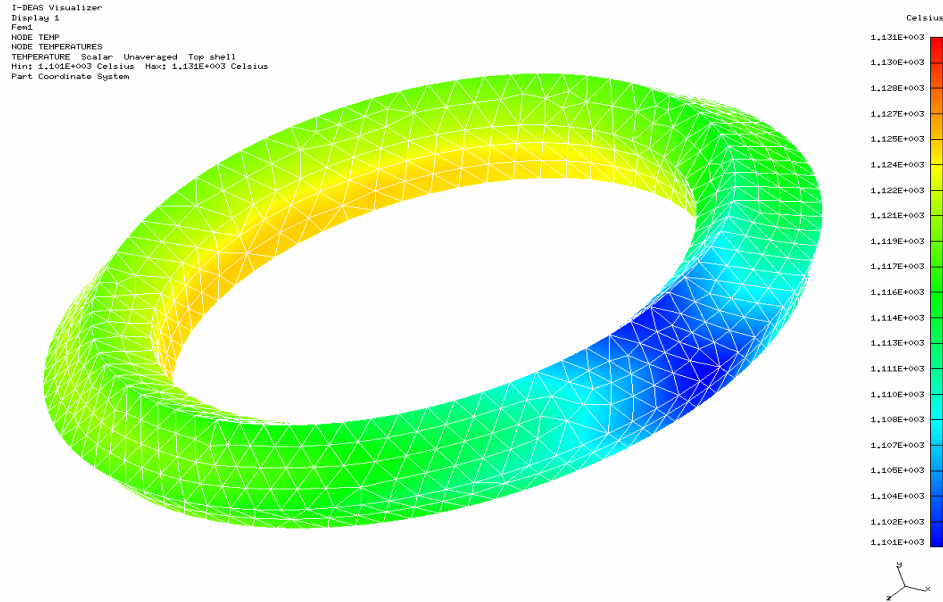


Figure 38 – Thermal profile of emitter.

A series of tests were performed in order to confirm that the temperature variation lead to a significant variation in azimuthal beam density, and to gauge the latter. Broadband radiation badges (10 mrem to 1 krem) were attached to the exterior of the electron gun can, at the axial location of the anode, in equal azimuthal intervals of 30°. Then the gun was fired with no magnetic field so that the beam would land straight into the anode. The results from these tests along with thermal data are presented in Fig. 39. There is a good correspondence between the thermal "cold spot" and the azimuthal location of lower radiation deposition (which is a gauge of the beam current density). From the radiation data, we can surmise that the beam current density may vary as much as 50% across the beam.

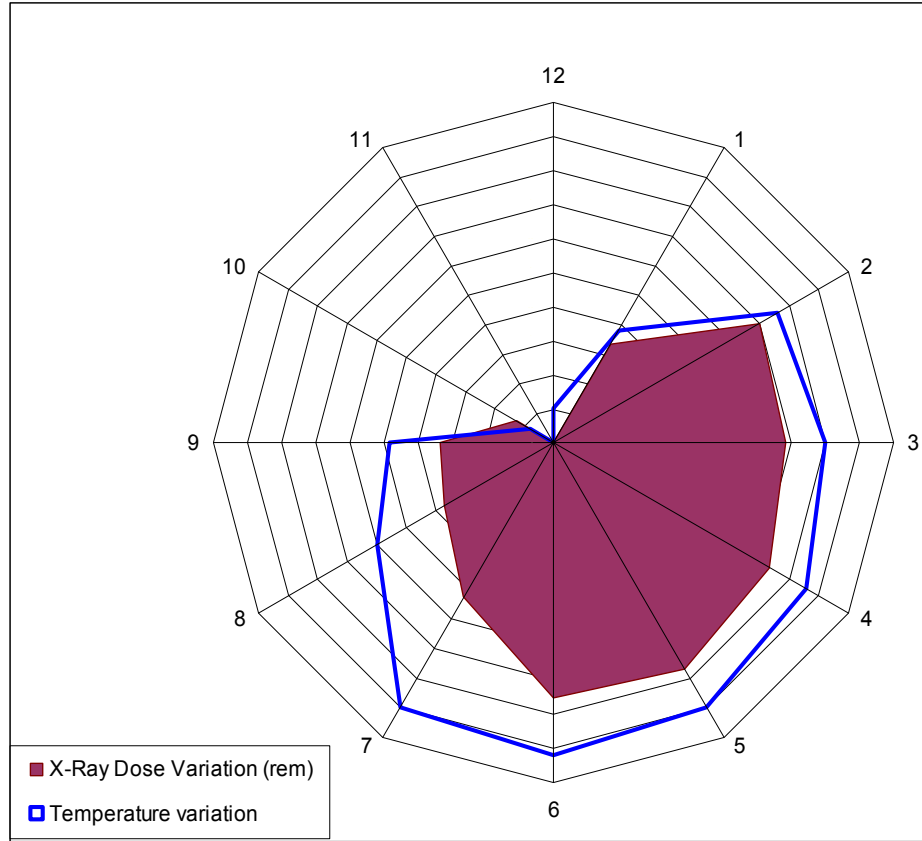


Figure 39 – Comparison of thermal and x-ray data from emitter studies.

We can calculate the current density of thermionic emission by using the Richardson-Dushman equation [57,58] given by

$$J = A_0 T^2 e^{-\frac{e\phi}{kT}} \quad (5.1)$$

where e is the electron charge, ϕ is the work function for electron emission, T is temperature of the emitter. A_0 is a constant given by

$$A_0 = \frac{4\pi me k^2}{h^3} \quad (5.2)$$

where m is the electron mass, k is Boltzmann's constant and h is Planck's constant. A further correction to the Richardson-Dushman equation can be obtained by considering

the effect of the electric field at the emitter surface. The electric field effectively reduces the work function as can be seen in (5.3)

$$\phi = \phi_0 - \Delta\phi \quad (5.3)$$

where the ϕ_0 is the intrinsic work function of the emitting material, and $\Delta\phi$ is the Schottky correction given by

$$\Delta\phi = \left(\frac{eE}{4\pi\epsilon_0} \right)^{1/2} \quad (5.4)$$

where E is the magnitude of the applied electric field at the cathode.

Using these equations we were able to calculate the current density of the beam as a function of azimuthal location. A plot of these values can be seen in Fig. 40. The minimum value of the current density calculated is approximately half of the maximum value. This is in agreement with the data collected from x-ray studies.

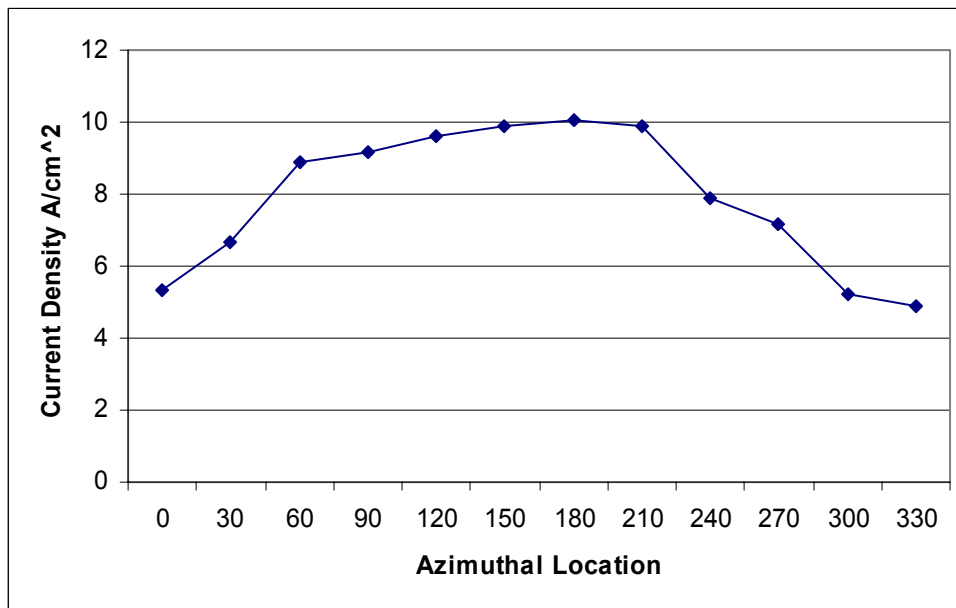


Figure 40 – Current density as function of azimuthal location.

So for the case in which our nominal design current of 540 A is taken to be the average beam current, the effective local values of the current will vary between 336 A and 688 A. These effective local currents correspond respectively to the cold and hot spots of the emitter. We performed EGUN simulations to determine what would be the effect of this current variation in terms of the velocity pitch ratio (α), axial electron velocity and its spread. These beam parameters are most crucial for efficient gyrokystron operation. Figure 41 displays the effect of the temperature variation on α . The variation of the axial velocity spread across the emitter is seen in Fig. 42.

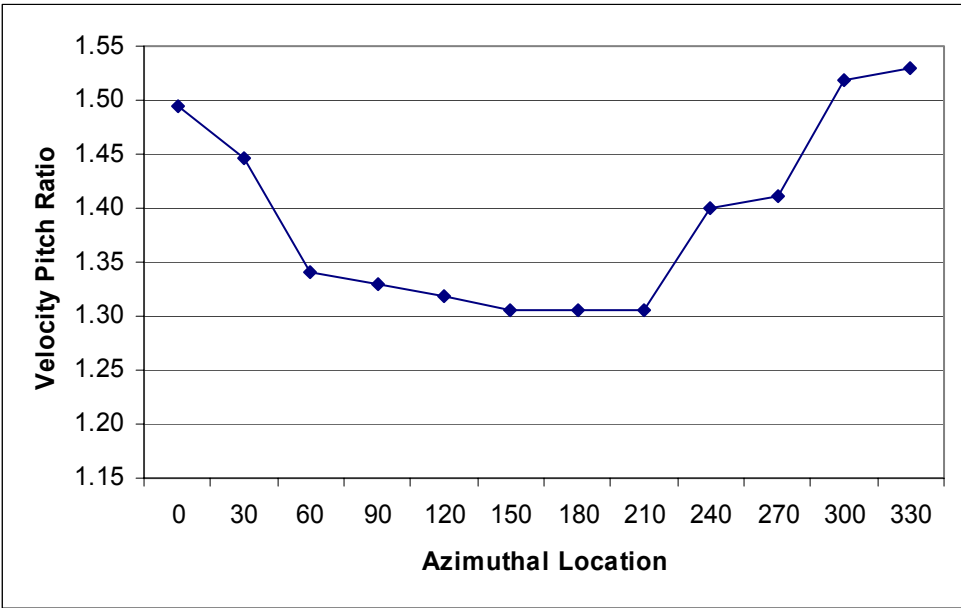


Figure 41 – α as function of azimuthal location (calculated with EGUN).

Now it becomes clear how this phenomenon of temperature variation in our emitter can adversely affect the operation of the gyrokystron. On one hand, it degrades beam quality by creating a distribution of current density across the beam. This distribution will cause beam parameters, which are crucial for gyrokystron

performance (like α), to vary considerably thus decreasing the efficiency and gain of the amplifier. Furthermore, this current density distribution would naturally increase the probability of excitation of spurious modes, since the effective beam current at some locations may be above the start of oscillation current for modes previously deemed unlikely to occur. This latter topic was the primary cause for the lower performance of the four-cavity circuit. I will further discuss and quantify these issues further in the next chapter.

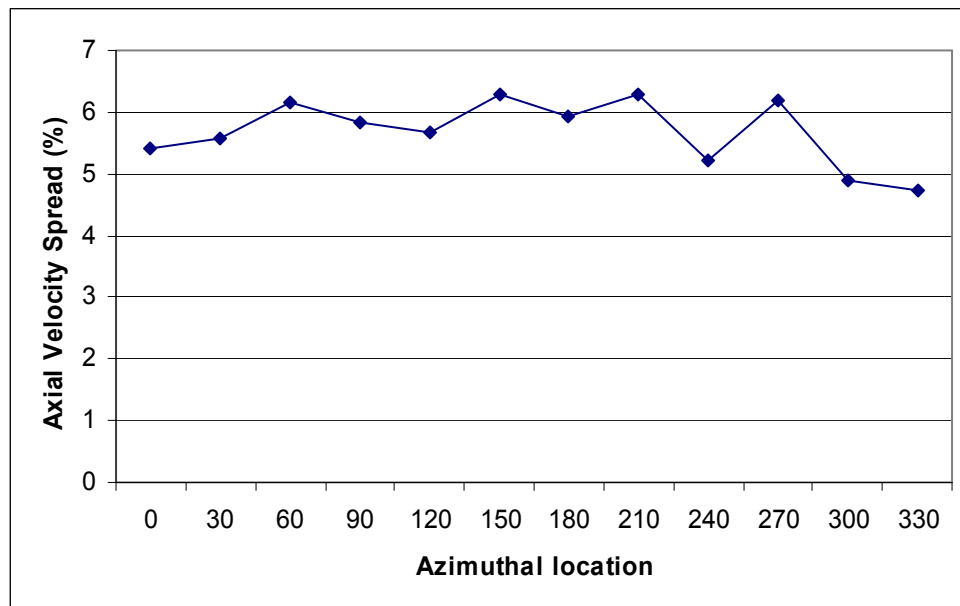


Figure 42 –Variation of the axial velocity spread across beam.

Chapter 6 – Design and Cold-Testing of New Input Cavity

6.1 Analysis of Instability in the Input Cavity

Once the problem of thermal non-uniformity of the MIG emitter was identified, several solutions were pursued. These consisted of (1) a redesign of the emitter and its method of manufacture, and (2) a redesign of the entire MIG. These issues will be discussed in Chapter 9. However, these were long-term and very work-intensive solutions and would not be able to address the problem of poor operation of the gyrokystron in the short term. Therefore, we decided to redesign the input cavity, so as to be able to continue experimental studies before the new MIG was available and in place. We started out by running simulations with Ansoft’s HFSS (High Frequency Structure Simulator) on a model of the input cavity [59]. The results from the eigenmode simulations are tabulated in Table.9.

	Frequency (GHz)	Q-Factor
Mode 1	6.87396	25.6257
Mode 2	7.51255	7.07431
Mode 3	7.69324	11.6197
Mode 4	8.56653	161.712
Mode 5	8.93812	8.17108
Mode 6	8.94864	27.9800

Table 9 – Results from HFSS eigenmode solver.

Mode 2 in Table 9 has a resonant frequency of 7.51 GHz, close to the peak point observed in the experimental spectrum of the instability. The electric field pattern

of this mode is shown in Fig.43. This mode is the TE_{411} . This then is one of the possible candidates for the instability we observed. Mode 4 corresponds to the TE_{011} mode as can be seen in Fig.44. After studying the data from these simulations, we conducted a series of cold-tests of the input cavity to seek experimental corroboration for the theoretical results.

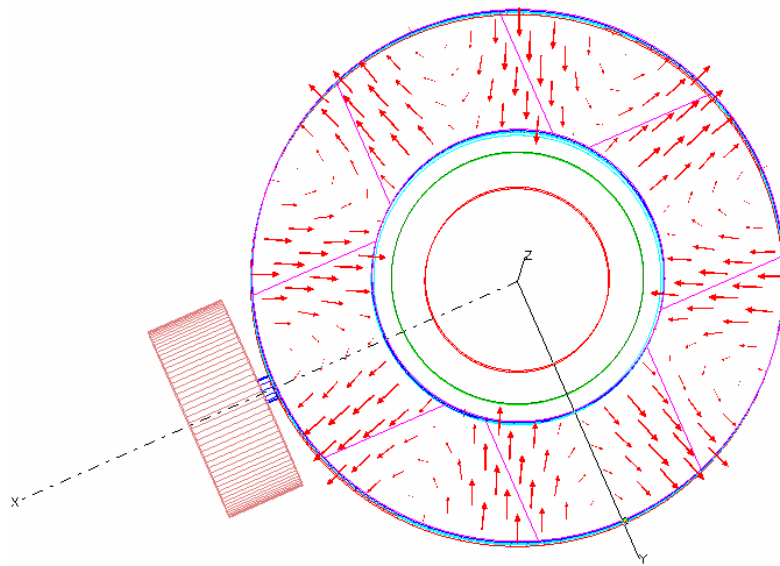


Figure 43 – Electric field pattern of mode 2 from HFSS solutions.

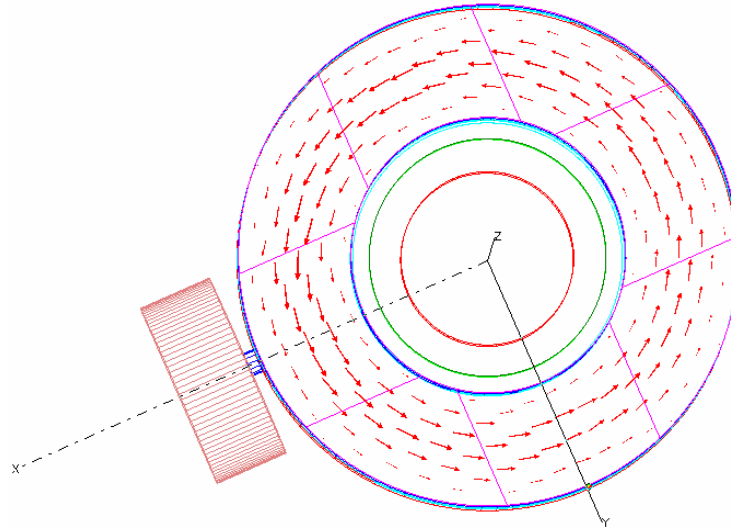


Figure 44 – Electric field pattern of mode 4 from HFSS solutions.

The cold test was conducted with a vector network analyzer. Power was injected into the cavity through the input slot and sampled through holes at 90° and 180° away from the injection. A broadband plot of the S_{21} coefficient for the cavity can be seen in Fig. 45. We identified a resonance centered around 7.52 GHz and with a Q factor of 62. We probed the topology of this resonance by carefully perturbing the fields in the cavity. The procedure followed consisted of inserting a thin probe in the cavity (both conductive and dielectric probes were used), and carefully varying its location (axial, radial and azimuthal), while observing the behavior of the resonances displayed in the network analyzer. The effect of the perturbations on the resonance at 7.52 GHz appeared to confirm that it had indeed a TE_{411} topology. Likewise, we confirmed the presence of our primary mode of operation, the TE_{011} , as the resonance located at 8.585 GHz.

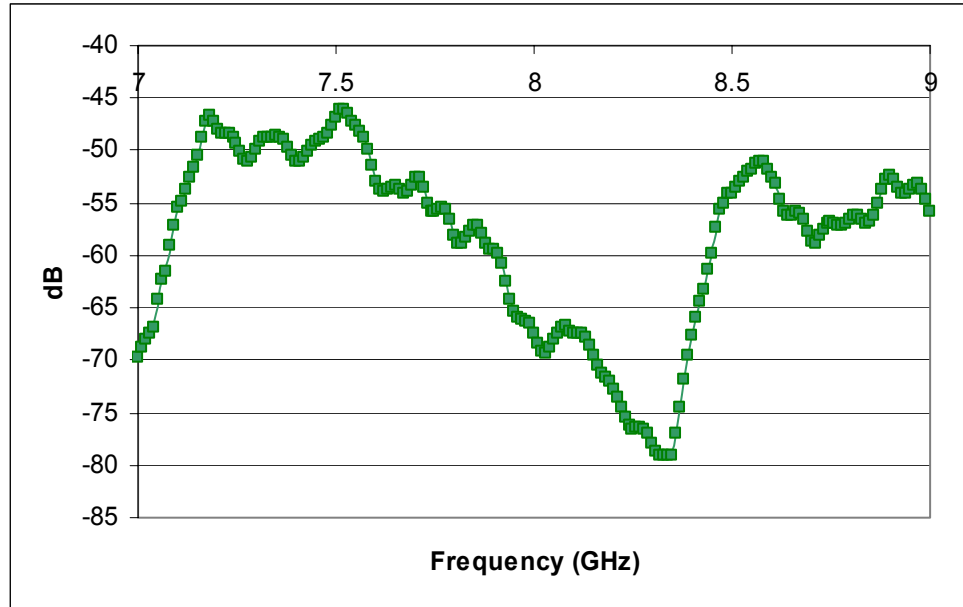


Figure 45 – Broadband S_{21} curve for input cavity.

Now, we wanted to confirm that this TE_{411} resonance could in fact be a component of the instability we observed experimentally. To do this, we used the code QPB (described in Chapter 2) to analyze the behavior of this mode in the input cavity at the operating conditions of our gyrokylystron. Our circuit was designed to operate with a nominal current of 540 A and an α of 1.4. Given the known temperature variations in the MIG emitter, we calculated (based on the formalism described in the previous chapter) that the equivalent local values of the beam current would vary between 336 A and 688 A. Consequently, the α of the beam would vary between 1.53 and 1.31, respectively. We utilized these values and data obtained from QPB to determine the start of oscillation conditions for the TE_{411} mode. Figure 46 displays the curves of the Q-factors required for start of oscillation of the TE_{411} mode for different values of the beam current.

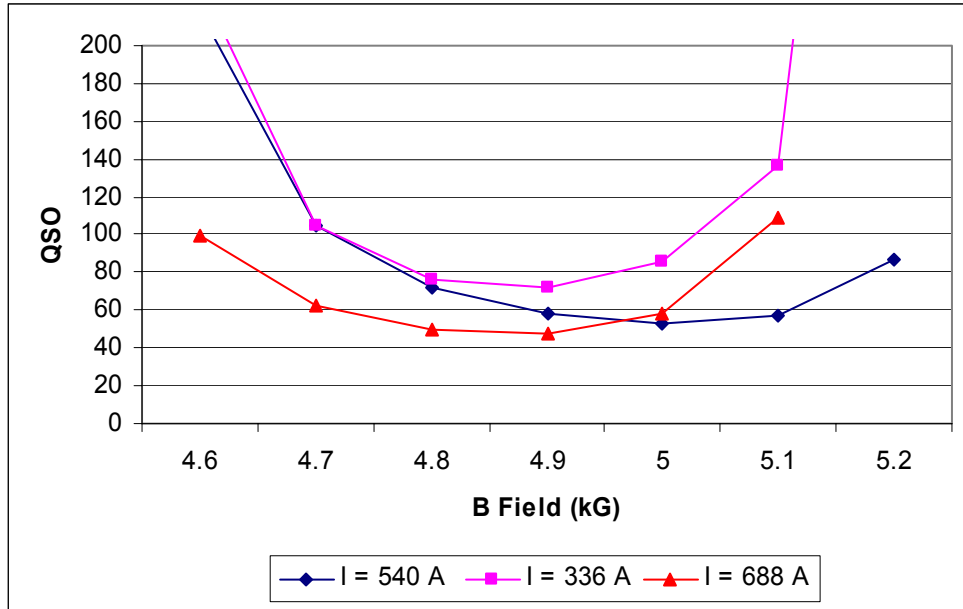


Figure 46 – Start-of-oscillation Q for TE₄₁₁ mode.

The Q of 62 obtained from cold test is clearly above the threshold of start-of-oscillation for the TE₄₁₁ mode in the input cavity for effective beam currents in the range predicted by our calculations and for α equal to 1.4. Thus, this mode is very likely the main cause of the instability observed experimentally. For completeness, I repeated this analysis to study the stability of the cavity with respect to our operating mode TE₀₁₁. The resulting plots of the Q for start of oscillation are seen in Fig. 47. The input cavity is clearly stable for this mode (its cold-test Q is 54, as mentioned in Chapter 4) within the range of predicted effective beam currents.

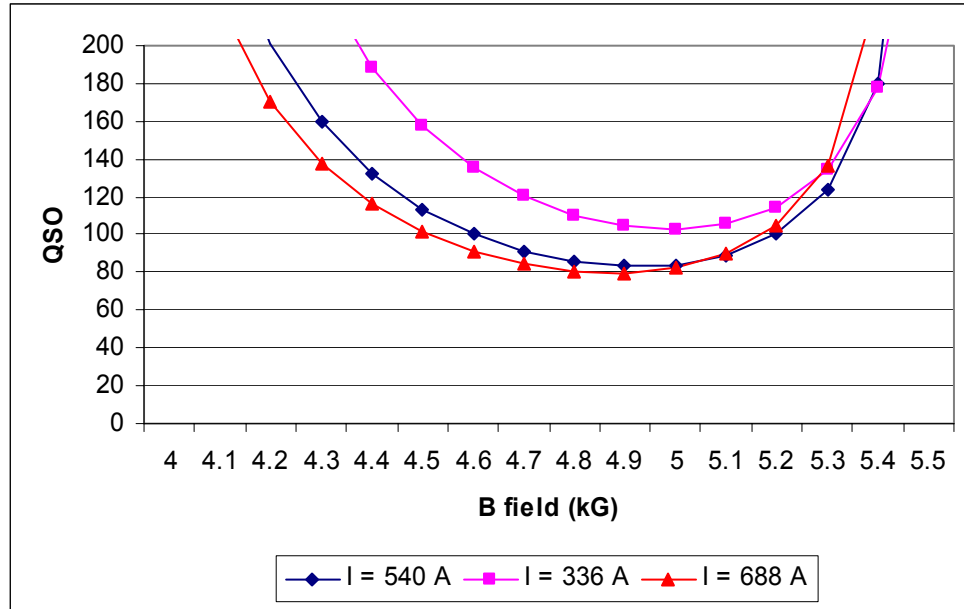


Figure 47 – Start-of-oscillation Q for TE₀₁₁ mode.

6.2 Design of New Input Cavity

We wanted to re-design the input cavity so as to decrease the probability of excitation of any spurious modes (particularly those with $m \neq 0$, such as the TE₄₁₁), while enhancing the coupling of the beam to the TE₀₁₁ mode induced in the input cavity by the input power.

Our approach was three-fold. We decided to reduce the cavity length, reduce its Q-factor, and change its geometrical structure.

By reducing the cavity length, one decreases the distance over which the beam can interact with the cavity, thus diminishing the coupling of the beam to all modes allowed in the cavity. Similarly, reducing the Q-factor of the cavity will decrease the coupling of the beam to modes in the cavity. In particular, we needed to decrease the Q factor of the TE₄₁₁ mode to values below the start-oscillation threshold.

Also, we decided to alter the geometry of the cavity. A comparison of the old and new input cavities can be seen in Fig. 48. The old cavity had an outer radius equal to the drift space, and it was defined solely by a variation of the inner radius. The resistive Q-factor of the cavity was set by a pair of microwave absorbing ceramics carefully located near the edges of the cavity.

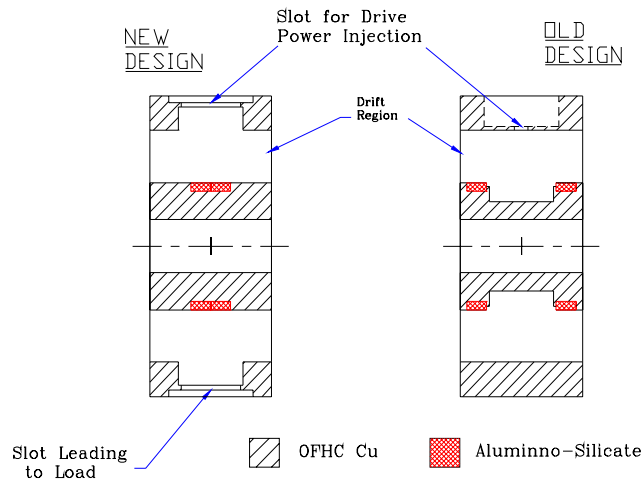


Figure 48 – Cross-sectional view of old and new designs for the input cavity.

This design was altered, so that the new input cavity has an inner radius equal to the drift tube radius and its outer radius is what truly defines the cavity. The change in radii has two main purposes: (a) it allows the placement of dielectric ceramics in the center of the cavity, and (b) it locates the peak of the TE_{011} field closer to the guiding center radius (r_g) of electrons in the beam. The resistive Q is now set by two ceramics placed in the center of the inner-coax region of the cavity. The new placement of these ceramics will preferentially inhibit modes that possess axial wall currents (J_z) (such as

the TE_{411}), while affecting less azimuthally symmetrical modes which only possess azimuthal wall currents (J_θ).

Additionally, the coupling aperture of the input cavity suffered less of a decrease in its length than the cavity itself. The coupling aperture changed from 2.25cm to 1.91cm, while the cavity's length was changed from 2.90 to 1.96 cm, so the aperture covers most (97%) of the cavity. This change, combined with the fact that the peak of the TE_{011} mode excited in the cavity is closer to the guiding center radius of electrons in the beam (r_g), will allow the input signal to couple more strongly to the beam.

Another important criterion that we wanted to preserve was that the diffractive and resistive Q-factors of the cavity were roughly equal (critical coupling), so as to maximize coupling of the input power.

All these changes combined will strongly discriminate against spurious modes, and in particular the TE_{411} mode observed, hence moving the effective restriction on α imposed by the onset of these instabilities to a higher value.

6.3 Cold-Testing of New Input Cavity

The design of the cavity started with a preliminary choice of target criteria: a decrease in the cavity length by at least 10%; a final Q-factor for the cavity near 35; and a change in the geometry of the cavity and the placement of ceramics outlined above.

I started out by running COAX simulations seeking a cavity geometry with the inner radius set by the drift space, with a resonant frequency near 8.568 GHz, and with a length at least 10% shorter than our original input cavity. The simulations yielded

several candidate geometries. Then I fabricated prototypes based on the COAX models. These prototypes were fitted with coupling slots and circular holes for cold-testing. I then tested these cavities with different ceramics placed at the central regions using a vector network analyzer.

A long iterative process followed in which the cavities were tested and then machined further to adjust their resonant frequencies and diffractive Q-factors. Then, different ceramics were tried attempting to conform to the criterion of equal diffractive and resistive Q-factors.

The final model called for two coupling slots instead of one (as in the original input cavity) in order to obtain the appropriate Q's. Based on this final model, the new input cavity was machined. It was also cold-tested, yielding final values of Q-factor and resonant frequency for the TE₀₁₁ mode equal to 31 and 8.575 GHz, respectively. The S₂₁ (transmission coefficient) curve of the final input cavity is shown in Fig. 49.

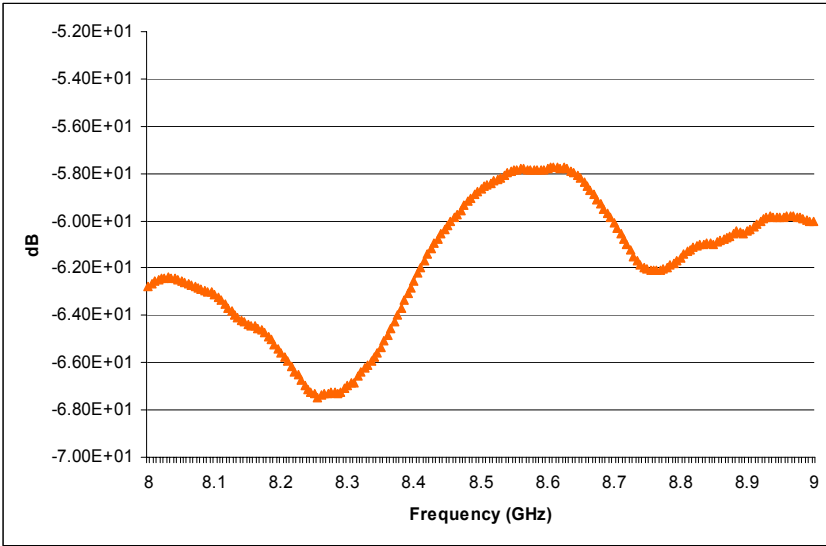


Figure 49 – S₂₁ curve for final input cavity.

A broadband view of the transmission coefficient curve is displayed in Fig. 50. As can be seen in this plot, the TE₄₁₁ mode occurs at 7.48 GHz, and has a Q of approximately 32 well below the start of oscillation curves shown in Fig. 46. Thus, this cavity should remain stable, not allowing the TE₄₁₁ mode to become excited under the presence of the electron beam (with parameters within our operating range).

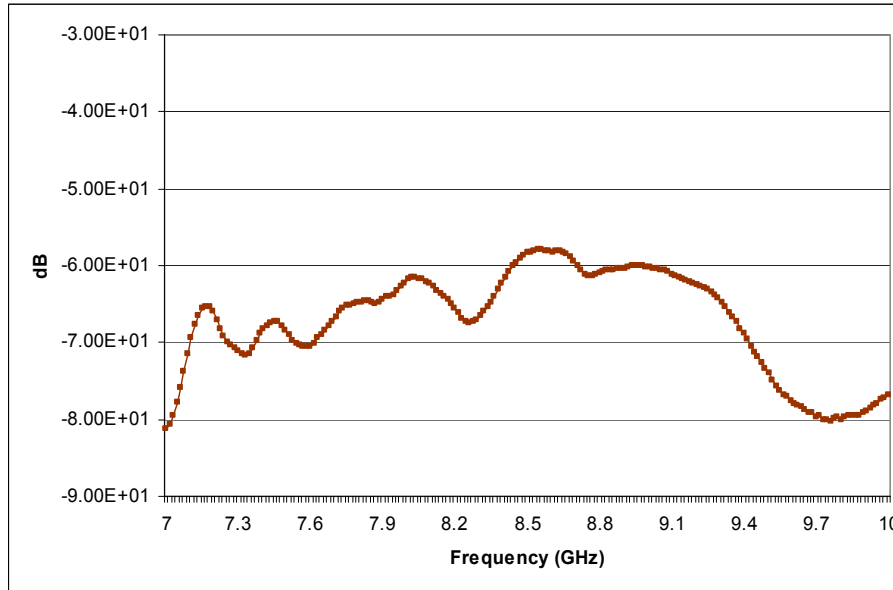


Figure 50 – Broadband S₂₁ curve for final input cavity.

6.4 Theoretical Performance of Circuit with New Input Cavity

Now, the use of an input cavity with lower Q-factor was likely to affect the overall efficiency of the four-cavity gyrokystron. So I decided to investigate the consequences of this new input cavity. I ran MAGYKL simulations using the new input cavity, while keeping all other parameters of the tube equal to the original design. The results of the simulations can be seen in Fig. 51. As expected, the lower Q-factor of the cavity leads to lower efficiencies and gains for the whole gyrokystron circuit. For $\alpha=1.4$, the maximum efficiency predicted is 32.6% with an input power of 2.2kW,

yielding a gain of 45.6 dB. If compared to the original theoretical design of the circuit with the old input cavity, one will find that this model represents a decrease in the efficiency of 2% and a reduction of gain by 10 dB. This circuit can still be driven by the TWT recently acquired by the University of Maryland GKL group, which has a maximum output power of 2.7 kW near 8.5 GHz.

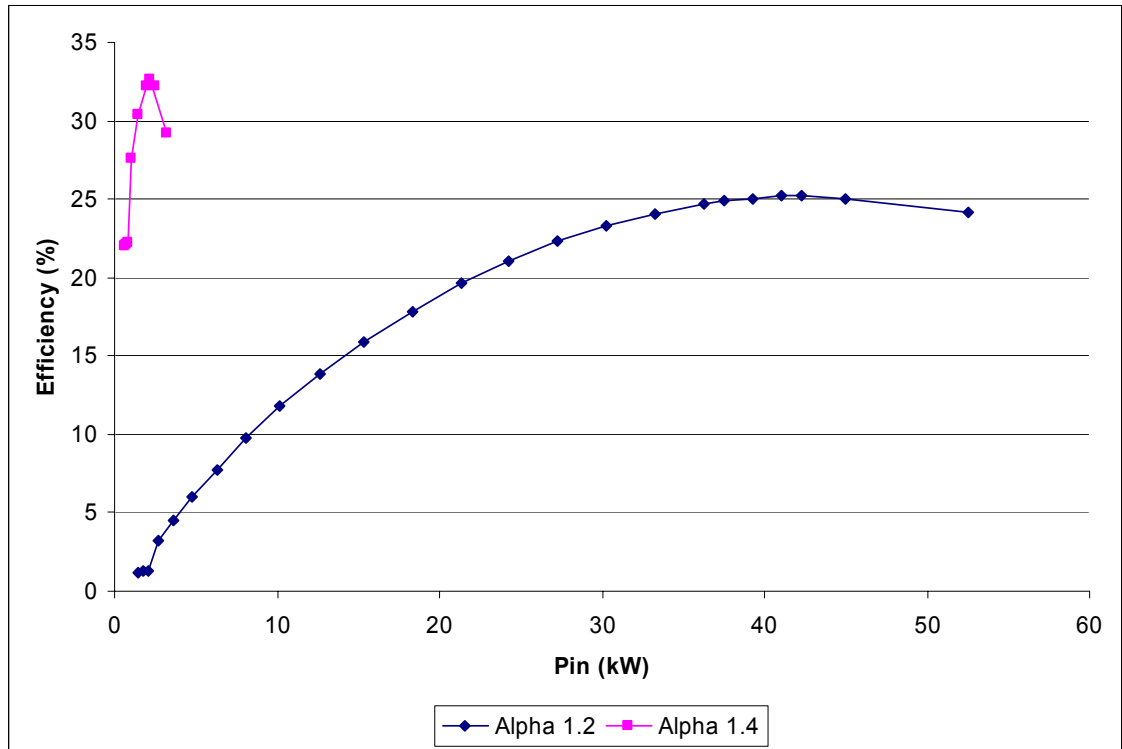


Figure 51 – Performance of gyroklystron with new input cavity (from MAGYKL).

The performance of the four-cavity gyroklystron exhibited above does not take into account the emitter temperature variation problem. We plan to replace the present emitter in our MIG by a newly fabricated emitter which has been designed so as to minimize the temperature variation across its surface. However, until the new emitter is inserted into the MIG, we will continue to experience the effects of thermal variation of the emitter on the quality of our electron beam. So, even though we may have resolved the issue of instabilities in the input cavity (which should allow us to operate at the

design value of α , around 1.4), we will still experience lower efficiencies and gains. This effect is a non-linear and very complex 3-dimensional problem, however I attempted to model it with our 2-D codes so as to estimate what the performance of my gyroklystron is likely to be with the current defective emitter.

I modeled the emitter by dividing it into twelve segments, each with a uniform temperature. The values of the temperature were obtained from pyrometric studies of the emitter (see Figs. 37 and 39). I calculated the current density of each section, and estimated the equivalent local beam currents for a distribution centered around our nominal value of 540 A, as discussed in Chapter 5. I then used these currents to calculate corresponding values of α and of the axial velocity spread with EGUN. Finally, I ran the code MAGYKL, and calculated the efficiency of the four-cavity gyroklystron for each of the twelve sets of beam parameters. Afterwards, I computed the output power produced from each set and averaged the results of all twelve segments. From this value I calculated the overall efficiency of the amplifier for the average beam current at a specific level of input drive power. The procedure was then repeated for different values of input power. The final results for these studies for α of 1.4 are displayed in Fig. 52. The model predicts a decrease of both efficiency and gain as expected. The maximum efficiency predicted is 28.4%, corresponding to a gain of 43.3 dB with an input power of 3.24 kW. Since our TWT has a maximum output of 2.7 kW this operating point is unattainable. Furthermore, once line losses are considered, the maximum power available for driving the gyroklystron should be approximately 2 kW. At 2.22 kW the model for the defective emitter predicts that we will still have an efficiency of 25.9% corresponding to an output power of 64 MW. Therefore, even with

a defective MIG emitter, this modified tube should still fulfill well the function that it was originally designed for, that is, to drive the Haimson Linear Accelerator (described further in Chapter 8).

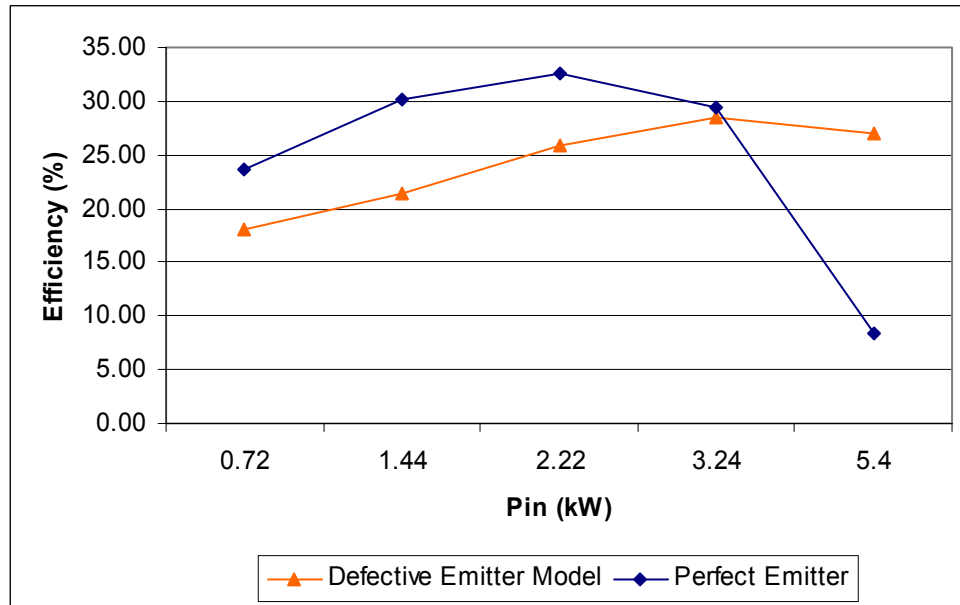


Figure 52 – Performance of gyrokystron with defective emitter (MAGYKL).

Chapter 7 – Design of New Radial-Extraction Output Cavity

7.1 Introduction

In this chapter I will describe my work concerning the design of a new type of output cavity for future gyroklystrons.

Our present gyroklystron design (which was described in detail in Chapter 4), consists of four overmoded cavities: the input, the buncher, the penultimate and the output cavity. The present output cavity (which can be seen in Fig. 17) has a drift region on its upstream boundary, where the TE_{021} mode is cutoff, while its downstream boundary contains a small transition (“lip”) followed by a waveguide section. This lip is especially designed to set the diffractive Q of the cavity, while at the same time maximize the coupling of the TE_{021} mode generated within the cavity to the waveguide section downstream. Thus power from the output cavity is extracted axially, exiting the cavity concurrently with the spent electron beam. This can be contemplated in Fig. 53.

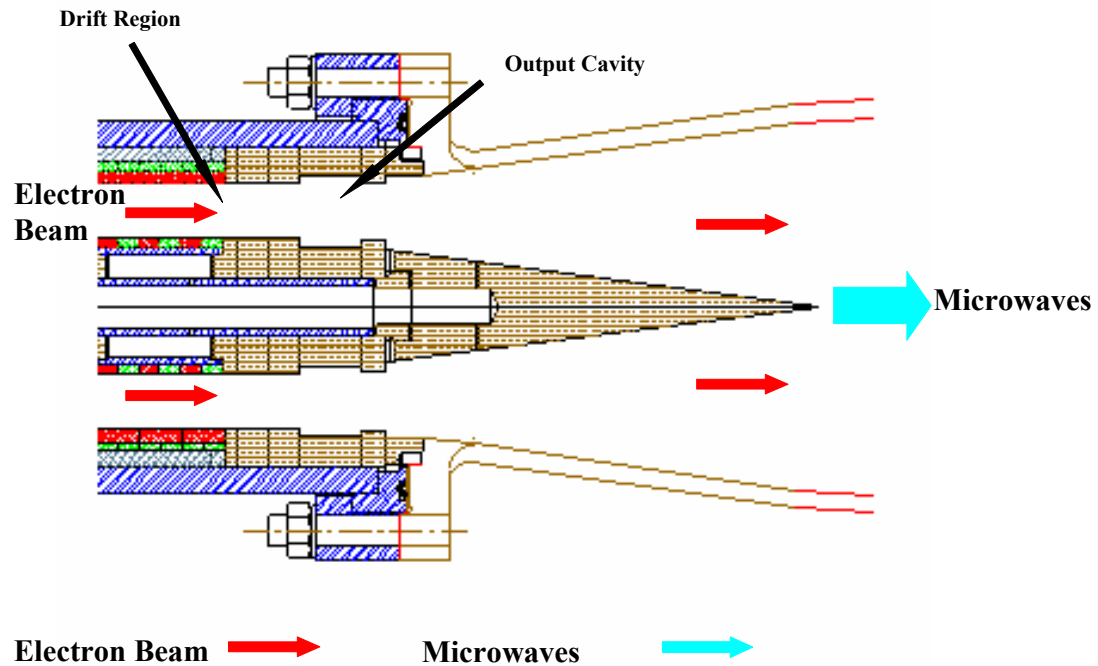


Figure 53 – Current axial-extraction output cavity.

This scenario has several drawbacks. The primary two concerns are (a) the microwave-beam interaction after the output cavity, and (b) the need for complex system of output tapers for power transport and mode conversion. The field strengths at the output end of the cavity are typically high, especially once the tube operates near its design criteria. Hence, the microwave-beam interaction may become very significant in the region between the output cavity and the beam dump, where the electron beam is finally terminated. This interaction can compromise the quality of the microwave power extracted from the gyrokylystron, by causing losses in power as well as in mode purity of the output signal. Furthermore, the microwave-beam interaction can lead to the generation of various spurious modes (especially in the tapered sections, which could act as local resonant cavities). These spurious modes could propagate back into the

gyroklystron interfering with its operation. They could also jeopardize the zero-drive stability of the gyroklystron.

With respect to the output power transport, axial power extraction makes it necessary to use a complex system of tapers so as to simultaneously allow beam dumping and adjust for the correct mode and waveguide size of the output microwaves. Irrespective of any microwave-beam interactions, the very presence of tapered transitions can lead to reflections and mode conversions. Spurious modes can be generated in these tapers which could interfere with amplifier operation. The danger of electrical breakdown is another concern, since local enhancement of fields becomes more probable as the output power travels through more waveguide transitions.

Thus, it would be desirable to extract power from the output cavity in a manner that would isolate it from the spent beam, while simultaneously allowing for the power to exit in a mode that minimized the need for taper conversions. The need for such an alternate method of power extraction may become more urgent once the gyroklystron circuit is operating near its optimal design parameters. It was under this mandate that we pursued a radial-extraction output cavity.

A schematic diagram of this concept is presented in Fig. 54. In this design, the output power generated in the output cavity would couple to an inner extraction cavity through slots on the inner wall of the coaxial output cavity. Radial coupling is achieved by taking advantage of the fact that the TE_{021} coaxial mode (the characteristic mode generated in the output cavity) has strong axial magnetic fields at the inner and outer conducting walls of the cavity. These lead to the generation of the TE_{01} mode in the

inner coaxial guide (via magnetic coupling). The inner waveguide is designed to propagate the TE_{01} coaxial waveguide mode out of the gyroklystron.

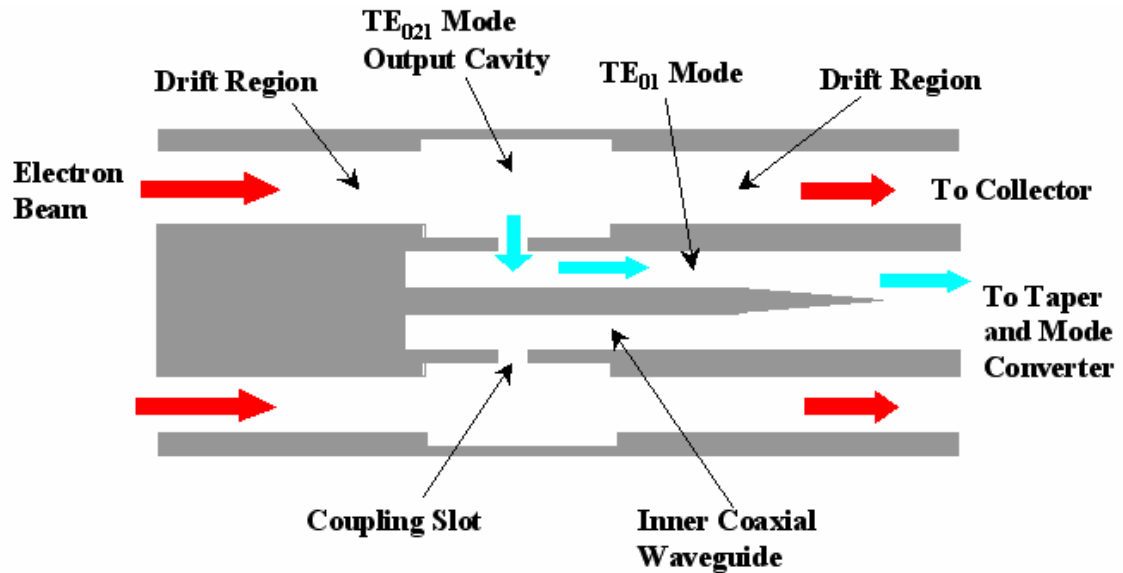


Figure 54 – Radial-extraction output cavity.

The TE_{01} mode is the desired output mode for several reasons. Firstly, this mode is the simplest and most natural to occur in the innermost guide based on the geometry of the cavity in Fig. 54. Also, the TE_{01} mode can be easily transported in circular waveguide, with very low losses. Furthermore, this mode is the desired output mode for accelerator applications that utilize pulse compression [60], and it can be easily converted directly into rectangular waveguide modes (a converter for this purpose is discussed in Chapter 8).

A similar radial-extraction cavity has been designed in the past by James Anderson [60]. I revisited this concept and performed my own design so as to obtain an improved model of the cavity.

7.2 Design Procedure

We started the design of the new radial-extraction cavity with design parameters of the conventional (axial-extraction) output cavity obtained with the GYCOAX and MAGYKL codes. This is important, since the overall design of the entire gyrokystron tube has been optimized based on the precise parameters of all four cavities. Therefore, any new version of the output cavity needs to match the fundamental parameters of the old output cavity so as to maintain the performance of the whole gyrokystron circuit. In particular, the new output cavity needs to have approximately the same electromagnetic features (resonant frequency and Q-factor) and geometric dimensions (same length, similar outer and inner radii).

Ansoft's High Frequency Structure Simulator (HFSS) was used for this design [59]. We created a three-dimensional model of the cavity which can be seen in Fig. 55.

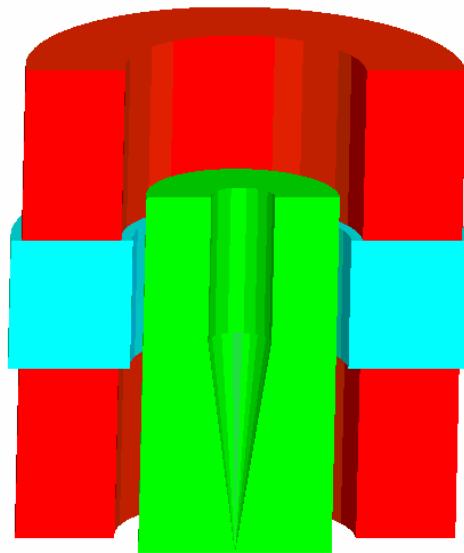


Figure 55 – Three dimensional model of new output cavity.

Figure 56 shows a simplified cross section of the model with its elementary constituents. Notice that, unlike the axial-extraction cavity, the downstream boundary of this new cavity is occupied by a drift space region which is cutoff to the TE_{021} mode (just like the upstream boundary of the cavity - see Fig. 55). Another important component of this new model is the presence of a conical taper in the inner waveguide (region 5 in Fig. 56) which serves for converting the coaxial TE_{01} mode generated in the innermost cavity into a TE_{01} circular mode that is transported through the output waveguide system.

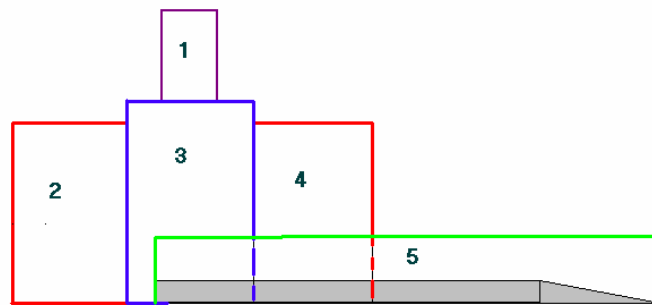


Figure 56 – Simplified cross-sectional view of model. 1 - Injection Port, 2 -Upstream Drift Region , 3 – Output Cavity, 4 – Downstream Drift Region, 5 – Inner Guide for Power Extraction.

HFSS simulates the cold-test performance of the cavity. Thus one simulates injecting power from an input port (in WR62 rectangular waveguide), which excites a TE_{021} mode in the cavity, and in turn leads to the generation of the TE_{01} mode in the inner guide. Figure 57 displays the electric fields seen in a mid-plane cross-sectional cut of the model. For the purpose of these simulations we used a model that had a quarter of the structure, with the symmetry cuts defined as perfect electric boundaries. This way, the code only considered modes whose electric fields were continuous across the

symmetry cuts. The field pattern of the TE_{021} mode is clearly visible in the cavity (although not pure), while the TE_{01} mode pattern appears in the inner-coaxial guide.

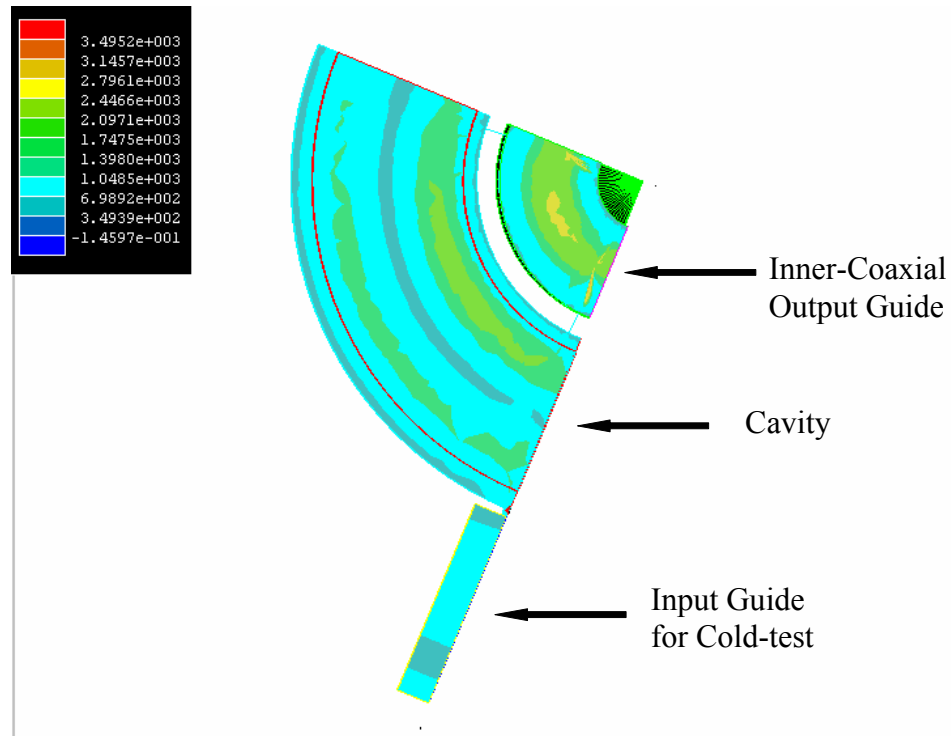


Figure 57 – Cross-sectional electric field distribution.

The power extraction from the inner guide is well illustrated in the longitudinal profile of the electric field which is seen in Fig. 58. Notice that the electric fields only penetrate a very limited distance of the drift regions. The addition of microwave absorbing ceramics (which were not included in these simulations) would decrease these fields even further. Once again, the electric field patterns indicate the presence of the TE_{021} and the TE_{01} modes in the cavity and inner guide, respectively.

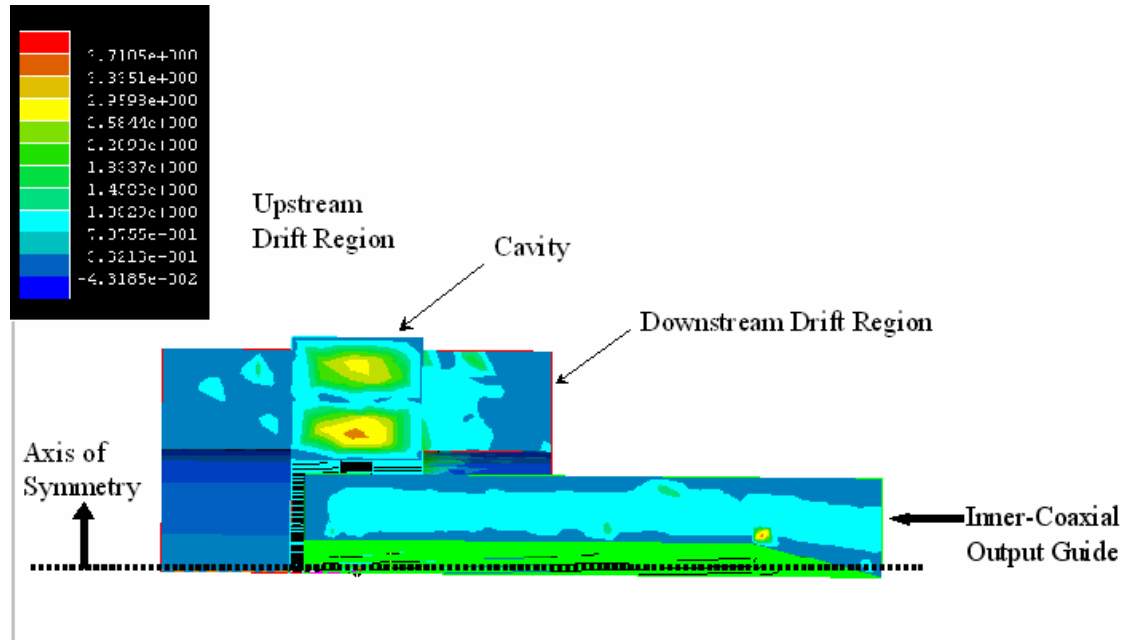


Figure 58 – Longitudinal electric field distribution.

In order to optimize the design we altered various parameters. The primary parameters studied were: the thickness of the inner wall of the output cavity; the axial position and angle of the conical taper; the number of coupling slots; the angular width and axial length of coupling slots. The model was optimized to fulfill the requirements of the four-cavity gyrokystron tube, in particular $f_R \sim 17.115$ GHz, with a Q-factor around 310, and a total efficiency of power extraction from the output cavity greater than 90%.

7.3 Final Results

The final design obtained had four coupling slots, and its electromagnetic characteristics are listed in Table 10. The geometric specifications of this cavity can be seen in Table 11. The final model had a resonant frequency of $17.088 \pm 0.015\text{GHz}$, which is only 17 MHz away from the old output cavity. Likewise the Q of this new cavity is 334 ± 20 which is close to $Q = 310$ of the old cavity.

Resonant Frequency (f_R)	$17.088 \pm 0.015\text{GHz}$
Quality Factor (Q)	334 ± 20
Transfer Ratio into TE01	$97.5 \pm 0.5 \%$

Table 10 – Electromagnetic properties of new output cavity.

Output Cavity	
Outer Radius	3.53 cm
Inner Radius	1.69 cm
Axial Length	2.00 cm
Coupling Apertures	
No. of Apertures	4
Axial Length	5.08 mm
Angular Width	81.5°
Inner-Coaxial Guide	
Outer Radius	1.46 cm
Inner Radius	0.48 cm

Table 11 – Geometric parameters of new output cavity.

We found that the axial length of the coupling slots was one of the most important factors in determining the resonant frequency and quality factor of the output cavity. Figure 59 shows the relationship of the slot length to f_R and Q. Note that Q is particularly sensitive to the slot length, varying by a factor of 10 for a slot length change of less than 0.5 mm.

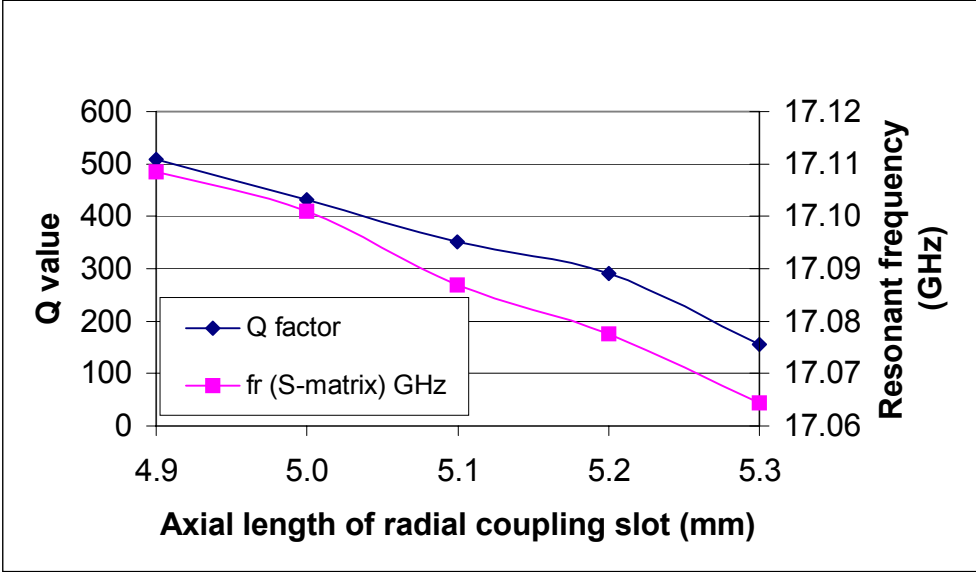


Figure 59 – Resonant frequency and Q as a function of slot length (from HFSS).

The curve of the transmission coefficient for the TE_{01} output mode is presented in Fig. 60. Meanwhile, Fig. 61 displays the reflection coefficient for injection through the input port of the final model. The peak in Fig. 60 appears to have a low magnitude ($S_{21} = 0.14$), however this is due to the fact that so much of the input power injected into the cavity is reflected at the injection port. Notice that the depression in Fig. 61 corresponding to the same frequency has a reflection parameter $S_{11} = 0.99$. When this fact is taken into account one realizes that the power transferred into the output guide is approximately 98 % of the power injected.

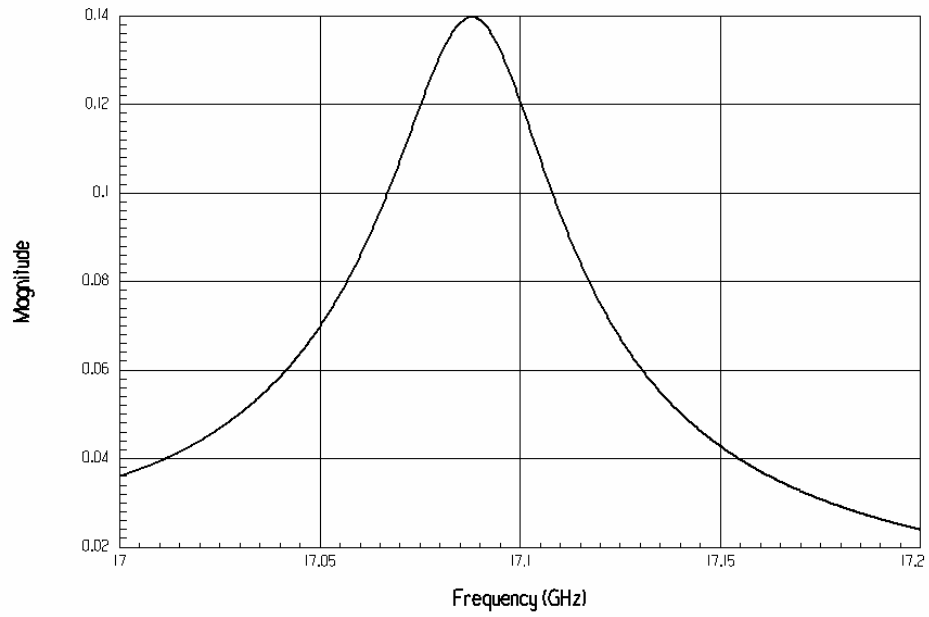


Figure 60 – Transmission coefficient for TE₀₁ mode.

The final design fulfills all the desired criteria, and is thus a good candidate for the output cavity of a future implementation of the four-cavity gyrokystron.

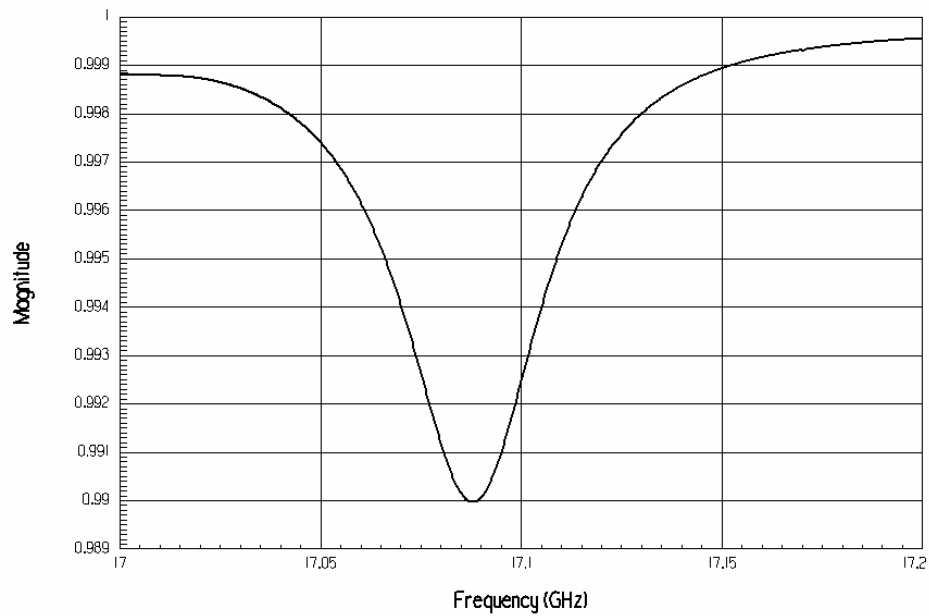


Figure 61 – Reflection coefficient of the new cavity's injection port.

Chapter 8 – Output Power Transport System and Linear Accelerator

8.1 Introduction

As I discussed in Chapter 1, the gyrokystron is a good candidate for driving future particle accelerators, since it is capable of producing high powers at high frequencies. This is due to the fact these devices scale well with frequency, and are capable of multiple harmonic operation. However, to date there has been no attempt to actually drive an accelerator with a gyrokystron. CERN has recently commissioned the design of a gyrokystron from CPI (Communication and Power Industries) so as to test its potential in accelerator applications. The gyrokystron group at the University of Maryland intends to pursue this approach as well, by performing proof-of-principle experiments in accelerator drive.

The four-cavity second harmonic gyrokystron described in this work was designed specifically for the purpose of driving a linear accelerator structure fabricated by the Haimson Research corporation (HRC) [61]. The output power produced in the gyrokystron exits in the TE_{02} circular mode, while the power needed to drive the accelerator must be delivered in two rectangular WR62 waveguides in the TE_{10} mode. Thus, in order to use the gyrokystron to drive the linear accelerator structure, an entire new range of microwave components had to be designed so as to allow the transport and appropriate conversion of the gyrokystron output microwave power. These included tapers, bends and mode converters.

My main contribution to this effort to date was centered on the re-design of a circular TE_{01} to rectangular TE_{20} mode converter, which was a key element of this new

output power transport system. In this chapter I will describe this effort. I will also briefly discuss this transport system and the high gradient linear accelerator that will be powered through it.

8.2 Design of Circular to Rectangular Converter

The original concept for this type of converter was developed for X-band applications at SLAC [62]. At the University of Maryland, we scaled the X-band design to Ku-band, and then made adjustments to optimize the performance [63].

The converter is depicted in Fig.62. It consists of three main sections, with very specific geometries.

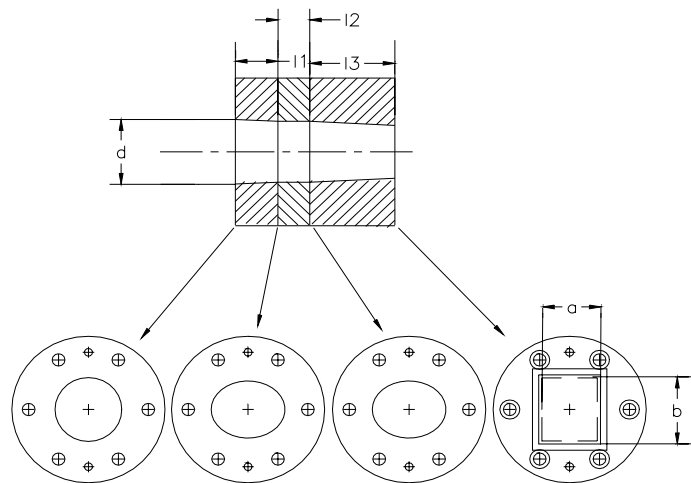


Figure 62 – Cross-sectional view of converter.

The most unusual section is the central one, which has a constant cross-section where the radius (in cylindrical coordinates) is defined by:

$$r(\phi) = r_0(1 + \Gamma \cos(2\phi)) \quad (8.1)$$

where ϕ is the azimuthal angle, r_0 is the average radius and Γ is a free numerical factor (< 1) that can be varied to optimize the conversion characteristics. The other two sections consist of tapers whose geometry gradually changes from that defined by (8.1) into either a circular guide or a rectangular guide.

In order to modify the SLAC design to Ku-Band, while maintaining the same high efficiency of the original concept and the same degree of mode purity, we decided to retain the relative cross-sectional shapes of the central region and of the circular and rectangular tapers. The dimensions of the converter were then fixed by scaling. We also altered the parameter Γ of the original model, for each value of the scaling factor (S) to determine which combination of Γ and S enhanced the conversion features of the converter. The design was performed based on three main criteria: (a) the central frequency of the converter should be close to the design output frequency of our gyrokystron (17.136 GHz), (b) the converter should have a power transfer higher than 99.9 % over the entire 300 MHz bandwidth, and (c) spurious modes must have amplitude levels of less than -30 dB.

In order to investigate the properties and behavior of each design variant of the converter, we performed extensive computer simulations of each model. We utilized the software package HFSS. The three-dimensional model of the converter can be seen in Fig. 63.

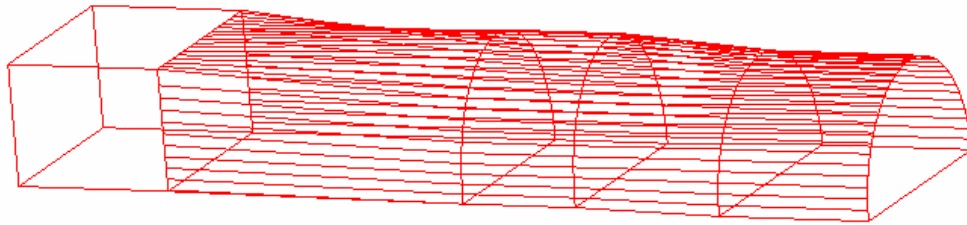


Figure 63 – 3-D Model of converter.

The most dangerous spurious mode was found to be TE_{02} rectangular - the symmetric counterpart of the desired output TE_{20} mode. Our priority was to diminish as much as possible the effective coupling of this spurious mode to the input TE_{01} circular mode, while enhancing the coupling of the TE_{20} rectangular mode.

<p>Circular Taper $l_1=1.676$ cm $d=2.656$ cm</p>
<p>Central Region $l_2=1.257$ cm $r_0=1.328$ cm Γ parameter 0.105</p>
<p>Rectangular Taper $l_3=3.353$ cm $b=2.597$ cm $a=2.179$ cm</p>

Table 12 – Final dimensions of converter.

The final dimensions of the converter are listed in Table 12. The characteristic scattering parameter (S) curves of the converter obtained from computer simulations are displayed in Figs. 64 and 65. The central frequency of the converter's bandwidth is 17.15 GHz.

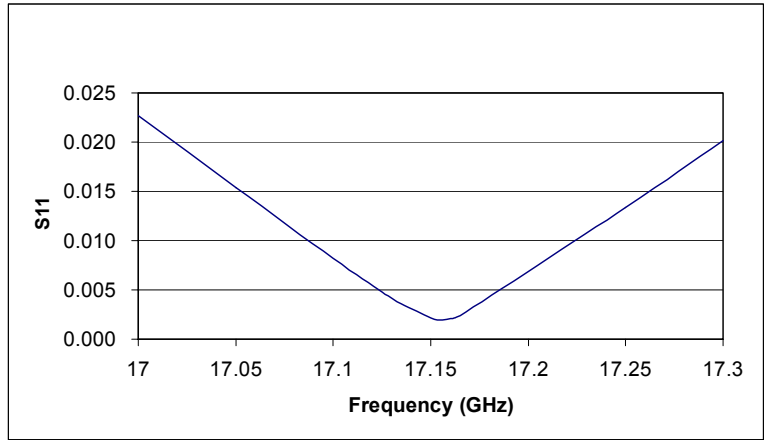


Figure 64 – Reflection coefficient of converter.

Figure 64 shows the reflection coefficient at the input port of the converter. Its values are between -33 and -53 dB over the range of 300 MHz. The power transfer ratio between the TE_{02} circular mode and the TE_{20} rectangular mode varies from 99.94 to 99.98 % over the same frequency range (see Fig. 65). At the expected output frequency of the gyrokystron (17.136 GHz) it is about 99.98% with a reflection of -50 dB. Thus, this final design fulfilled the original design goals.

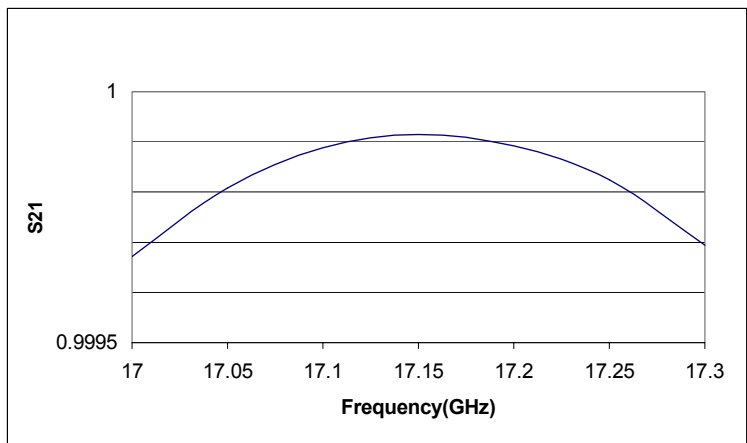


Figure 65 – Transmission coefficient of converter.

8.3 Overview of Power Transport System

Figure 66 displays an engineering drawing of the entire power transport system and coupling to the HRC accelerator. As mentioned above, there is a significant number of microwave components which are necessary for the integration of the high gradient Accelerator with our gyroklystron. These components needed to fulfill very stringent design criteria. All microwave components needed to be very carefully designed so as to accomplish their specific function (whether re-directing, tapering or mode converting microwave power) with a minimum amount of reflections, and without exciting spurious modes. Such modes could interfere with the operation of the gyroklystron, affecting its performance and compromising zero-drive stability. Furthermore, spurious modes would degrade the quality of the power delivered to the accelerator by diminishing mode purity and introducing amplitude and phase variations.

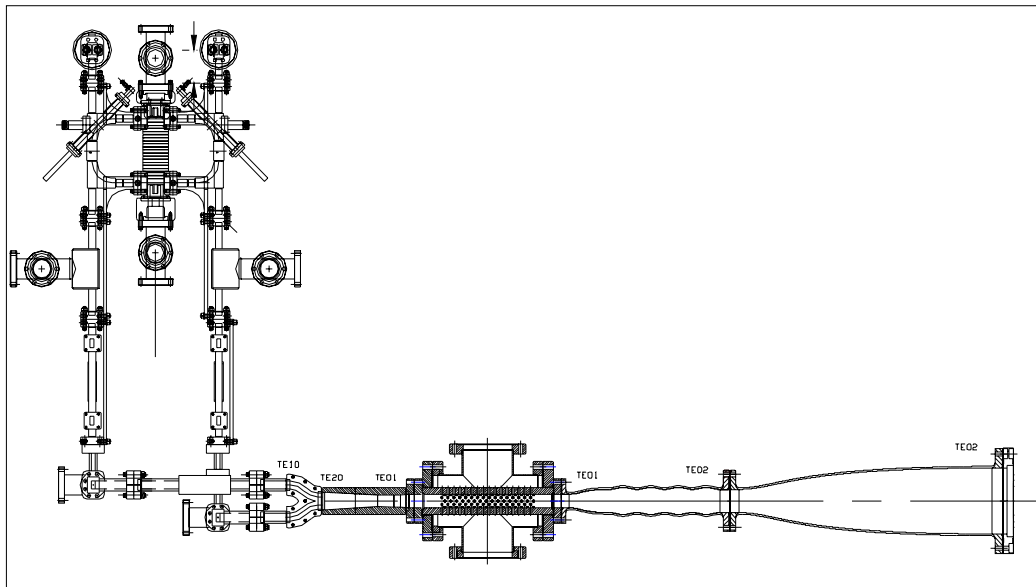


Figure 66 – Complete view of power transport system coupled to accelerator.

All microwave components must also be capable of handling high peak fields associated with the 10-80 MW of power they will experience, while minimizing the probability of electrical breakdown. Lastly, all components must be able to sustain ultra-high vacuum. Most components of the transport system were designed and modeled using the HFSS finite element code. At this point in time, all mechanical design and drawing have been completed and all of the components are at some stage of fabrication.

Next, I will describe the various components of the system while following the path of the power that exits the gyrokystron. Note that the generation of power in the gyrokystron and its usual transport and diagnostics have already been described in Chapters 3 and 4.

Once the accelerator transport system is implemented the output power leaving the gyrokystron through the alumina output window will not be tapered into the anechoic chamber. Instead, a non-linear downtaper with normalized power transfer of 99.9 % will lead the power to a periodic rippled-wall converter. Figure 67 displays a cross-sectional view of this converter. This converter was designed with the code NLTAPER [55] and will convert the TE_{02} circular mode that exits the gyrokystron into a TE_{01} circular mode. Then the microwaves pass through a Dolph-Chebyshev circular taper with a normalized power transfer of 99.7 %, and enter the compact circular to rectangular converter which was described earlier. The power leaves this converter in the TE_{20} rectangular mode. Following this converter, a bifurcation divides the power along the broadwall of the waveguide equally into two rectangular guides. In this process, the bifurcation effectively converts the TE_{20} rectangular mode into the TE_{10}

rectangular mode in two waveguides. An engineering drawing of the bifurcation can be seen in Fig. 68.

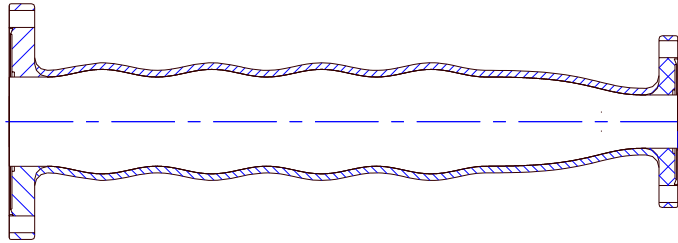


Figure 67 – Rippled-wall converter.

Linear tapers then bring the wall dimensions to those of standard WR62 waveguide. Both E-plane and H-Plane bends are used to re-direct and align the waveguides carrying the power with the accelerator feeds. Also, an adjustable phase shifter is used to experimentally calibrate the system so as to ensure that the microwaves carried in the two parallel guides are in phase with each other. The microwave power is then transported in the TE_{10} mode into the dual feeds of the accelerator structure.

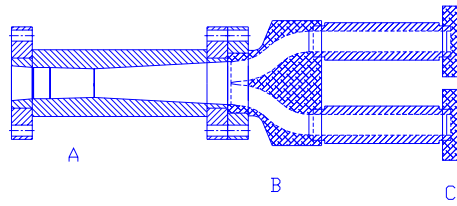


Figure 68 –Schematic of part of the output waveguide system (A - circular to rectangular mode converter; B - Bifurcation; C- Linear tapers).

Other integral components of the transfer system are the high conductance pumping crosses. These incorporate perforated stainless-steel jackets which allow for pumping of the waveguides, while preventing microwave power from escaping into the ion pumps. The circular pumping cross and its insert are shown in Fig. 69.

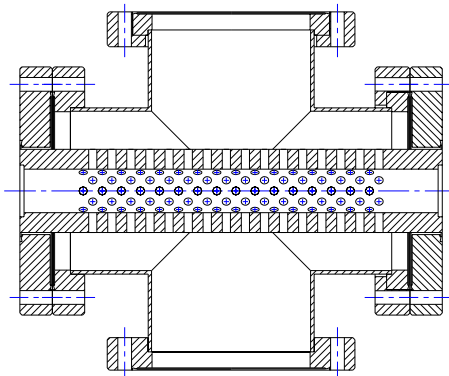


Figure 69 – Circular pumping cross.

8.4 The HRC Linear Accelerator

Figure 70 shows a schematic diagram of this accelerating structure. The HRC linear accelerator utilizes a high-peak power multiplier system based on a dual hybrid feed (TE_{10}) bridge configuration [61]. It was designed to operate at 17.136 GHz with input power levels between 10 and 75 MW, and pulse lengths greater than 250 ns.

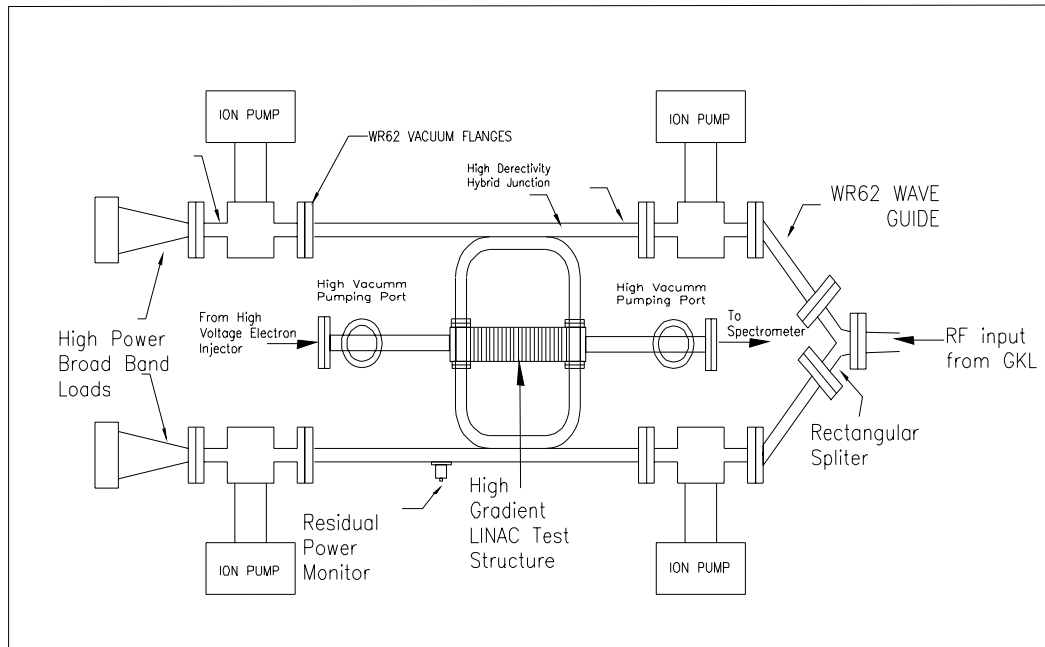


Figure 70 –Schematic of linear accelerator.

The accelerator was designed so as to produce high accelerating gradients by effectively multiplying its input power. This is achieved by the use of two directional couplers which couple the input power to the accelerating section. The couplers have a transmission coefficient of 0.866, and thus only allow a portion of the input power to enter the linac, the remaining power is led to water loads. In turn, part of the power from the linac re-enters the hybrids. As time within a given input source pulse

progresses, the power in the accelerating section of the structure builds up to approximately four times the source power. A representation of this phenomenon is displayed in Fig.71 [61]. Experiments with this structure will constitute proof-of-principle for these novel accelerator concepts.

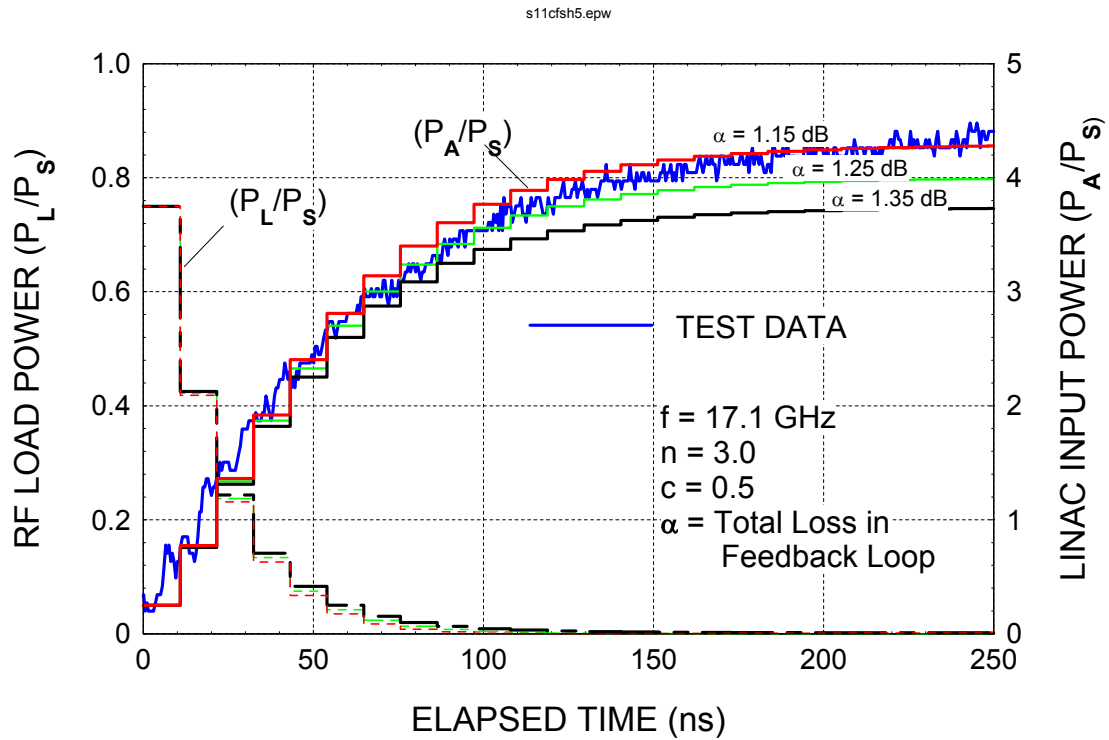


Figure 71 –Build-up of power in accelerating structure.

Chapter 9 – Summary and Future Work

In this thesis I have chronicled the work I have performed while pursuing my doctoral degree. During this time, my central objective was to produce a four cavity second-harmonic gyrokystron capable of serving as driver for the HRC linear accelerator. I performed the design of this circuit, then I implemented it as described in Chapter 4. The experimental results obtained confirmed that amplification did indeed occur, however the performance of the circuit was lower than the design parameters, as was shown in Chapter 5. We obtained pulses with a peak power of 18.50 ± 1.67 MW, and a FWHM time of $0.73 \mu\text{s}$. An instability was detected in the input cavity, which was responsible for limiting the operation of the gyrokystron to a regime where the velocity pitch ratio (α) was below 0.9 (much lower than the design value of 1.4). In this regime the performance of the gyrokystron is expected to be poor. In order to counteract this problem, I re-designed the input cavity (as was discussed in Chapter 6) so as to eliminate the instabilities that hampered the experiment. Therefore, we should finally be able to operate the gyrokystron in regions near the design parameter of $\alpha = 1.4$.

The decrease in the experimental performance of the tube is ultimately due to the significant temperature variation across the MIG emitter. As explained in Chapter 5, the temperature variation leads to a variation in the current density of the electron beam which increases the spread in velocity and α leading to the likelihood of instabilities. And even though my new input cavity may eliminate the instability that constituted the primary cause of low performance, the poor beam quality due to the defective emitter

will still decrease the efficiency and gain of gyrokystron. Therefore this issue needs to be addressed. We believe that this imperfection in the emitter is caused by design and manufacturing flaws. Our group has made a great effort to improve upon these aspects. B. Hogan, our chief engineer, has re-designed the emitter and developed a detailed manufacturing process to assure significant improvement in the temperature uniformity of future emitters. He has worked closely with industry, in particular with SEMICON Associates, our primary supplier of MIG emitters. Two new emitters are being manufactured which include his modifications. Additionally, an entirely new electron gun is being built for our experiment by Calabazas Creek Research (CCR) which should possess great improvements in its vacuum as well as electrostatic characteristics in comparison with our present MIG [52]. These upgrades of the emitter and MIG will increase greatly the performance of the four-cavity gyrokystron in future experiments.

Once the gyrokystron is tested and optimized experimentally, we will move on to the task of coupling it to the accelerator. This task will likely unravel a new array of technical and scientific difficulties. Furthermore, the issues of amplitude and phase control of the output power and matching of parameters between the two parallel feeds of the linear accelerator will definitely be very challenging. Another important concern is electric breakdown. Transporting powers of the order of 30-70 MW through various waveguide sections and mode conversions will certainly create areas of high electric fields where breakdown may occur. There is much yet to be learned while carrying out this work, and results from these experiments will have a crucial influence on the design and construction of future particle accelerators.

REFERENCES

- [1] D.H. Perkins, *An Introduction to High Energy Physics*, Addison Wesley, 1987.
- [2] R.N. Mohapatra, *Unification and Supersymmetry: The Frontiers of Quark-Lepton*. New York. Springer Verlag. 1991.
- [3] M. Carena *et al.*, “The complementarity of LEP, the Tevatron and the LHC in the search for a light MSSM Higgs boson”, *Phys.Rev.* D62 (2000).
- [4] J.D. Lykken, “Physics Needs for Future Accelerators”, *Int. J. Mod. Phys.* A15S1 pp.787-805, 2000.
- [5] H. Wiedemann, *Particle Accelerator Physics*. Berlin: Springer Verlag, 1993. pp.300-336.
- [6] H. Bare *et al.*, “The complementary roles of the LHC and the LC in discovering supersymmetry”, Contribution to Snowmass 2001.
- [7] J. Ellis, “Possible Accelerators at CERN Beyond the LHC”, Proceedings of the Workshop on the Development of Future Linear Electron-Positron Colliders for Particle Physics Studies and for Research using Free-Electron Lasers”, Lund, 23 - 26 September 1999.
- [8] R.B. Neal, “Accelerator Parameters for an e⁺e⁻ Super Linear Collider”, Stanford Linear Accelerator Center, *Pub. SLAC/AP-7*, 1983.
- [9] V.L. Granatstein and W. Lawson, “Gyro-Amplifiers as Candidate RF Drivers for TeV Linear Colliders”, *IEEE Trans. Plas. Sci.*, vol. 24, no.3, 1996.
- [10] R.H. Varian and S.F. Varian, “A high frequency oscillator and amplifier”, *J. Appl. Phys.*, vol. 10, pp. 321-327, May 1939.
- [11] R.M. Phillips and D.W. Sprehn, “High-Power Klystrons for the Next Linear Collider”, *Proc. of IEE - Special Issue*, May 1999, pp.738-751.
- [12] D. Sprehn, "SLAC RF Source Research at X-Band" Presented at RF 2003, 6th Workshop on High Energy Density and High Power RF, Berkeley Springs, WV, June 22-26, 2003. Published in High Energy Density and High Power RF, AIP Conf. Proc. 691, New York: AIP Press, 2003, pp.15-21.
- [13] Gold, Steven H., Fliflet, Arne W., True, Richard, “X-band magnicon amplifier for the Next Linear Collider.”, *Physics of plasmas*, vol. 4 n.5, p.1900, 1997.

- [14] L. Song *et al.*, "Development of an X-Band 50 MW Multiple Beam Klystron" Presented at RF 2003, 6th Workshop on High Energy Density and High Power RF, Berkeley Springs, WV, June 22-26, 2003. Published in High Energy Density and High Power RF, AIP Conf. Proc. 691, New York: AIP Press, 2003, pp.100-106.
- [15] V.L. Granatstein, "Scanning the Technology", *Proc. of IEE - Special Issue*, May 1999, pp.702-716.
- [16] M. V. Fazio, W. B. Haynes, B.E. Carlsten, and R.M. Stringfield, "A 500 MW, 1 μ s Pulse Length, High Current Relativistic Klystron" *IEEE Trans. Plas. Sci.* vol.22, no.5, pp.740-749, 1994.
- [17] J. Haimson and B. Mecklenburg, "A 71 dB Gain, High Efficiency Relativistic Klystron using a High Current Linear Accelerator Traveling Wave Buncher Output Structure" Presented at RF 2003, 6th Workshop on High Energy Density and High Power RF, Berkeley Springs, WV, June 22-26, 2003. Published in High Energy Density and High Power RF, AIP Conf. Proc. 691, New York: AIP Press, 2003, pp.34-45.
- [18] L. Schachter, J.A. Nation, "Beam-Quality and Guiding-Magnetic-Field Requirements for a High-Power Traveling-Wave Amplifier Operating at 35 GHz" *Phys. Rev. E*, vol. 57, no. 6 p.7176, 1998.
- [19] D. Shiffler, J.A. Nation, J.D. Ivers, G.S. Kerslick, and L. Schachter, "A high-power two stage traveling-wave tube amplifier" *J. Appl. Phys.* vol. 70, no.1 p.106, 1991.
- [20] W.L. Menninger, B.G. Danly, R.J. Temkin, "Multimegawatt Relativistic Harmonic Gyrotron Traveling Wave Tube Amplifier Experiments", *IEEE Trans. Plas. Sci.*, Jun 1994 v.24 n.3 p.687.
- [21] J.L. Rullier, S. Alberti, and B.G. Danly, "High Power CARM and Harmonic Gyro-Amplifier Experiments", *Nucl. Inst. & Meth. In Phys. Res.*, vol.341 n1 /3, p.93 1994.
- [22] S.L. Allen, et.al., "Generation of High Power 140 GHz Microwaves with an FEL for the MTX Experiment", *Proceedings of the 1993 Particle Accelerator Conference*, New York : IEEE Press, 1993, pp.1551-1553.
- [23] H.P. Freund and G.R. Neil, "Free-Electron Lasers: Vacuum Electronic Generators of Coherent Radiation", *Proc. of IEE - Special Issue*, May 1999, pp.782-803.
- [24] H.P. Freund and T.M. Antonsen Jr., *Principles of Free-electron Lasers*. London: Chapman & Hall, 1996.

- [25] K.L. Felch *et al.*, “Characteristics and Applications of Fast-Wave Gyrodevices”, *Proc. of IEE - Special Issue*, May 1999, pp.751-781.
- [26] M. Blank, B.G. Danly, B. Levush, and DE. Pershing, “Experimental Investigation of W-Band (93 GHz) Gyroklystron Amplifiers”, *IEEE Trans. Plas. Sci.*, vol.26, pp.409-415, 1998.
- [27] J.P. Calame, M. Garven, J.J. Choi, K. Nguyen, F. Wood, M. Blank, B.G. Danly, and B. Levush, “Experimental Studies of Bandwidth and Power Production in a Three-Cavity, 35 GHz Gyroklystron Amplifier”, *Phys. Plasmas*, vol.6, pp.285-297, 1999.
- [28] W. Lawson *et al.*, “Design of a 10-MW, 91.4-GHz, Frequency-Doubling Gyroklystron for Advanced Accelerator Applications”, *IEEE Trans. Plas. Sci.*, vol.29, pp.545-558, 2001.
- [29] K.R. Chu, Victor L. Granatstein, P.E. Latham, W. Lawson, and Charles Striffler, “A 30-MW Gyroklystron-Amplifier Design for High-Energy Linear Accelerators”, *IEEE Trans. Plas. Sci.*, vol. PS-13 no.6, 1985.
- [30] J. Calame, W. Lawson, V.L. Granatstein, P.E. Latham, B. Hogan, C.D. Striffler, M.E. Read, M. Reiser, and W. Main, “Experimental Studies of Stability and Amplification in Four Overmoded, Two-Cavity Gyroklystrons operating at 9.87 GHz”, *J. Appl. Phys.*, vol. 70, pp.2423-2434, 1991.
- [31] J.P. Calame and W.G. Lawson, “A modified Method for Producing Carbon-Loaded Vacuum-Compatible Microwave Absorbers from a Porous Ceramic”, *IEEE Trans. Electron Devices*, vol.38, pp.1538-1543, 1991.
- [32] W. Lawson, J.P. Calame, B. Hogan, P.E. Latham, M.E. Read, V.L. Granatstein, M. Reiser, and C.D. Striffler, “Efficient Operation of a High-Power X-Band Gyroklystron”, *Phys. Rev. Lett.*, vol.67, pp.520-523, 1991.
- [33] W. Lawson, J.P. Calame, B. Hogan, M. Skopec, C.D. Striffler, and V.L. Granatstein, “Performance Characteristics of a High-Power X-Band Two-Cavity Gyroklystron”, *IEEE Trans. Plas. Sci.*, vol. 20, pp.216-223, 1992.
- [34] S. Tantawi, W. Main, P.E. Latham, G. Nusinovich, W. Lawson, C.D. Striffler, and V.L. Granatstein, “High Power X-Band Amplification from an Overmoded Three-Cavity Gyroklystron with a Tunable Penultimate Cavity”, *IEEE Trans. Plas. Sci.* vol. 20, pp.205-215, 1992.
- [35] W. Lawson, H.W. Matthews, M.K.E. Lee, J.P. Calame, B. Hogan, J. Cheng, P.E. Latham, V.L. Granatstein, and M. Reiser, “High-Power Operation of a K-Band Second Harmonic Gyroklystron”, *Phys. Rev. Lett.*, vol. 71 pp.456-459, 1993.

- [36] H.W. Matthews, W. Lawson, J.P. Calame, M.K.E. Flaherty, B. Hogan, J. Cheng, and P.E. Latham, "Experimental Studies of Stability and Amplification in a Two-Cavity Second Harmonic Gyroklystron", *IEEE Trans. Plas. Sci.*, vol.22, pp.825-833, 1994.
- [37] W. Lawson, B. Hogan, and H. Metz, "Design and Operation of a Two-Cavity, Third Harmonic Ka-Band Gyroklystron", *Appl. Phys. Lett.*, vol.69 n.13, p.1849, 1996.
- [38] M.K.E. Flaherty, et. al., "Operation of a K-Band Second Harmonic Coaxial Gyroklystron", *J. Appl. Phys.*, vol.76, p.4393-4398, 1994.
- [39] W. Lawson, J. Cheng, J.P. Calame, M. Castle, B. Hogan, V.L. Granatstein, M. Reiser, and G.P. Saraph, "High-Power Operation of a Three-Cavity X-Band Coaxial Gyroklystron", *Phys. Rev. Lett.*, vol. 81, pp.3030-3033, 1998.
- [40] M.W. Castle, "Operation of a high-power, second harmonic, coaxial gyroklystron", Ph.D Dissertation, University of Maryland College Park, 2001.
- [41] V.L. Bratman, N.S. Ginzburg, G.S. Nusinovich, M.I. Petelin, and P.S. Strelkov, "Relativistic Gyrotrons and Cyclotron Autoresonance Masers", *Int. J. Electron.*, vol.51, 1981, p.541.
- [42] B.G. Danly and R.J. Temkin, "Generalized Nonlinear Harmonic Gyrotron Theory", *Phys. Fluids*, vol.29, 1986, p.561.
- [43] K.R. Chu and J.L. Hirshfield, "Comparative study of the axial and azimuthal bunching mechanisms in electromagnetic cyclotron instabilities", *Phys. Fluids*, 21(3), 1978, p.461-466.
- [44] A.V. Gaponov, "Interaction of irrectilinear electron beams with electromagnetic waves in transmission lines", *Izu. VUZov Radiofizika*, vol. 2, pp450-462, pp. 836-837, 1959.
- [45] J. Schneider, "Stimulated emission of radiation by relativistic electrons in a magnetic field", *Phys. Rev. Lett.*, vol. 2, pp. 504-505, 1959.
- [46] J.M. Neilson, P.E. Latham, M. Caplan, and W. Lawson, "Determination of the Resonant Frequencies in a Complex Cavity Using the Scattering Matrix Formulation", *IEEE Trans. Microwave Theory Tech.*, vol.37, p.1165, 1989.
- [47] W. Lawson and P.E. Latham, "Scattering Matrix Formulation for Coaxial Cavities", *IEEE Trans. Microwave Theory Tech.*, vol. 40 ,p.1973-1977, 1992.

- [48] P.E. Latham, W. Lawson, and V. Irwin, "The Design of a 100 MW Ku Band, Second Harmonic Gyroklystron Experiment", *IEEE Trans. Plas. Sci.*, vol.22, p.804-817, 1994.
- [49] M. Reiser, *Theory and Design of Charged Particle Beams*. John Wiley. 1994 , pp.204-205.
- [50] P.E. Latham, S.M. Miller, and C.D. Striffler, "Use of Lie Transforms to Generalize Madey's Theorem for Computing the Gain in Microwave Devices", *Phys. Rev. A*, vol.45, no.2, pp.1197-1206, 1992.
- [51] J.P. Calame, "Modulator Design for a 30 MW Gyroklystron", Master of Science Thesis, University of Maryland, 1986.
- [52] L. Ives *et al.*, "Development of improved cathodes for high power RF sources", *Proc. of The IEEE Particle Accelerator Conference*, Portland, OR, May 12-16, 2003, pp. 1113-1115.
- [53] I.G. Yovchev, W.G. Lawson, G.S. Nusinovich, V.L. Granatstein, and M.W. Castle, "Present Status of a 17.1-GHz, Four-Cavity, Frequency-Doubling Coaxial Gyroklystron Design", *IEEE Trans. Plas. Sci.*, vol.28, pp.523-528, 2000.
- [54] M.K.E. Flaherty, "Coaxial Circuits for Gyroklystron Amplifiers", Master of Science Thesis, 1994.
- [55] Wes Lawson, "Theoretical Evaluation of Nonlinear Tapers for a High Power Gyrotron", *IEEE Trans. Microwave Theory Tech.*, vol.38, 1990.
- [56] J.P. Calame, J. Cheng, B. Hogan, W. Lawson, C.D. Striffler, P.E. Latham, and V. Irwin, "Measurements of Velocity Ratio on a 90 MW Gyroklystron Electron Beam", *IEEE Trans Plas. Sci.*, vol.22 n.4, pp.476-485, 1994.
- [57] A.S. Gilmour, *Microwave Tubes*, Artech House, 1986.
- [58] M. Cristea and G. Zisis, "Thin barium Layer Formation and its Influence on Tungsten Electrode Arc Attachment Modes in HID Lamps", *J. of Optoelectronics and Advanced Materials*, Vol.5, No. 2, June 2003, p.511-520.
- [59] Electrical Engineering Simulation Software, Version 2.0.62, Copyright 1984-1988, ANSOFT Corp.
- [60] J.P. Anderson, "The Advanced-Concept Gyroklystron Design", Master of Science Thesis, University of Maryland, 1997.

- [61] J. Haimson and B. Mecklenburg, "A Linear Accelerator Power Amplification System for High Gradient Structure Research" in *Proc. Advanced Accelerator concepts*, pp. 1003-1013, (1998).
- [62] S. G. Tantawi, N. M. Kroll, and K. Fant, "Rf Components Using Over-Moded Rectangular Waveguides for the Next Linear Collider Multi-Moded Delay Line RF Distribution System," *Proc. Of The IEEE Particle Accelerator Conference*, New York City, March 29th - April 2nd, 1999, p. 1435-1437.
- [63] I. Spassovsky, E. S. Gouveia, S. P. Tantawi, B. P. Hogan, W. Lawson, and V. L. Granatstein, "Design and Cold-Testing of a Compact $TE_{01} \rightarrow TE_{20}$ Mode Converter," *IEEE Trans. Plasma Sci.* **30**, 787-793 (2002).